No. 321
September 1992

The Numerical Stability of Nonlinear Floating Body Calculations

Jong-Hwan Park

Department of Naval Architecture
and Marine Engineering

No. 321
September 1992

THE NUMERICAL STABILITY OF NONLINEAR FLOATING BODY CALCULATIONS

by

Jong-Hwan Park

Department of Naval Architecture
and Marine Engineering
College of Engineering
The University of Michigan
Ann Arbor, MI 48109-2145

THE NUMERICAL STABILITY OF NONLINEAR FLOATING BODY CALCULATIONS

by

Jong-Hwan Park

A dissertation submitted in partial fulfillment
of the requirements for the degree of
Doctor of Philosophy
(Naval Architecture and Marine Engineering)
in The University of Michigan
1992

This work has been supported by the Office of Naval Research, Applied Hydrodynamics Research Program in Nonlinear Ship Hydrodynamics, Contract No. DOD-G-N0014-90-J-1818

Doctoral Committee:

Associate Professor Armin W. Troesch, Chairperson
Professor Robert F. Beck
Assistant Professor Marc Perlin
Professor Bram van Leer

ABSTRACT

THE NUMERICAL STABILITY OF NONLINEAR FLOATING BODY CALCULATIONS

by

Jong-Hwan Park

Chairperson: Armin W. Troesch

The numerical stability of nonlinear body-wave interaction problems is investigated by applying potential flow assumptions to oscillating, non-wallsided two-dimensional and three-dimensional axisymmetric bodies. This body-wave interaction problem is solved using a mixed two-step Eulerian-Lagrangian method. In the first step, Laplace's equation is solved to determine the unknown potential values on the body and the unknown derivatives of the potentials on the free surface. In the second step, free surface boundary conditions are applied using the results of the first step to find the evolved free surface location and new potential values on the new location. Each step has particular mathematical characteristics (elliptic or parabolic-like), so that each step requires different numerical schemes. Consequently, the numerical stability of this body-wave interaction problem contains the characteristics of both of these two steps.

The major contributions made to this body-wave interaction problem are the effects of the various parameters (*i.e.* time increments, panel length, *etc.*) and the different forms of the Boundary Integral Method (BIM) on numerical stability and accuracy. The far-field truncation requirement is met by matching the linear outer solution to the nonlinear inner solution at the truncation boundary. The intersection point is traced by the extrapolation method with a special boundary condition at the intersection point. To determine the evolution of the free surface according to a Lagrangian model, a regridding scheme is utilized to prevent the concentration of the Lagrangian markers in the vicinity of high gradients.

A parameter for the numerical stability of free surface waves, the Free Surface Stability (FSS) number, is defined as a function of the time step size and the discretized panel length. The various stability regions are investigated by changing the FSS number, Green's function constant **c**, and numerical schemes. A nonlinear stability analysis is also compared to the results of the linear stability analysis for a number of specific conditions to study the effect of nonlinear boundary conditions.

To my parents and loving family

ACKNOWLEDGEMENTS

Thank God ! Glory of God.

You have finished one step on me for the next work in Your plan.

Show me the way I have to pursue from now on for Your purpose.

*

First of all, I give my sincere thanks to my advisor, Professor Troesch. He kindly guided and encouraged me to finish this work. I remember Professor Brockett who helped me to make good start of my research work at the University of Michigan. I send my appreciation to him in Washington via air.

I appreciate Professor Beier for his comments and help with the plotting programs and for his wonderful software 'MPLOT'. I am indebted to Professor van Leer and Professor Perlin for their suggestions and comments. I am thankful to Professor Beck for his comments and constructive discussions he shared with me.

I wish to express my thanks to Professor Jong-Heul Hwang and other professors who taught me in the Seoul National University. My special thanks should be given to Dr. Jong-hyun Kim, Dr. Chang-Gu Kang, Dr. Seok-Won Hong, Dr. Jung-chun Suh, Myung-Hwan Kim, and all my office-mates who have spent days and nights in the office of the NAME Department and who shared their precious time when I had difficulties. Also I can not forget the warm friendship of Professor Falzarano, Dr. Ivan Kirschner, Dr. Allan Magee, and Dr. Richard Korpus.

I am very grateful to Mrs. Virginia Konz and others in our Departmental office

for their loving care in various academic processes. No flower would be more beautiful than their hearts. And I'll never forget the peaceful smile of Professor Benford which he showed every time I saw him in the hallway.

There is really important group I have to express my deepest thanks, the brothers and sisters in Christ Jesus who prayed for me and helped me to grow in the spiritual health. They made my life in Ann Arbor really meaningful and blessed.

This thesis is dedicated to my parents in Korea and my wife and two sons (Mino and Guno) who supported me patiently with love and prayer.

TABLE OF CONTENTS

LIST OF FIGURES

Figure

LIST OF TABLES

LIST OF APPENDICES

Appendix

CHAPTER I

INTRODUCTION

As the knowledge of mankind increases, the eagerness to analyze nature deepens. Scientists try to understand everything from the atom to the universe. Attempting to understand complex phenomena, they start with a specific problem, simplify it, and draw conclusions. Then they move on to more and more general and complicated phenomena, from single degree to multi-degree, from particle to continuum, from one dimension to N dimensions, from linear to nonlinear, by relaxing the physical assumptions and constraints. In the analysis of nature, the computer, which is the product of the development of science and mathematics, provides many more possibilities. It has extended broadly the possible limits of engineering and scientific solutions.

One of the complex problems which has been recently addressed in hydrodynamics is the "impact problem". The problem arises in ocean-going vessels or fast boats when the hull impacts the free surface. The impact problem first emerged in the stress analysis of seaplane landings [von Karman(1929) and Wagner(1931)]. The problem was approximated analytically by von Karman(1929) and modified by Wagner(1931). These approximations became the basic references for many subsequent investigations.

With the advent of computers, it became possible to study the impact problem much more effectively. Computer calculations allowed people to see nonlinear effects by simulation and to propose nonlinear solutions that do not exceed the permissible engineering range of error. The introduction of computers facilitated "a method of calculation by means of an electronic computer of the non-lifting potential flow about arbitrary three-dimensional bodies" [Hess and Smith(1964)]. This method marked a breakthrough in computational fluid dynamics.

In an effort to solve the nonlinear free-surface wave problem, Longuet-Higgins and Cokelet (1976) presented a mixed Eulerian-Lagrangian method. The mixed Eulerian-Lagrangian method is comprised of two separate calculations, one in the Eulerian sense and the other in the Lagrangian sense. This method advances in time individual particles on the free surface following the solution of an integral equation. Using a technique similar to that of Longuet-Higgins and Cokelet(1976), Faltinsen(1977) solved a nonlinear body-wave interaction problem. In this problem, Faltinsen added a two-dimensional body which interacts with the free surface. He assumed that the body intersects the free surface and oscillates harmonically in the vertical plane. He also treated the far-field radiation problem as the flow induced by a dipole located at the center of the body. This far-field model is the first term in an expansion of a linear time-dependent free surface Green function. Vinje and Brevig(1981) determined a numerical method for the time simulation of two-dimensional surface-piercing bodies of arbitrary shapes. They used the exact free-surface boundary condition and considered finite depth effects. They solved the problem using the Cauchy integral theorem to calculate the complex potential and its derivatives along the boundary. Baker *et al.*(1982) treated a two-dimensional nonlinear free surface problem in water of finite depth with appropriate dipole (vortex) and source distributions. They

solved the resulting Fredholm integral equations by iteration.

Dommermuth and Yue(1986) developed a numerical method for nonlinear three-dimensional axisymmetric free surface problems using a mixed Eulerian-Lagrangian scheme. They used Rankine ring sources with Green's theorem, a boundary integral formulation. Kang(1988) investigated nonlinear interactions between the free surface and three-dimensional axisymmetric floating bodies in water of infinite depth. He performed the numerical calculation for wallsided axisymmetric bodies.

Addressing and solving this numerical free surface impact problem, three major difficulties are encountered :

- numerical stability,
- far-field closure, and
- body and free surface intersection.

Each problem is described briefly in the following sections and the related research and the methods used in this thesis are introduced.

1.1 Numerical Stability

The numerical stability problem, which is the primary concern of this thesis, occurs in any numerical iteration scheme and requires careful treatment. When the impact problem is solved using numerical calculations, there are a number of difficulties to cope with, some of which are the accumulation of numerical error and memory limitation. The accumulation of numerical error can cause serious errors which contaminate the numerical results or cause the results to diverge. This is defined loosely as numerical instability. To prevent this numerical instability, numerical schemes should be chosen carefully and operated within a proper parametric range.

Longuet-Higgins and Cokelet(1976) observed "sawtooth instabilities" on the free

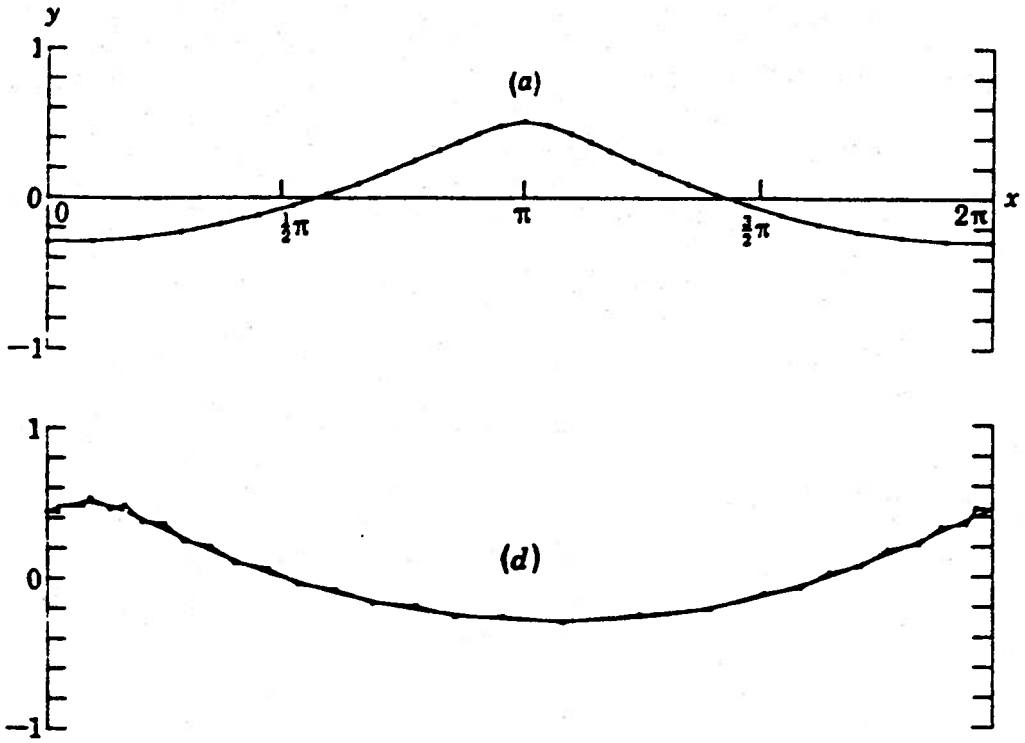

Figure 1.1: An example of the sawtooth instability observed by Longuet-Higgins and Cokelet for a steady progressive wave in deep water computed by Pade approximants for Stokes's series (smooth curve) and the corresponding time-stepped profile (unsmoothed). Number of segments, $N = 30$. The profiles are compared at times (a) $t = 0$, (d) $t = \pi$. [Longuet-Higgins and Cokelet(1976)]

surface when they followed the time history of space-periodic irrotational surface waves as can be seen in Figure 1.1. This sawtooth instability was found when a deep water progressive wave of finite amplitude was marched in time. The authors claimed that this instability was due, partly, to physical reasons and they applied a smoothing technique to remove it.

Faltinsen(1977), in the numerical solution of two-dimensional nonlinear transient problems, found that his solution procedure sometimes became invalid before the surface waves had reached the far-field boundary. To demonstrate this phenomena, he performed the calculation varying the size of the far-field boundary b. In the

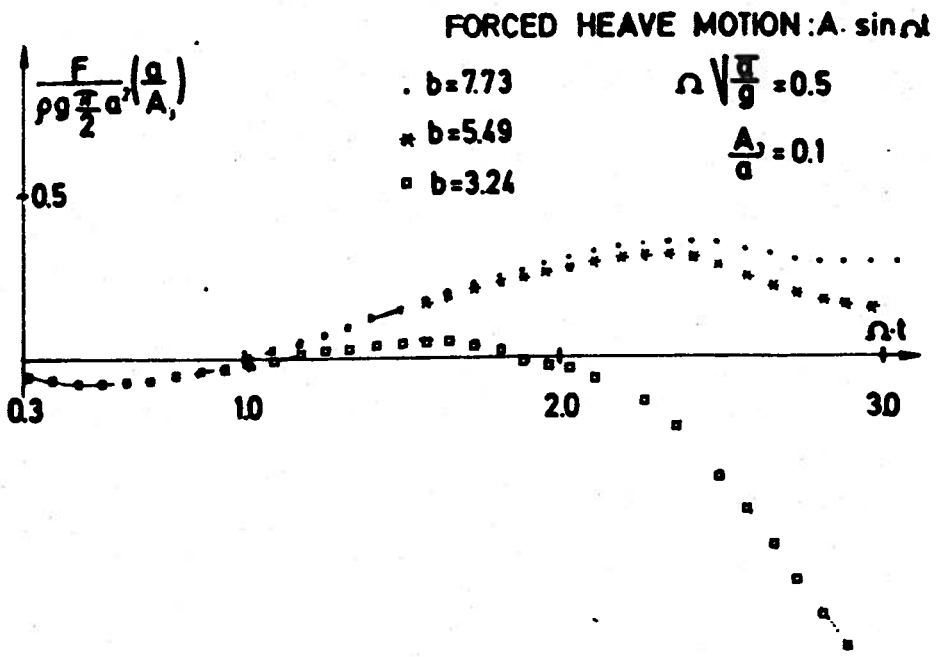

Figure 1.2: The vertical force acting on a heaving circular cylinder, an example of the instability observed by Faltinsen. 'b' represents the far-field boundary coordinate, and 'a' the radius of the cylinder. [Faltinsen(1977)]

calculation, he fixed the length of the free surface elements to $\frac{\pi}{14}a$. As shown in Figure 1.2, the force is rapidly growing in negative values for the case of $b = 3.24$. This behavior contrasts with that shown in Figure 1.1. In Figure 1.1, the error has a sawtooth shape as if a high frequency wave-like error is superposed on the onset flow contrary to Figure 1.2, where the error appears to grow exponentially. These two figures suggest that numerical errors can either grow exponentially when the error magnification factor is greater than 1.0 and pure real, or grow with changing phase when the error magnification factor is complex and has a modulus greater than 1.0. Analogous types of error growth will be shown during the investigation of the eigenvalues associated with the matrix stability analysis in Chapters III and IV.

Similar to Longuet-Higgins and Cokelet(1976), Baker *et al.*(1982) also encountered this numerical instability which occurred when the local waves were steep.

They used a smoothing operator to reduce the effect of the instability. They also found that this instability was reduced remarkably by the use of a dipole distribution rather than a vortex distribution.

There are also some researchers who observed no such numerical instability. The instability was removed by Roberts(1983) in his analysis of a body-wave interaction problem using Fourier spectral representations for the position and potential of a free shear layer. The modeling was accomplished by a simple modification of the highest (even) Fourier mode. This method of instability removal was also reported by Dold and Peregrine(1984) extending the idea of Vinje and Brevig(1981) with the addition of the higher time derivatives of the complex potential in the Eulerian step. Using the resulting time integration scheme, they found no apparent short-wavelength instability. Another numerically stable scheme was given by Casulli and Cheng(1990) in their discussion of the stability and error analysis for some finite difference methods of the one-dimensional shallow water equations which consist of a system of quasi-linear hyperbolic equations. They showed that the explicit Eulerian-Lagrangian method with fixed grid is unconditionally stable when the Courant-Isaacson-Rees method is used as a time-stepping scheme.

Dommermuth and Yue(1986) and Dommermuth *et al.*(1988) claimed that the instabilities are not physical and closely related to the accuracy of the velocity calculation for the free surface particles. They postulated that when the mixed Eulerian-Lagrangian scheme is used, the high-wavenumber instability is caused mainly by the concentration of Lagrangian markers in the region of higher gradients. This concentration of the markers, they said, caused a local Courant condition to be inevitably violated for a fixed time step as the waves steepened. They developed a regridding algorithm wherein a new set of equally spaced Lagrangian points on the free surface

is created each time step. This regridding algorithm has the disadvantage of the loss of resolution near the region of high velocity gradients where Lagrangian points would otherwise concentrate. Kang(1988) speculated that the numerical error at the intersection point propagates and could generate saw-tooth instabilities.

Fewer researchers have actually established stability criteria. Yeung(1982) investigated the stability criteria using a *simplified* von Neumann analysis. He assumed $\phi(x, y, n\Delta t)$ to be of the form $\phi^n e^{ikx+ky}$ where k is a wave number; thus $\phi_y^n = k\phi^n$. His calculation for the numerical stability criteria is simple and easy to follow. However, his stability criteria is independent of the panel length Δx and independent of the various boundary conditions.

Dommermuth *et al.*(1988) derived the numerical stability criteria using a 'linearized von Neumann stability analysis'. They also assumed $\phi_y^n = k\phi^n$. By this assumption and a Taylor-series expansion, they found the stability criteria for the explicit fourth-order Runge-Kutta scheme and the fourth-order multi-step Adams-Bashforth-Moulton predictor-corrector (ABM4) scheme.

In this thesis, an effort is made to find the neutrally stable region or conditionally stable algorithm in the numerical calculation of the impact problem

- utilizing a Green function constant,
- managing the far-field condition, and/or
- applying the regridding algorithm on the free surface.

A new stability parameter is introduced: the Free Surface Stability number (FSS $= \pi g \frac{(\Delta t)^2}{\Delta x}$) where Δt represents the time-step size, Δx the panel length, and g the gravity force. This FSS number contrasts with the stability parameter of Yeung(1982) ($f = kg\frac{(\Delta t)^2}{2}$) and the Courant condition of Dommermuth and Yue(1986) ($(\Delta t)^2 \leq \frac{8}{\pi}\frac{\Delta x}{g}$).

The FSS number of this thesis is defined as the ratio of $(\Delta t)^2$ and Δx, and the effect of the ratio on the numerical stability is investigated. The spatial and temporal increment, Δx and Δt, represent the basic parameters of a numerical code for the elliptic partial difference equation and for the parabolic partial difference equation respectively. This is based on the idea that the free surface problem is a combination of two types of partial differential equations: Laplace's equation and the free surface boundary condition equations. The two different stability criteria derived by Yeung(1982) and Dommermuth *et al.*(1988) are compared with the results of this thesis in Chapters III and IV.

1.2 Far-field Closure

In addition to numerical instability, the proper treatment of the far-field condition is another difficult problem. If there is no interaction with a body, the free surface problem is sometimes solved by the assumption of periodicity as done by Longuet-Higgins and Cokelet(1976). However, this periodicity can hardly be applied if a body is introduced into the problem. A simple way to alleviate this difficulty is to make the computational domain as large as possible so that the far-field truncation effect can be ignored. The disadvantage of this approach, though, is that it consumes time and money and is limited by computer size.

Faltinsen(1977), in solving two-dimensional numerical free surface motion with an oscillating body, used the method of matching the numerically generated nonlinear inner solution to an outer solution with a Rankine dipole at the origin. Since this Rankine dipole solution does not consider wave effects, it is valid only until a propagating wave nears the far-field boundary. Dommermuth and Yue(1986) posed a far-field closure by matching the nonlinear computational solution to a general lin-

ear solution of a transient radiated wave. Kang(1988) derived the three-dimensional axisymmetric form of Faltinsen's matching scheme.

In this thesis, Kang(1988)'s far-field closure is applied and the effect of the far-field condition on numerical stability is investigated. In Chapter III, it is shown that the far-field closure conditions produce different regions of stability.

1.3 Body and Free Surface Intersection

As a body is introduced onto the free surface, several significant difficulties such as the calculation of potential values near the intersection point and the locus of the intersection point must be confronted. The calculation of potential values involves singular integrals which need special treatment. Kang(1988) analytically deleted the logarithmically singular terms before numerical calculation. He also found that the continuity of the potential and the velocity of water particles at the intersection point is automatically satisfied on the wallsided body assuming that the intersection angle is fixed to 90 degrees.

In this thesis, the intersection point is traced using a non-uniform parametric Lagrangian polynomial interpolation scheme with the control point in the center of the panel. By this treatment, the potentials for the non-wallsided body are calculated and the initial stage of the forming of a jet is observed.

1.4 Research Objectives

The investigation for the stability analysis starts with the linear "near-field" boundary value problem, which is the simplest modeling of the free surface problem. The linear "closed boundary" problem is dealt with next and finally the linear "far-field" boundary problem follows. Each of these problems is described in Chapter III

with the numerical stability results. The panel method is used to solve the field equation, a limiting form of Green's second identity. In the determination of the new free surface location and new potential value of a boundary point, various kinds of the finite difference methods are used. The numerical stability characteristics of each of these numerical schemes are studied. For some simple cases, the stability region is analytically derived as a function of the FSS number. In each case, analytical or numerical stability regions are found as a function of the FSS number and $c\Delta x$, where c is the Green function constant. Simulations of these cases are performed to confirm the boundaries of the stability region. The effects of the various time marching schemes and body shapes on stability are also investigated. Stability regions are also compared with previously published results such as Yeung(1982) or Dommermuth and Yue(1986).

In Chapter IV, the numerical stability of the nonlinear free surface problem with a two-dimensional or three-dimensional axisymmetric body is solved. This is done with a nonlinear free surface and with the nonlinear free surface boundary conditions. The stability region of the nonlinear problem is compared with that of the linear problem. The effect of c (the Green function constant) and the effect of numerical schemes, by varying the FSS number, are also considered. The influence of decreasing deadrise angle on jet formation is investigated. High tangential velocities, near the intersection point create difficulties in the accurate modeling of jets. In Chapter V, the results of this thesis and the direction of future work are discussed.

CHAPTER II

FORMULATION OF THE PROBLEM

In this chapter, basic assumptions made in the analysis of the problem are reviewed. After the review, the governing equation (*i.e.* Laplace's equation) is discussed and relevant boundary conditions are described. A brief explanation of various numerical schemes is given including the ones used in this thesis.

2.1 Governing Equation and Boundary Conditions

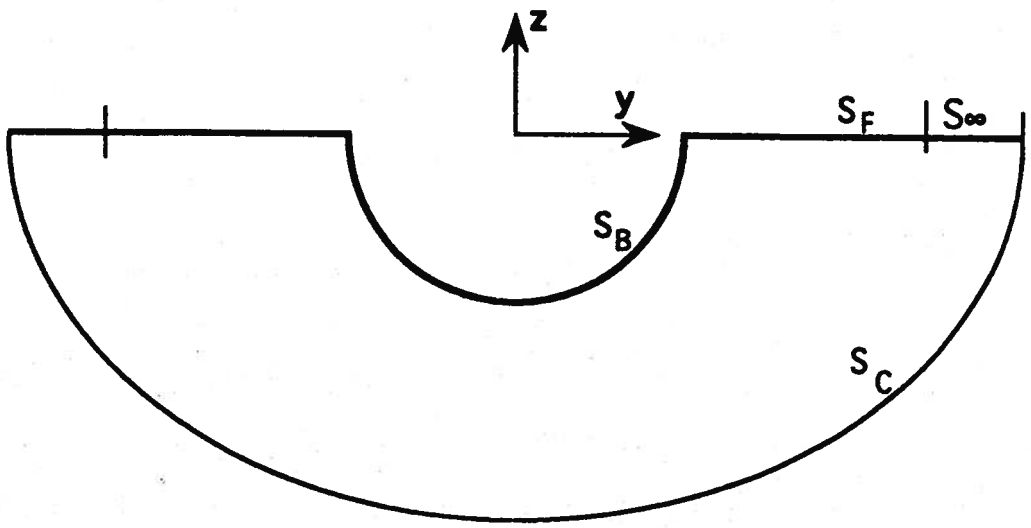

Figure 2.1: Coordinates and geometry of the free surface problem

The coordinate system used in this work is depicted in Figure 2.1. The figure represents an infinitely long two-dimensional symmetrical body, or a three-dimensional axisymmetric body, either of which is forced to oscillate vertically on a free surface. The body shape is arbitrary and the body motion can be cyclic or linear with constant velocity in the z direction.

The free surface is given by $F(\vec{x}, t) = 0$, where $\vec{x}(x, y, z)$ is the position vector in the right-handed coordinate system. In this system, the z axis is defined as positive upwards, while the y axis represents the calm water level. The origin is at the intersection of the vertical centerline of the body and the undisturbed water surface.

The fluid is assumed to be incompressible and inviscid, and the flow is assumed to be irrotational. Given the above assumptions, the velocity potential $\phi(\vec{x}, t)$ can be introduced and the velocity of a fluid particle can be expressed as the gradient of this potential, written as $\vec{u} = \nabla\phi$. Surface tension at the free surface is assumed negligible and thus not considered. Finally, the water is considered to be sufficiently deep to ignore bottom effects and the surface is assumed to be initially at rest.

With the several assumptions stated for the mathematical model, the governing equation is now introduced — Laplace's equation:

- Governing equation (Laplace's equation)

$$\nabla^2\phi = 0 \qquad \text{in the fluid domain} \tag{2.1}$$

where ∇^2 is the Laplacian operator. Laplace's equation is another form of the continuity equation expressed with the velocity potential. The equation is a statement of conservation of mass and thus there is neither creation nor destruction of fluid inside the domain.

In order to solve the impact problem, Laplace's equation must satisfy the following

boundary conditions :

- the kinematic free surface boundary condition,
- the dynamic free surface boundary condition,
- the body boundary condition, and
- the far-field boundary condition.

The first two conditions – the kinematic free surface boundary condition and the dynamic free surface boundary condition – are applied on the free surface, which is composed of a certain set of water particles. The kinematic free surface boundary condition means that the normal velocity of a water particle on the free surface is the same as the normal velocity of the free surface itself. In another words, once a particle is on the free surface, it remains there. The kinematic boundary condition is :

- Kinematic free surface boundary condition

$$\frac{D(z-\eta)}{Dt} = (\frac{\partial}{\partial t} + \nabla\phi \cdot \nabla)(z-\eta) = 0 \qquad \text{on } z = \eta(x,y,t) \tag{2.2}$$

where $\frac{D}{Dt}$ is the substantial(material) derivative. This kinematic condition is used to trace the free surface as a function of time.

The dynamic free surface boundary condition is obtained from Bernoulli's equation which assumes that the pressure on the free surface must be atmospheric. The right-hand side constant $C(t)$ of Bernoulli's equation is absorbed into the potential $\phi(\vec{x},t)$ and the value of the time-independent constant is set to equal the atmospheric pressure, P_a. The dynamic free surface boundary condition is stated as :

- Dynamic free surface boundary condition

$$\frac{p}{\rho} + \frac{\partial\phi}{\partial t} + \frac{1}{2}|\nabla\phi|^2 + gz = 0 \tag{2.3}$$

$$\longrightarrow \quad \frac{D\phi}{Dt} = -g\eta + \frac{1}{2}\nabla\phi \cdot \nabla\phi \qquad \text{on } \; z = \eta(x,y,t). \tag{2.4}$$

By this dynamic condition, the value of the potential on the free surface is determined.

Having described the two free surface boundary conditions, the body boundary condition is introduced next. Under this condition, a fluid particle can not penetrate the solid-body surface, rather it remains in contact with the surface. Thus, the normal velocity of the particle on the body surface is the same as that of the body surface :

- Body boundary condition

$$\vec{V} \cdot \vec{n} = \nabla\phi \cdot \vec{n} \qquad \text{on the body } S_B(x, y, z, t) = 0 \tag{2.5}$$

where $\vec{V}$ is the velocity of the body and $\nabla\phi$ is the velocity of the fluid particle on the body. The unit normal vector $\vec{n}$ is directed outwards from the domain of interest *i.e.* into the body.

The fourth boundary condition, the far-field condition, is defined for the unbounded far-field. The normal velocity far away is assumed to tend to zero :

- Far-field condition

$$\frac{\partial\phi}{\partial n} \to 0 \text{ as } |r| \to \infty \tag{2.6}$$

where $|r|$ is the distance from the origin. This far-field condition is one of the more difficult conditions to apply properly. For the two-dimensional problem, especially, this condition needs to be treated carefully. The far-field truncation effect, properly considered, makes the computational domain finite.

The above four conditions along with the governing equation constitute a well-posed boundary value problem. Specific solutions can be obtained analytically as in the case of infinitesimal amplitude motions and waves, or numerically as in the case of large amplitude motions and waves. One of the methods used in this thesis to

solve Equations 2.1 $\sim$ 2.6 is numerical simulation. Simulation times are short enough so that waves generated by the body never propagate to the far-field boundary. This short time scale approach will allow for the calculation of the potential values and the pressure on the body during impact or the first few cycles of transient motion.

2.2 Method of Solution

In this section, several methods for solving the governing equation and the four boundary conditions stated in Section 2.1 are discussed. There are a number of approaches for doing so and the typical one used with moving boundaries is the two-step approach. In the two-step approach, the governing equation is solved first on a temporarily fixed boundary, and then the free surface boundary equations are solved to determine the new boundary position and the values of the normal derivatives on that boundary. These two steps are iterated as a function of time. Each step can be solved in the Eulerian sense, where all the physical values are calculated at the spatial points, or in the Lagrangian sense, where all the physical values are calculated along the path of the moving water particles. There are thus two steps, and the option of using either the Eulerian sense or Lagrangian sense for each.

Typically, solutions of the impact problem with a moving boundary use the Eulerian sense in Step 1 and the Lagrangian sense in Step 2. This strategy was introduced by Longuet-Higgins and Cokelet(1976) (who termed it the 'mixed Eulerian-Lagrangian method'), and it is now in frequent use. This numerical approach is adapted in this work, but with different numerical schemes in each step. In Step 1, the governing equation using the Boundary Integral Method (BIM) is solved; and in Step 2, the free surface boundary conditions are satisfied using several different

time-stepping schemes. Below is a brief summary of how the two-step method works.

- Step 1 :

  Solve the governing equation to get the normal derivatives[1], ${\phi_n}^n$, on the free surface with the given boundary condition using the BIM. The boundary condition can be given as Dirichlet type, Neumann type, or Cauchy type (combination of Dirichlet type and Neumann type). In this step, the governing equation which has elliptic partial differential equation characteristics is solved in the Eulerian sense.

- Step 2 :

  Apply the kinematic free surface boundary condition to get the new location of the free surface η^{n+1} using ${\phi_n}^n$ and ϕ^n. On the new free surface, get the new boundary value ϕ^{n+1} from the dynamic free surface boundary condition. In this step, the new location and new boundary values are obtained in the Lagrangian sense.

These two steps are depicted in Figure 2.2 and these steps repeat as time continues. Several numerical solvers for step 1 including the BIM are introduced in Section 2.2.1 and solvers for step 2 in Section 2.2.2.

2.2.1 Governing Equation Solver

Currently, there are various numerical methods used in Step 1 to solve Laplace's equation. Four of these methods including the BIM are described in this section with an assessment of their respective benefits and limitations.

[1]The superscript n in ${\phi_n}^n$ represents the (n) time step whereas the subscript n means the normal derivative of ϕ.

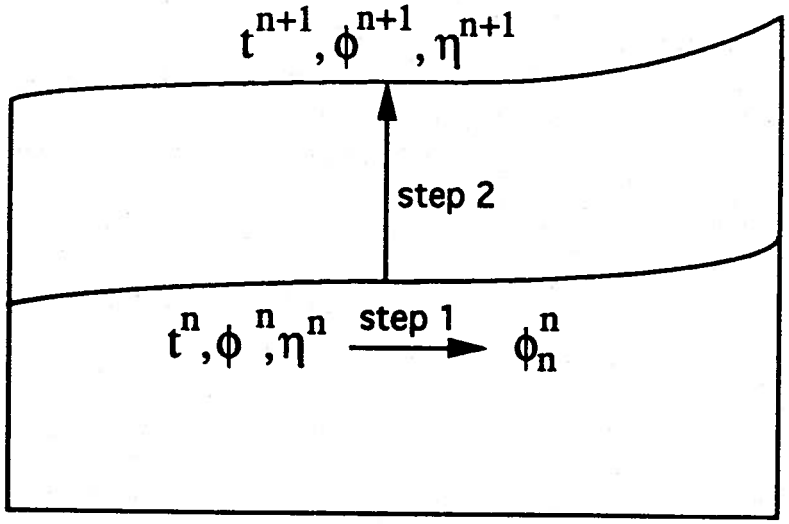

Figure 2.2: Mixed Eulerian Lagrangian method

Finite Difference Method

The Finite Difference Method (FDM) is well described in Richtmyer and Morton(1967) and Anderson, Tannehill and Pletcher(1984). The FDM is based on a very simple concept, the 'difference'. The partial derivatives appearing in the equations are replaced by finite differences. This method is well-established and easy to implement. The FDM is the most suitable method for rectilinear boundary-shaped domains. However for the free surface problem, which has a free boundary on the free surface, this method is not really suitable. The FDM can be developed by grid generation mapping of an arbitrary shape into a simple rectilinear one. However, this introduces the complexity of the mapping function. The principle deficiency of FDM, with regards to this thesis, is its inability to follow moving boundaries easily.

Finite Element Method

Introduced and developed in the 1960's, the Finite Element Method (FEM) has flourished in the field of structural stress analysis of complicated geometries. The FEM requires that the problem to be solved be stated in a variational form. Extensive reviews of the FEM in fluid flow problems have been given by Shen(1977), and Norrie and de Vries(1978). The FEM describes the arbitrary boundary geometry with the introduction of curvilinear or isoparametric elements [Yeung(1983)]. The usual procedure starts with subdividing the domain of interest into a mesh of finite-sized subregions. Each subregion is made of many elements and the elements can be essentially any shape, which allows great flexibility, enough to handle most kinds of geometry. For time dependent boundaries, determining time dependent elements is time consuming.

Spectral Method

The field of spectral methods in fluid mechanics is still very much in the development phase. The spectral-boundary technique is very accurate when the geometry is very smooth and simple (like a circle or an ellipse) and when the nodal spacing is uniform [Huh(1991)]. To improve accuracy, the known and unknown boundary values and the boundary shapes are expanded in a global Fourier series using an arclength parameter, resulting in an exponentially accurate solution. So, for the simple wave case which has periodicity on the free surface, the spectral method is proper. But, for contours with corners such as the body-wave interaction problem which has an intersection point, this method is inappropriate due to the large number of Fourier terms required for accuracy.

Green's Identity and the Boundary Integral Method

Despite their respective merits, the above three methods are not well suited for solving the impact problem. They require vast amounts of computer time and memory to solve for all of the domain values – values not directly related to the problem here. In contrast, the BIM solves for the potential values and the derivatives on the moving boundary efficiently – values needed to calculate the pressures or forces acting on the body. The BIM uses the information (the potential values or the derivatives of the potential) only on the boundary. In the impact problem, the potential values are given and the normal derivatives of the potential values are unknown on the free surface (a Dirichlet boundary condition). The normal derivatives are known and the potential values are unknown on the body (a Neumann boundary condition). With known boundary values on the body and the free surface, the governing equation is solved to obtain the unknown pairs, respectively. To solve Laplace's equation, the velocity potential $\phi(\vec{x}, t)$ is introduced in the fluid domain by the incompressible, irrotational and inviscid assumptions (See Section 2.1). This velocity potential $\phi(\vec{x}, t)$ describes the fluid disturbance at time t in space $\vec{x}$.

The mathematical derivation for the BIM begins with the divergence theorem.

$$\iiint \nabla \cdot \vec{V} dV = \iint \vec{n} \cdot \vec{V} dS \tag{2.7}$$

where $\vec{V}$ is any vector that is continuous and differentiable in the volume V (in this thesis, $\vec{V}$ is the fluid velocity), and the unit normal $\vec{n}$ is the outward normal vector. This theorem states that the total increase of the volume of fluid is the same as the total flux through the surface. The divergence theorem is applied to Green's first identity (Equation 2.8), and hence produces the integral equation, Green's second

identity (Equation 2.9).

$$\nabla \cdot (G\nabla\phi) = G\nabla^2\phi + \nabla G \cdot \nabla\phi \tag{2.8}$$

$$\iiint (\phi\nabla^2 G - G\nabla^2\phi)dV = \iint (\phi\frac{\partial G}{\partial n} - G\frac{\partial \phi}{\partial n})dS \tag{2.9}$$

In two dimensions, the volume integral becomes a surface integral and the surface integral becomes a line integral. The fluid domain V of interest is surrounded by a body surface S_B, free surface S_f, free surface at infinity S_∞, and the other far-field contour including bottom S_c (See Figure 2.1.).

Two quantities are introduced in Equation (2.9), ϕ is defined as the velocity potential which satisfies Laplace's equation, and G as the solution of the Poisson equation in the fluid domain :

$$\nabla^2\phi = 0 \qquad \text{and} \tag{2.10}$$

$$\nabla^2 G(\vec{x};\vec{\xi}) = -\delta(\vec{x}-\vec{\xi}) = -\frac{\delta(\vec{r})}{2\pi r} \quad (2-D) \tag{2.11}$$

$$= \frac{\delta(\vec{r})}{4\pi r^2} \quad (3-D) \tag{2.12}$$

in the fluid domain.

The solution of Equation (2.11) or Equation (2.12) can be obtained by applying Fourier Transforms or by successive integrals. Another solution G^* can be obtained by adding any analytic homogeneous solution to the particular solution, Equation (2.13) or Equation (2.14). One such set of analytic solutions are given as follows:

$$G(\vec{x};\vec{\xi}) = -\frac{1}{2\pi}\ln|\vec{x}-\vec{\xi}| = -\frac{1}{2\pi}\ln r \quad (2-D) \tag{2.13}$$

$$= \frac{1}{4\pi}\frac{1}{|\vec{x}-\vec{\xi}|} = \frac{1}{4\pi r} \quad (3-D) \tag{2.14}$$

$$G^*(\vec{x};\vec{\xi}) = -\frac{1}{2\pi}(\ln r + \ln \mathbf{c}) = -\frac{1}{2\pi}\ln r\mathbf{c} \quad (2-D) \tag{2.15}$$

$$= \frac{1}{4\pi}(\frac{1}{r}+\frac{1}{\mathbf{c}}) \quad (3-D) \tag{2.16}$$

$$\nabla G(\vec{x};\vec{\xi}) = \frac{1}{2\pi}\frac{(\vec{x}-\vec{\xi})}{|\vec{x}-\vec{\xi}|^2} \quad (2-D) \tag{2.17}$$

$$= \frac{1}{4\pi}\frac{\vec{x}-\vec{\xi}}{|\vec{x}-\vec{\xi}|^3} \quad (3-D) \tag{2.18}$$

The Green functions G and G^*, are both solutions of the Poisson equation. G^* has an arbitrary constant $\ln \mathbf{c}$ which will be important in the stability analysis in Chapters III and IV. In the equations above, $\vec{x}$ is the field point, $\vec{\xi}$ is the source point and $\mathbf{c}$ is some constant used to normalize the two-dimensional Green's function.

Substituting Equations (2.10) $\sim$ (2.18) into Equation (2.9), new surface integral equations for the potential ϕ of the point $\vec{x}$ in domain V are produced. The velocity potential in two dimensions is expressed as

$$\phi(\vec{x},t) = -\int(\phi\frac{\partial G}{\partial n} - G\frac{\partial \phi}{\partial n})\,dl \tag{2.19}$$

$$= -\frac{1}{2\pi}\int\left\{\phi(\vec{\xi},t)\frac{\vec{n}(\vec{\xi})\cdot(\vec{x}-\vec{\xi})}{|\vec{x}-\vec{\xi}|^2} + \frac{\partial\phi}{\partial n}(\vec{\xi},t)\ln|\vec{x}-\vec{\xi}|\right\}dl \tag{2.20}$$

If G^* instead of G is used in the integral equation,

$$\phi(\vec{x},t) = -\int(\phi\frac{\partial G^*}{\partial n} - G^*\frac{\partial \phi}{\partial n})\,dl \tag{2.21}$$

$$= -\frac{1}{2\pi}\int\left\{\phi(\vec{\xi},t)\frac{\vec{n}(\vec{\xi})\cdot(\vec{x}-\vec{\xi})}{|\vec{x}-\vec{\xi}|^2} + \frac{\partial\phi}{\partial n}(\vec{\xi},t)\ln \mathbf{c}|\vec{x}-\vec{\xi}|\right\}dl \tag{2.22}$$

and in three dimensions,

$$\phi(\vec{x},t) = -\frac{1}{4\pi}\iint\left\{\phi(\vec{\xi},t)\frac{\vec{n}(\vec{\xi})\cdot(\vec{x}-\vec{\xi})}{|\vec{x}-\vec{\xi}|^3} - \frac{\partial\phi}{\partial n}(\vec{\xi},t)\frac{1}{|\vec{x}-\vec{\xi}|}\right\}dS \qquad (2.23)$$

or

$$\phi(\vec{x},t) = -\frac{1}{4\pi}\iint\left\{\phi(\vec{\xi},t)\frac{\vec{n}(\vec{\xi})\cdot(\vec{x}-\vec{\xi})}{|\vec{x}-\vec{\xi}|^3} - \frac{\partial\phi}{\partial n}(\vec{\xi},t)\left(\frac{1}{|\vec{x}-\vec{\xi}|}+\frac{1}{c}\right)\right\}dS$$

As $\vec{x}$ approaches the boundary, the potential value on the boundary is derived in a principal value integral form such as

$$\phi(\vec{x},t) = -\frac{1}{\pi}\int\left\{\phi(\vec{\xi},t)\frac{\vec{n}(\vec{\xi})\cdot(\vec{x}-\vec{\xi})}{|\vec{x}-\vec{\xi}|^2} + \frac{\partial\phi}{\partial n}(\vec{\xi},t)\ln|\vec{x}-\vec{\xi}|\right\}dl \qquad (2.24)$$

$$\phi(\vec{x},t) = -\frac{1}{\pi}\int\left\{\phi(\vec{\xi},t)\frac{\vec{n}(\vec{\xi})\cdot(\vec{x}-\vec{\xi})}{|\vec{x}-\vec{\xi}|^2} + \frac{\partial\phi}{\partial n}(\vec{\xi},t)\ln c|\vec{x}-\vec{\xi}|\right\}dl \qquad (2.25)$$

and in three dimensions,

$$\phi(\vec{x},t) = -\frac{1}{2\pi}\iint\left\{\phi(\vec{\xi},t)\frac{\vec{n}(\vec{\xi})\cdot(\vec{x}-\vec{\xi})}{|\vec{x}-\vec{\xi}|^3} - \frac{\partial\phi}{\partial n}(\vec{\xi},t)\frac{1}{|\vec{x}-\vec{\xi}|}\right\}dS \qquad (2.26)$$

or

$$\phi(\vec{x},t) = -\frac{1}{2\pi}\iint\left\{\phi(\vec{\xi},t)\frac{\vec{n}(\vec{\xi})\cdot(\vec{x}-\vec{\xi})}{|\vec{x}-\vec{\xi}|^3} - \frac{\partial\phi}{\partial n}(\vec{\xi},t)\left(\frac{1}{|\vec{x}-\vec{\xi}|}+\frac{1}{c}\right)\right\}dS \qquad (2.27)$$

where $\vec{x}$ and $\vec{\xi} \in S$, and $\vec{n}$ is an outward unit normal vector.

This equation says that the velocity potential ϕ at $(\vec{x},\ t)$ can be expressed in terms of the boundary values only, without any information from inside the volume. In other words, the BIM reduces the space dimension by one which is the essential benefit of the BIM. For the free surface problem, this method is adequate since the physical values of interest are usually only on the boundaries. For each case, one of the Equations (2.24) $\sim$ (2.27) will be used in the numerical computations of Chapter III and Chapter IV.

2.2.2 Time-Stepping Schemes

Once Laplace's equation is solved in the fluid domain, the normal derivatives of the potentials on the free surface and the potentials on the body surface are obtained. With this information, the two free surface boundary conditions determine the new location of the free surface for the next time step and estimate the potential on the new free surface. The new location and the new potential on the new location are used as a boundary condition of Step 1, and the result of Step 1 is used for the next Step 2, and so on.

For this time-stepping procedure three different Euler methods are chosen; specifically the explicit, implicit-like, and implicit Euler methods. Three different fourth-order Runge-Kutta methods are also selected which are the explicit, implicit-like, and Kang's modified method [Kang (1988)]. These different numerical methods are used for comparison of the numerical stability characteristics. Detailed numerical stability concepts and their relationship to the time-stepping schemes are explained in Chapter III and Chapter IV.

CHAPTER III

LINEAR NUMERICAL STABILITY ANALYSIS AND ITS APPLICATIONS

In this chapter, the basic concept of the numerical stability analysis and its application to free surface, water wave problems will be discussed. The free surface boundary conditions (Section 2.1) are linearized. Various time stepping algorithms, such as the different Euler schemes and modified fourth-order Runge-Kutta schemes are employed. Two numerical stability analysis methods are introduced in Section 3.3. The numerical stability of the impact problem is investigated for three cases with linear boundary conditions and mean surface geometries. The three different cases are :

- near-field open boundary problem,
- closed boundary problem, and
- far-field open boundary problem.

In some instances, it is possible to determine an analytic solution for a stability region. The stability regions for each case are searched using one of the two numerical stability analysis methods. For some typical cases, time simulations are performed to verify the numerical stability regions. All stability regions are related to the Free Surface Stability parameter (FSS number), far-field closure treatment and the Green

Function constant **c**.

The analysis of these simplified problems is meant as a first step in understanding the more complex behavior of the nonlinear problems described in Chapter IV. The validity of the method will be demonstrated by comparing estimated stability boundaries with analytical values and the results of numerical simulation thus making the extension to the nonlinear analysis straightforward.

3.1 Linear Free Surface Boundary Conditions with Time-Stepping Schemes

It is not possible to obtain an analytic solution for the stability analysis of the nonlinear free surface boundary conditions with nonlinear free surface geometry. Therefore, the numerical stability analysis begins with the linear boundary conditions and linear geometry using the assumption that the nonlinear effect on stability is small in the limit of small wave slope. This hypothesis will be tested in Chapter IV. It is also assumed that the influence coefficient matrix is not changed during the time interval of interest. Within these assumptions, the characteristics of the linear stability study become the basis for the nonlinear stability analysis.

For the analytical and numerical investigation of this free surface flow problem, the more commonly used simple Euler schemes and fourth-order Runge-Kutta schemes are selected for time integration. Once the fluid domain is disturbed by the oscillation of a body, the free surface is deformed following the free surface conditions. These conditions are also used to estimate the potential ϕ on the deformed free surface at every time step.

The linear equivalent of the boundary conditions is obtained as shown below :

- Kinematic boundary condition

$$\frac{D(z-\eta)}{Dt} = 0 \qquad \xrightarrow{\text{linearize}} \qquad \eta_t = \phi_z \quad \text{on} \quad z = 0. \tag{3.1}$$

- Dynamic boundary condition

$$\frac{D\phi}{Dt} = -g\eta + \frac{1}{2}|\nabla\phi|^2 \xrightarrow{\text{linearize}} \phi_t = -g\eta \quad \text{on} \quad z = 0. \tag{3.2}$$

The subscript t means the derivative with respect to time and the subscript z means the derivative with respect to z. Other researchers are using different forms of this free surface condition. See Yeung(1982) for a comparison.

3.1.1 Simple Euler Schemes

The linearized forms of the free surface boundary conditions are given in Equations (3.1) and (3.2). The various Euler difference approximations for these equations are shown below :

- Explicit scheme

$$\begin{aligned} \frac{\eta^n - \eta^{n-1}}{\Delta t} &= \phi_z^{n-1} \\ \frac{\phi^{n+1} - \phi^n}{\Delta t} &= -g\eta^n \end{aligned}$$

$$\Rightarrow \qquad \phi^{n+1} - 2\phi^n + \phi^{n-1} = -g(\Delta t)^2 \phi_z^{n-1}, \tag{3.3}$$

- Implicit-like scheme

$$\begin{aligned} \frac{\eta^n - \eta^{n-1}}{\Delta t} &= \phi_z^{n-1} \\ \frac{\phi^{n+1} - \phi^n}{\Delta t} &= -g\eta^{n+1} \end{aligned}$$

$$\Rightarrow \qquad \phi^{n+1} - 2\phi^n + \phi^{n-1} = -g(\Delta t)^2 \phi_z^n. \tag{3.4}$$

The kinematic boundary condition is applied explicitly in both of the schemes. In the dynamic free surface boundary condition however, each scheme uses a different stage of the value of η to update the potential ϕ. Thus, the combined boundary conditions have different forms on their right-hand side as shown in Equations (3.3) and (3.4).

- Implicit Scheme

$$\begin{aligned} \frac{\eta^n - \eta^{n-1}}{\Delta t} &= \phi_z^n \\ \frac{\phi^{n+1} - \phi^n}{\Delta t} &= -g\eta^{n+1} \end{aligned}$$

$$\Rightarrow \qquad \phi^{n+1} - 2\phi^n + \phi^{n-1} = -g(\Delta t)^2 \phi_z^{n+1}$$

In the implicit scheme, ϕ_z at the (n+1) time step is used in the calculation of ϕ at the (n+1) time step.

3.1.2 Fourth-order Runge-Kutta Scheme

This scheme requires the calculation of several intermediate steps such as $\phi^{n+\frac{1}{2}}$ and $\eta^{n+\frac{1}{2}}$. Thus four iterations of the boundary value problem accompany each time step:

$$\phi^{n+1} = \phi^n + \frac{1}{6}(k_1 + 2k_2 + 2k_3 + k_4) \tag{3.5}$$

$$\eta^{n+1} = \eta^n + \frac{1}{6}(l_1 + 2l_2 + 2l_3 + l_4) \tag{3.6}$$

where k_i and l_i are the intermediate increments of ϕ and η respectively, or

$$k_1, k_2, k_3, l_1, l_2, l_3 \ : \text{ half time predictor}$$

$$k_4, l_4 \ : \text{ full time predictor.}$$

1. Simple explicit scheme

   In this scheme, all the intermediate $d\phi$ (such as k_1, k_2, k_3 or k_4) and $d\eta$ (such as l_1, l_2, l_3, or l_4) are calculated from the previous values. The increments k_1 and l_1 are calculated from the values of the (n) step. k_2 and l_2 are calculated from the values of the k_1 and l_1 intermediate step, and so on in a similar fashion for k_3 and l_3, and k_4 and l_4.

2. Implicit-like scheme

   In this scheme, $d\eta$ is calculated first at each intermediate time step and is used to get $d\phi$. Therefore, the increment l_i is calculated first and k_i later. This scheme has implicit characteristics compared to the explicit scheme even though ϕ or η for the $(n+1)$ time step are calculated explicitly.

3. Kang's method

   This is the method Kang(1988) used in his thesis for the calculation of the nonlinear three-dimensional oscillation problem with a wallsided body. This is very similar to the simple explicit scheme except that the calculation of the intermediate steps k_2, k_3, and k_4 are slightly different.

Refer to the Appendix C for more details about the fourth-order Runge-Kutta schemes. The appendix includes the derivation of the general fourth-order Runge-Kutta algorithm and the discretized forms of the above three schemes.

3.2 Solution of the Boundary Value Problem

To apply the free surface boundary condition in the Lagrangian step of the two-step method, the unknown ${\phi_n}^n$ on the free surface is calculated using the Boundary Integral Method (BIM). The BIM starts with Green's second identity and results in

an integral equation for the potential on the boundary. The potential $\phi(\vec{x})$ on the boundary point $\vec{x}$ of domain V is depicted as ;

$$\phi(\vec{x}) = -\int(\phi\frac{\partial G}{\partial n} - G\frac{\partial \phi}{\partial n})\,dl \tag{3.7}$$

where G is the Green function of Equation (2.13) or Equation (2.14) in Chapter II. Poisson equation.

Discretizing the surface with panels (3-D) or line segments (2-D), the potential ϕ at the (i) panel or segment is approximated as ;

$$\phi_i(\vec{x}) = -\sum\left\{\phi_j\int_{\Delta x_j}\frac{\partial G_{ij}}{\partial n_j}dl_j - (\frac{\partial \phi}{\partial n})_j\int_{\Delta x_j}G_{ij}dl_j\right\} \tag{3.8}$$

where

ϕ_j : known on the free surface

$\frac{\partial \phi_j}{\partial n_j}$: unknown on the free surface

and

ϕ_j *or* $(\frac{\partial \phi}{\partial n})_j$: one is known and the other is unknown on the remaining surfaces S_B, S_{bottom}, and S_∞ (3-D) or ℓ_B, ℓ_{bottom}, and ℓ_∞ (2-D).

In the linear problem, $\frac{\partial \phi}{\partial n} \rightarrow \frac{\partial \phi}{\partial z}$ on the free surface. These thesis will consider three types of enclosing surfaces. The first used in the near-field, open boundary problem (Figure 3.2) has vertical boundary surfaces ℓ_∞ on both sides, the bottom surface ℓ_{bottom} at infinite depth, and the free surface ℓ_F. Second, the closed boundary problem (Figure 3.8) has the body surface ℓ_B, the far-field bounding surface ℓ_∞, the finite bottom surface ℓ_{bottom}, and the free surface ℓ_F. The last surface, used in the far-field, open boundary problem (Figure 3.22), has the body surface ℓ_B (2-D) or S_B (3-D), far-field truncated surface ℓ_∞ (2-D) or S_∞ (3-D), far-field bounding contour ℓ_c (2-D) or S_c (3-D), and the free surface ℓ_F (2-D) or S_F (3-D).

In matrix form, Equation (3.8) can be expressed as

$$\begin{bmatrix} & & \\ & A_{ij} & \\ & & \end{bmatrix} \left\{ \begin{array}{c} \vdots \\ \hline \frac{\partial \phi}{\partial n} \\ \vdots \end{array} \right\} = \begin{bmatrix} & & \\ & B_{ij} & \\ & & \end{bmatrix} \left\{ \begin{array}{c} \vdots \\ \hline \phi \\ \vdots \end{array} \right\}$$

or

$$\left\{ \begin{array}{c} \vdots \\ \hline \frac{\partial \phi}{\partial n} \\ \vdots \end{array} \right\} = \begin{bmatrix} & & \\ & C_{ij} & \\ & & \end{bmatrix} \left\{ \begin{array}{c} \vdots \\ \hline \phi \\ \vdots \end{array} \right\} = \left[\begin{array}{c|c} [C^1] & [C^2] \\ \hline [C^3] & [C^*] \end{array} \right] \left\{ \begin{array}{c} \vdots \\ \hline \phi \\ \vdots \end{array} \right\}$$

where the first m entries in the left-hand column are the unknown potential or unknown normal derivative values on the bottom boundary ℓ_{bottom}, body boundary ℓ_B, and the far-field boundary ℓ_∞ and the rest of the entries in the left-hand column are the unknown normal derivatives of the potential on the free surface ℓ_F. The $[C]$ matrix is the multiplication of the $[A]^{-1}$ and the $[B]$ matrices (*i.e.* $[C] = [A]^{-1}[B]$).

A subset of the above matrices is made by retaining only the terms needed to complete the time step on the free surface :

$$\left\{ \begin{array}{c} \frac{\partial \phi}{\partial n} \\ \vdots \end{array} \right\} = \left[[C^3][C^*] \right] \left\{ \begin{array}{c} \vdots \\ \hline \phi \\ \vdots \end{array} \right\} = [C^3] \left\{ \begin{array}{c} \frac{\partial \phi}{\partial n} \text{ or } \phi \\ \vdots \end{array} \right\} + [C^*] \left\{ \begin{array}{c} \phi \\ \vdots \end{array} \right\} \tag{3.9}$$

$$= \sum_{j=f.s.}^{N} C^*_{ij}\phi_j + \sum_{j=non\ f.s.} C^3_{ij} \cdot \left((\frac{\partial \phi}{\partial n})_j \text{ or } \phi_j \right) \tag{3.10}$$

$$\equiv [C^*] \left\{ \begin{array}{c} \phi \\ \vdots \end{array} \right\} + \left\{ \begin{array}{c} f \\ \vdots \end{array} \right\} \tag{3.11}$$

where $[C^*]$ is the subset of the influence coefficient matrix [C] which is related to the free surface only. C^*_{ij} is the influence coefficient of the (j) free surface panel to the (i) free surface panel. The column $\{f\}$ is the multiplication of C^3_{ij} and the known values

of ϕ_j or $(\frac{\partial\phi}{\partial n})_j$ on all surfaces except the free surface. In this way, it acts as a forcing function. This summation form, Equation (3.10), is substituted to the Equations (3.1) $\sim$ (3.4) to study the numerical stability characteristics of the different time stepping schemes. Yeung(1982) and Dommermuth *et al.*(1988) ignored this step by simply assuming that ${\phi_n}^n = k\phi^n$ before performing a numerical stability analysis. By ignoring this step, their results do not include any relationship between the solution of the boundary value problem and the boundary conditions. In particular, Yeung's stability analysis is only a function of time step size Δt. However, as shown later in this thesis, the stability characteristics have an important relationship between the panel size, Δx, the surface geometry, and the boundary condition type, in addition to the time increment.

As an example of the matrix formation, if ϕ_n is given and ϕ is unknown on the boundaries excluding the free surface, $[A_{ij}]$ and $[B_{ij}]$ then become

$$\left[\begin{array}{c} \\ A_{ij} \\ \\ \end{array}\right] \left\{\begin{array}{c} \phi \\ \vdots \\ \hline \phi_n \\ \vdots \end{array}\right\} \equiv \left[\begin{array}{c|c} \frac{1}{2}I_{ij}+ & \\ \int_{\Delta x_j} \frac{\partial G_{ij}}{\partial n_j} dl_j & -\int_{\Delta x_j} G_{ij} dl_j \end{array}\right] \left\{\begin{array}{c} \phi \\ \vdots \\ \hline \phi_n \\ \vdots \end{array}\right\} \tag{3.12}$$

$$\left[\begin{array}{c} \\ B_{ij} \\ \\ \end{array}\right] \left\{\begin{array}{c} \phi_n \\ \vdots \\ \hline \phi \\ \vdots \end{array}\right\} \equiv \left[\begin{array}{c|c} & -\frac{1}{2}I_{ij} \\ \int_{\Delta x_j} G_{ij} dl_j & -\int_{\Delta x_j} \frac{\partial G_{ij}}{\partial n_j} dl_j \end{array}\right] \left\{\begin{array}{c} \phi_n \\ \vdots \\ \hline \phi \\ \vdots \end{array}\right\} \tag{3.13}$$

Each component of $[A_{ij}]$ and $[B_{ij}]$ matrices is calculated by an integration on the panel segment with the Green function G or its normal derivative $\frac{\partial G}{\partial n}$. I_{ij} is the identity matrix.

3.3 Numerical Stability of Mixed Eulerian-Lagrangian Method

The impact problem deals with the body striking the fluid at relatively high velocities. Real fluids have very complicated characteristics such as viscosity, turbulancy, compressibility, *etc.* which generally are simplified through mathematical modeling. The mathematical model of the problem should contain the problem's essential characteristics. Existence and uniqueness should be satisfied but not necessarily proven for the modeling to be valid. After the model has been formed, the solution can be determined through analytic calculation, numerical analysis, or experiment. By solving the idealized problem from which non-essential effects have been removed, a fundamental understanding of the governing physics is possible.

Now, focusing on the model analysis and its resulting stability characteristics, there are three possible ways for instabilities in the numerical results to occur :

1. The physical problem has inherent instabilities.

2. In simplifying the physical problem to the mathematical model, mathematical instabilities can be created.

3. In converting the mathematical formulation to a numerical formulation, numerical instabilities can be generated.

If the instability is sufficiently investigated to insure that it is due to item 3, the numerical instability can be removed or avoided by selecting certain parameter ranges.

In this work, the panel method is selected for the solution of Laplace's equation and several Euler schemes or fourth-order Runge-Kutta schemes are used for the time-stepping evolution. Thus, the combinations of this proposed methodology are going to be investigated for numerical stability. Figure 3.1 shows the stencil for the

numerical calculation of the free surface flow problem. To find ϕ at the (j) panel on the $(n+2)$ time step, the values of ϕ on all boundaries at the $(n+1)$ time step are needed. This reflects the combined nature of the elliptic and parabolic partial differential equations associated with the mixed Eulerian-Lagrangian method.

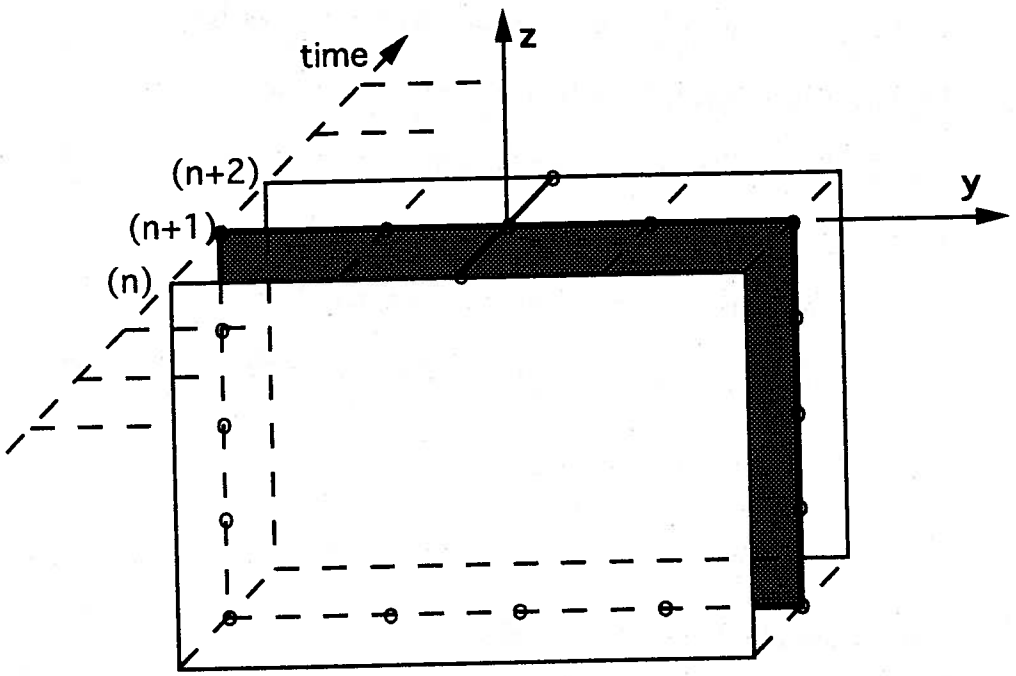

Figure 3.1: Stencil of the numerical method for the free surface evolutions. Example shows the stencil for the Implicit-like scheme

3.3.1 von Neumann Analysis

There are two well-known methods to investigate the numerical stability of time-stepping algorithms. The first, and most direct, is the von-Neumann analysis ([3],[53]).

A numerical calculation produces a numerical solution, N. The numerical solution N is considered to be composed of the exact value, D, and an error, ε. The error,

$\varepsilon(\vec{x},t)$, can be assumed to be written as a series of sine and cosine terms. The ratio between the error at the (n) time step and the error at the $(n+1)$ time step is defined as the magnification factor, G. The magnification factor $G(=\frac{\varepsilon_j^{n+1}}{\varepsilon_j^n})$ for the (j) point in the computational grid should be less than 1 in magnitude for the numerical algorithm to be stable. It follows, then

$$\mathrm{N} = \mathrm{D} + \varepsilon \tag{3.14}$$

where

N : numerical solution computed using a real machine with finite accuracy,

D : exact solution of the equation, and

ε : error in the numerical solution due to round-off.

For the free surface problem then, the potential ϕ is considered to be composed of an exact value, ϕ_{exact}, and the numerical error, $\varepsilon(x,t)$. The numerical error, $\varepsilon(x,t)$, can be expressed as a Fourier series expansion :

$$\phi = \phi_{exact} + \varepsilon(x,t) \tag{3.15}$$

$$\varepsilon(x,t) = \sum_{m=1}^{\infty} b_m(t)\, e^{ik_m x} = \sum_{m=1}^{\infty} e^{at} e^{ik_m x} \tag{3.16}$$

$$\varepsilon_j^n = e^{an\Delta t} e^{ik_m j\Delta x} \tag{3.17}$$

'a' may be complex and k_m is real.

Applying Equations (3.15) $\sim$ (3.17) to the linearized free surface boundary conditions using the Euler scheme results in

$$\left(\begin{array}{c} \phi_t = -g\eta \\ \\ \eta_t = \phi_z \end{array} \right) \longrightarrow \phi_{tt} = -g\,\phi_z$$

$$\phi^{n+1} - 2\phi^n + \phi^{n-1} = -g(\Delta t)^2 \, \phi_z^\gamma \tag{3.18}$$

$$\text{where} \quad \begin{cases} \gamma = n-1 & \text{for the explicit scheme} \\ \gamma = n & \text{for the implicit-like scheme.} \\ \gamma = n+1 & \text{for the implicit scheme} \end{cases}$$

The potential derivative ϕ_z^γ on the free surface (*i.e.* the right-hand side of Equation (3.18)) is obtained through the application of the BIM in Equation (3.10) such as:

$$\{\phi_{zi}\}^\gamma = \left[[C^3][C^*]\right] \left\{ \begin{array}{c} \phi_{nj} \text{ or } \phi_j \\ \vdots \\ \hline \phi_j \\ \vdots \end{array} \right\}^\gamma = [C^*]\{\phi_j\}^\gamma + \{f_j\}^\gamma \tag{3.19}$$

$$\text{and} \quad \phi_j^\gamma = \phi_{j_{exact}}^\gamma + \varepsilon_j^\gamma \tag{3.20}$$

where $\{\phi_{zi}\}^\gamma$ is the potential derivative of the (i) panel on the free surface at the (n) or $(n+1)$ time step and $[C^*]$ is the submatrix related to the free surface potential $\{\phi_j\}^\gamma$. The submatrix $[C^3]$ forms the equivalent of an external exciting function $\{f\}^\gamma$ through the multiplication of the known values. Substituting Equations (3.19) $\sim$ (3.20) into Equation (3.18) and cancelling common terms yields the equation for the magnification factor $G(= \frac{\varepsilon^{n+1}}{\varepsilon^n})$:

$$\begin{cases} G^2 - 2G + (1-\alpha) = 0 \ \text{(Explicit scheme)} \\ G^2 - (2+\alpha)G + 1 = 0 \ \text{(Implicit} - \text{like scheme)} \\ (1-\alpha)G^2 - 2G + 1 = 0 \ \text{(Implicit scheme)} \end{cases}$$

where α is a function of discretized panel length, Δx, time-step size, Δt and the Green function constant, **c**.

The solution of the quadratic equation for the magnification factor G above has two roots. These two roots can have pure real values or complex values and the moduli of the roots are associated with the following stability characteristics :

$$\begin{aligned} &\text{If } |G| > 1, \quad \text{then the time stepping algorithm is unstable.} \\ &\text{If } |G| = 1, \quad \text{then the time stepping algorithm is neutrally stable.} \\ &\text{If } |G| < 1, \quad \text{then the time stepping algorithm is stable.} \end{aligned} \tag{3.21}$$

If one modulus of the two roots is larger than 1, then the scheme is not stable and is called to be 'unconditionally unstable'. If the larger one of the two roots has the modulus 1 in some region, the scheme is said to be 'neutrally stable' in that region. In this neutrally stable region, the error is neither growing nor dissipating. If the moduli of both roots are less than 1, then the scheme is said stable.

Applying the von Neumann numerical stability analysis to the linearized free surface boundary conditions

$$\begin{pmatrix} \phi_t = -g\eta \\ \eta_t = \phi_z \end{pmatrix}$$

using the fourth-order Runge-Kutta Explicit scheme results in the following equations. Refer to Equation (C.8) in Appendix C for the next derivation.

$$\phi^{n+1} = \phi^n - g\Delta t\{\eta^n + \frac{1}{6}(d\eta_1 + d\eta_2 + d\eta_3)\}$$

$$\Rightarrow \quad \phi^{n+1} = \phi^n - g\Delta t\{\eta^n + \frac{\Delta t}{6}[(\phi_z)_1^{n+\frac{1}{2}} + (\phi_z)_2^{n+\frac{1}{2}} + (\phi_z)_3^{n+1}]\} \tag{3.22}$$

$$\phi^{n+2} = \phi^{n+1} - g\Delta t\{\eta^{n+1} + \frac{\Delta t}{6}[(\phi_z)_1^{n+\frac{3}{2}} + (\phi_z)_2^{n+\frac{3}{2}} + (\phi_z)_3^{n+2}]\} \tag{3.23}$$

Subtract Equation (3.23) from Equation (3.22) , then

$$\begin{aligned} \phi^{n+2} - 2\phi^{n+1} + \phi^n = -\frac{g(\Delta t)^2}{6}\{ &\phi_z^n + (\phi_z)_1^{n+\frac{1}{2}} + (\phi_z)_2^{n+\frac{1}{2}} \\ &+(\phi_z)_1^{n+\frac{3}{2}} + (\phi_z)_2^{n+\frac{3}{2}} + (\phi_z)_3^{n+2}\} \end{aligned} \tag{3.24}$$

The magnification factor associated with Equation (3.24) becomes a fifth-order algebraic equation even though $(\phi_x)_3^{n+2}$ is assumed to be a function of ϕ^{n+2}. It may not be possible to get the analytic solution for the various roots. The other modified fourth-order Runge-Kutta schemes also have similar fifth-order algebraic equations for which the roots must be found. Consequently, the von Neumann analysis to determine the stability region for the fourth-order Runge-Kutta scheme is completed numerically. The magnification factor G has the same characteristics as explained before in Equation (3.21). If any modulus of the five roots is larger than 1, the scheme is unconditionally unstable.

3.3.2 Matrix Stability

The disadvantage of von Neumann's approach is that it does not directly include the effects of the boundaries, and therefore gives only approximate stability criteria. A more general, but more computationally intensive way to establish stability criteria is the Matrix Method ([53]). This method will now be applied to the two free surface boundary conditions :

$$\phi_t = -g\,\eta$$

$$\eta_t = \phi_z = [C^*]\phi + f.$$

The discretized system of the two boundary conditions can be written in matrix

form

$$\begin{Bmatrix} \phi \\ \vdots \\ \eta \\ \vdots \end{Bmatrix}^{n+1} = \begin{bmatrix} & & \\ & D_{ij} & \\ & & \end{bmatrix} \begin{Bmatrix} \phi \\ \vdots \\ \eta \\ \vdots \end{Bmatrix}^{n} + \begin{Bmatrix} 0 \\ \vdots \\ f \\ \vdots \end{Bmatrix}^{n} . \tag{3.25}$$

where $[D]$ is a $(2N \times 2N)$ matrix and N represents the number of panels on the free surface. If any one of the absolute values of the $2 * N$ eigenvalues of $[D]$ is larger than 1, then the marching scheme is unstable (See [3].). The formation of the $[D]$ matrix is decided according to the choice of numerical schemes. It follows that the eigenvalues of the [D] matrix have a meaning very similar to that of the roots of the magnification factor G in the von Neumann analysis.

(1) Explicit Euler scheme

The difference equations using the explicit Euler scheme is as follows ;

$$\phi^{n+1} = \phi^n - g\,\Delta t\,\eta^n \tag{3.26}$$

$$\eta^{n+1} = \eta^n + \Delta t \sum_{j=1}^{N} C^* \phi_j^n + f^n \tag{3.27}$$

or combined into matrix form :

$$\left\{\begin{array}{c} \phi \\ \vdots \\ \hline \eta \\ \vdots \end{array}\right\}^{n+1} = \left[\begin{array}{cc|cc} 1 & 0 & -g\Delta t & 0 \\ 0 & \ddots & 0 & \ddots \\ \hline & & 1 & 0 \\ \Delta t\, C^* & & & \\ & & 0 & \ddots \end{array}\right] \left\{\begin{array}{c} \phi \\ \vdots \\ \hline \eta \\ \vdots \end{array}\right\}^{n} + \left\{\begin{array}{c} 0 \\ \vdots \\ \hline f \\ \vdots \end{array}\right\}^{n} \tag{3.28}$$

As can be seen in Equation (3.28), the $[D]$ matrix of the explicit Euler scheme is composed of two identity matrices, one $-g\,\Delta t * [I]$ matrix, and the $\Delta t\,[C^*]$ matrix which is a subset of the [C] matrix. The $[C^*]$ matrix is a result of the BIM and plays

the most important role in the [D] matrix.

(2) Implicit-like Euler scheme

The difference equations using the implicit-like scheme are as follows :

$$\phi^{n+1} = \phi^n - g\,\Delta t\,\eta^{n+1} \tag{3.29}$$

$$\eta^{n+1} = \eta^n + \Delta t \sum_{j=1}^{N} C^* \phi_j^n + f^n \tag{3.30}$$

with a matrix representation of

$$\left[\begin{array}{cc|cc} 1 & 0 & g\Delta t & 0 \\ 0 & \ddots & 0 & \ddots \\ \hline 0 & 0 & 1 & 0 \\ 0 & \ddots & 0 & \ddots \end{array}\right] \left\{\begin{array}{c} \phi \\ \vdots \\ \hline \eta \\ \vdots \end{array}\right\}^{n+1} = \left[\begin{array}{cc|cc} 1 & 0 & 0 & 0 \\ 0 & \ddots & 0 & \ddots \\ \hline & & 1 & 0 \\ \Delta t\, C^* & & 0 & \ddots \end{array}\right] \left\{\begin{array}{c} \phi \\ \vdots \\ \hline \eta \\ \vdots \end{array}\right\}^{n} + \left\{\begin{array}{c} 0 \\ \vdots \\ \hline f \\ \vdots \end{array}\right\}^{n}$$

To construct the [D] matrix of Equation (3.25) using the implicit-like Euler scheme, the inverse of the matrix on the left-hand side of the above equation should be multiplied on both sides. The [D] matrix for this scheme also includes the $[C^*]$matrix and this $[C^*]$ matrix has a large influence on the eigenvalues of the [D] matrix.

(3) Fourth-order Runge-Kutta schemes

The difference equations using the fourth-order Runge-Kutta schemes start with

$$\phi^{n+1} = \phi^n + \frac{1}{6}(k_1 + 2k_2 + 2k_3 + k_4)$$

$$\eta^{n+1} = \eta^n + \frac{1}{6}(l_1 + 2l_2 + 2l_3 + l_4)$$

All the intermediate values are represented as the summation of the influence coefficient matrix $[C^*]$ and the forcing function. Each element of the $[D]$ matrix is composed of triply summed expressions. The detailed procedure for the derivation and formation of the $[D]$ matrix is in Appendix C.

3.4 Near-Field Open Boundary Problem

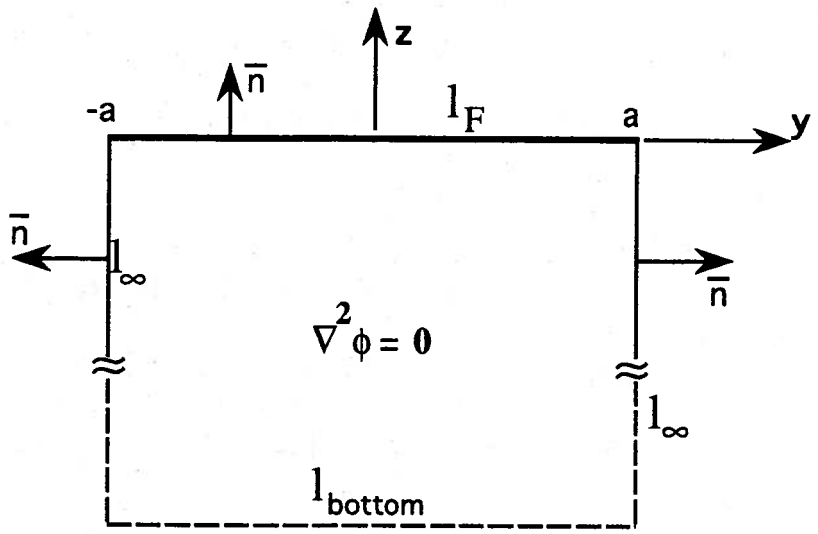

Figure 3.2: Model for near-field open boundary problem

With the numerical stability analysis methods described in Section 3.3, the numerical stability region for various cases is now investigated. As an initial step, the simplest example of the stability analysis in the free surface problem is considered. This example is defined as the Near-Field Open Boundary Problem. Figure 3.2 shows the computational domain and the coordinate system of this example. The fluid volume, V, is surrounded by the free surface, ℓ_F, and the far-field boundary, ℓ_∞, on both sides. The water depth, h, is considered to be infinitely deep. This is the simplest example where the stability analysis can be performed. The closed form solution to this Near-Field Open Boundary Problem contains many of the stability characteristics of the more complicated free surface problems. The potential and its normal derivative, ϕ and ϕ_n, on both side boundaries are given as the solution of the plane, progressive wave moving from left to right. On the free surface, the potential is

initially given and the derivative of potential, ϕ_n, is unknown. The potential on the free surface satisfies the kinematic and dynamic boundary conditions and in domain V, Laplace's equation. The unknown ϕ_n on free surface is calculated by the BIM and the new potential ϕ on the free surface is calculated by free surface boundary conditions. The analytic solution to plane progressive waves and its derivatives are shown below :

$$\phi(y,z;t) = \mathrm{Re}\{A\,e^{kz}e^{i(ky-\omega t)}\} = A\,e^{kz}\cos(ky-\omega t) \tag{3.31}$$

$$\phi_y(y,z;t) = -kA\,e^{kz}\sin(ky-\omega t) \tag{3.32}$$

$$\phi_z(y,z;t) = kA\,e^{kz}\cos(ky-\omega t) \tag{3.33}$$

where k is wave number, ω is the wave frequency, and A is the amplitude of the potential ϕ. The free surface is divided into a number of panels, and an initial ϕ is given on that surface. The boundary value problem is solved to get $\frac{\partial\phi}{\partial n}$ on the free surface, which is next used to calculate the new potential values of the free surface.

The modified Green function is used in the solution of the integral equation. In the following sections, the effect of **c** (an additional constant in the Green function) on the stability of the free surface problem is investigated with different Euler schemes to find the stable region. The analytic form of the numerical stability region is derived as a function of **c**. Numerical simulations for specific cases are performed to check whether the numerical stability region obtained analytically coincides with the results of the simulation by varying $\frac{\pi g(\Delta t)^2}{\Delta x}$ and $c\Delta x$. The comparison shows a very good coincidence between the analytic results and simulation.

The general solution for the velocity potential is

$$\phi(\vec{x},t) = -\frac{1}{\pi}\oint_{l_f+l_\infty+l_b}\left\{\phi_n(\vec{\xi},t)\,\ln \mathbf{c}|\vec{x}-\vec{\xi}| + \phi(\vec{\xi},t)\frac{\vec{n}(\vec{\xi})\cdot(\vec{x}-\vec{\xi})}{|\vec{x}-\vec{\xi}|^2}\right\}d\xi. \tag{3.34}$$

Substitute Equations (3.31) ~ (3.33) into Equation (3.34) and the far-field integral becomes

$$
\begin{aligned}
&-\frac{1}{\pi}\int_{l_\infty}\{\quad\}d\xi \\
&\quad= \frac{kA}{2\pi}\sin(ka+\omega t)\int_0^\infty e^{-k\zeta}\ln(\{c(y+a)\}^2+\{c(z+\zeta)\}^2)d\zeta \\
&\quad+\frac{kA}{2\pi}\sin(ka-\omega t)\int_0^\infty e^{-k\zeta}\ln(\{c(y-a)\}^2+\{c(z+\zeta)\}^2)d\zeta \\
&\quad+\frac{(y+a)A}{\pi}\cos(ka+\omega t)\int_0^\infty \frac{e^{-k\zeta}}{(y+a)^2+(z+\zeta)^2}d\zeta \\
&\quad-\frac{(y-a)A}{\pi}\cos(ka-\omega t)\int_0^\infty \frac{e^{-k\zeta}}{(y-a)^2+(z+\zeta)^2}d\zeta. \qquad (3.35)
\end{aligned}
$$

The free surface and the body integrals are

$$
\begin{aligned}
-\frac{1}{\pi}\int_{l_F}\{\quad\}d\xi &= \text{effect from other panels on the free surface} \\
&\quad + \text{self induced effect} \\
-\frac{1}{\pi}\int_{l_B}\{\quad\}d\xi &= 0 \text{ (no body introduced)}
\end{aligned}
$$

3.4.1 Single Panel

For this case, only one panel of length $\Delta x = 2a$ is used on the free surface and the field point is at the origin, the center of the panel. Applying the von Neumann stability analysis to the kinematic and dynamic boundary conditions, the numerical stability equation is obtained as a function of magnification factor G and the analytic form of the stability region can be derived. The control point $\vec{x}$ is located at the center of the panel.

$$\vec{x} = (y, z) = (0, 0)$$

From Equations (3.31) ~ (3.33) and (3.35),

$$
\begin{aligned}
-\frac{1}{\pi}\int_{l_\infty}\{\quad\}d\xi &= \frac{2A}{\pi}\cos(\omega t)\{\sin(ka)\ln(ca)-\mathrm{si}(ka)\} \\
-\frac{1}{\pi}\int_{l_f}\{\quad\}d\xi &= -\frac{2a}{\pi}(\ln(ca)-1)\frac{\partial\phi}{\partial n}(\vec{x})
\end{aligned}
$$

where si(ka) is the sine integral (pp. 231 $\sim$ 232 [1]) and c is the Green function constant. Then, Equation (3.34) becomes

$$\phi(\vec{x},t) = -\frac{1}{\pi}\int_{l_f+l_\infty}\left\{\phi_n(\vec{\xi},t)\,\ln \mathrm{c}|\vec{x}-\vec{\xi}| + \phi(\vec{\xi},t)\frac{\vec{n}(\vec{\xi})\cdot(\vec{x}-\vec{\xi})}{|\vec{x}-\vec{\xi}|^2}\right\}d\xi$$

$$= \frac{2A}{\pi}\cos(\omega t)\{\sin(ka)\ln(\mathrm{c}a) - \mathrm{si}(ka)\}$$

$$-\frac{2a}{\pi}\{\ln(ca)-1\}\frac{\partial\phi}{\partial n}(\vec{x})$$

or $$\phi(0,0) = FG(1) - A_{11}\frac{\partial\phi}{\partial n}(0,0) \tag{3.36}$$

where $A_{11} = \frac{2a}{\pi}\{\ln(ca)-1\}$ and $FG(1) = -\frac{1}{\pi}\int_{l_\infty}\{\quad\}d\xi$.

Therefore, the unknown $\frac{\partial\phi}{\partial n}(0,0)$ on the free surface is

$$\frac{\partial\phi}{\partial n}(0,0) = \frac{FG(1)}{A_{11}} - \frac{\phi(0,0)}{A_{11}}. \tag{3.37}$$

This solution $\frac{\partial\phi}{\partial n}(0,0)$ from the BIM is used in Step 2, the time stepping of the kinematic and dynamic free surface boundary conditions.

(1) Explicit Euler Method

Equation (3.37) is introduced into the right hand side of the combined free surface boundary condition explicitly :

$$\frac{\phi^{n+2}-2\phi^{n+1}+\phi^n}{(\Delta t)^2} = -g\phi_z^n = -g\{\frac{FG^n(1)}{A_{11}} - \frac{\phi^n}{A_{11}}\} \tag{3.38}$$

and the stability equation becomes

$$G^2 - 2G + \{1 - \frac{\pi g(\Delta t)^2}{2a(\ln(\mathrm{c}a)-1)}\} = 0 \tag{3.39}$$

For this scheme to be stable, Equation (3.39) must have two roots which satisfy the condition on the magnification factor, $|G| \le 1$.

- If $\mathrm{c}a > e$: One of the two roots of $|G|$ is larger than 1.

  (no region for stability)

- If $ca < e$: The forms of the two roots of G are $1\pm$ (some complex number). Therefore, at least, one of two roots of $|G|$ is always larger than 1. (no region for stability)

There is no region where the modulus of both roots are less than or equal to 1 for any value of ca. Therefore, the Explicit Euler Method is **unconditionally unstable** for this problem.

(2) Implicit-like Euler Method

The difference form of the free surface equations become

$$\frac{\phi^{n+2} - 2\phi^{n+1} + \phi^n}{(\Delta t)^2} = -g\phi_x^{n+1} = -g\{\frac{FG^{n+1}(1)}{A_{11}} - \frac{\phi^{n+1}}{A_{11}}\} \tag{3.40}$$

$$\text{or} \quad \phi^{n+2} - \{2 - \frac{g(\Delta t)^2}{A_{11}}\}\phi^{n+1} + \phi^n = g(\Delta t)^2\frac{FG^{n+1}(1)}{A_{11}}. \tag{3.41}$$

Following the von Neumann analysis, the stability equation is

$$G^2 - \{2 + \frac{\pi g(\Delta t)^2}{2a(\ln(ca) - 1)}\}G + 1 = 0 \tag{3.42}$$

So, the stability region is defined by the following relation :

$$\frac{\pi g(\Delta t)^2}{2a} \;<\; -4\,(\ln ca - 1). \tag{3.43}$$

Thus, the Implicit-like Euler Method is **conditionally stable.**

(3) Matrix stability of the implicit-like Euler method

For this single panel case, the matrix stability analysis shows the same equation as that of the von Neumann analysis for the stability region. Applying the matrix stability analysis to the implicit-like Euler method using Equations (3.29) $\sim$ (3.30) and (3.37) gives :

$$\begin{aligned} \phi^{n+1} &= \phi^n - g\,\Delta t\,\eta^{n+1} \\ \eta^{n+1} &= \eta^n + \Delta t\frac{FG(1) - \phi^n}{A_{11}} \end{aligned}$$

or in matrix form

$$\begin{bmatrix} 1 & g\Delta t \\ 0 & 1 \end{bmatrix} \begin{Bmatrix} \phi \\ \eta \end{Bmatrix}^{n+1} = \begin{bmatrix} 1 & 0 \\ -\frac{\Delta t}{A_{11}} & 1 \end{bmatrix} \begin{Bmatrix} \phi \\ \eta \end{Bmatrix}^{n} + \begin{Bmatrix} 0 \\ f \end{Bmatrix}^{n} \tag{3.44}$$

$$\Rightarrow \begin{Bmatrix} \phi \\ \eta \end{Bmatrix}^{n+1} = \begin{bmatrix} 1 & -g\Delta t \\ 0 & 1 \end{bmatrix} \begin{bmatrix} 1 & 0 \\ -\frac{\Delta t}{A_{11}} & 1 \end{bmatrix} \begin{Bmatrix} \phi \\ \eta \end{Bmatrix}^{n} + \begin{Bmatrix} 0 \\ f \end{Bmatrix}^{n} \tag{3.45}$$

$$\text{with} \qquad [D_{ij}] = \begin{bmatrix} 1 + \frac{g(\Delta t)^2}{A_{11}} & -g\Delta t \\ -\frac{\Delta t}{A_{11}} & 1 \end{bmatrix}. \tag{3.46}$$

The eigenvalues of $[D_{ij}]$, λ, satisfy the equation

$$(1 + \frac{g(\Delta t)^2}{A_{11}} - \lambda)(1 - \lambda) - \frac{g(\Delta t)^2}{A_{11}} = 0 \tag{3.47}$$

which is identical to Equation (3.42).

The solid curve of Figure 3.3 shows the analytic stability region for the case of a single panel on the free surface. The horizontal axis represents the value of **c a** and the vertical axis represents the FSS (Free Surface Stability) number. Several time simulations were performed to confirm the analytical curve of Equation (3.43) shown in Figure 3.3. The background markers show the simulation results of the potential value on the free surface by varying the conditions of two parameters, **ca** and FSS number. For each condition, the potential value was checked as to whether it diverged or not for up to 200 time steps. These results coincide very well with the analytic curve. A fundamental conclusion of this example is that the stability of an algorithm may be changed by redefining the Green function. This will be shown to be true for some, but not for all the cases considered in this work. Generally, for open boundary problems the stability can be influenced by **c**. As will be shown, for closed boundary problems, the stability is independent of **c**.

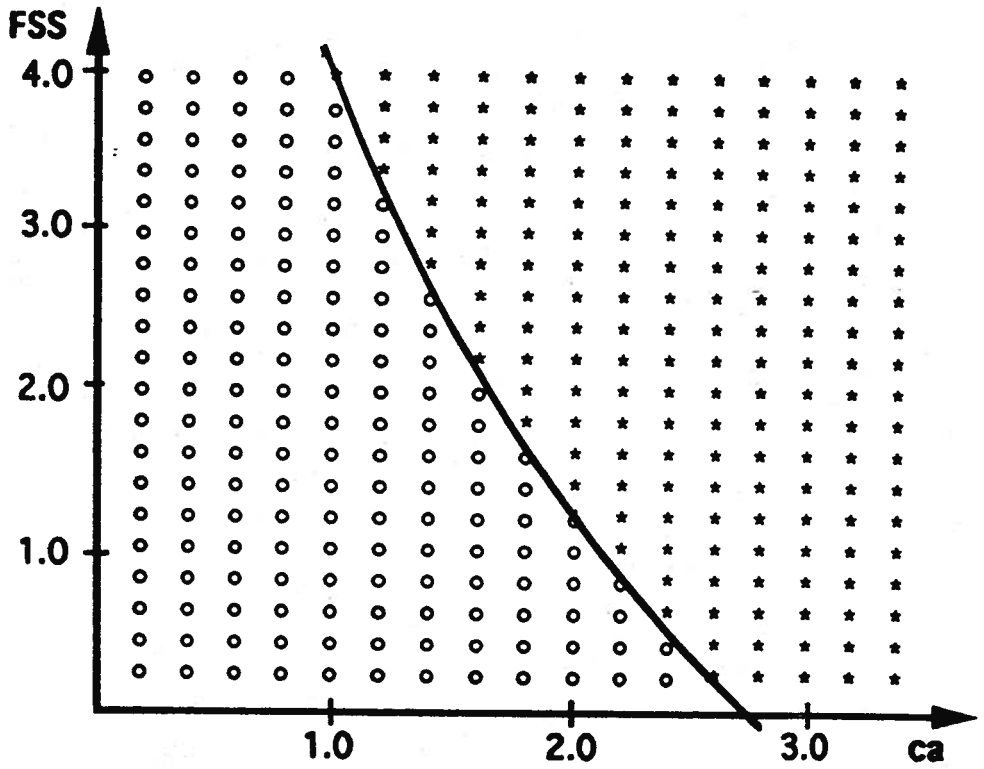

Figure 3.3: Time simulations with different parametric conditions for the one panel case of the near-field open boundary problem. Included is the analytic curve of Equation (3.43), $FSS \leq -4(\ln ca - 1)$. Time marching was based upon the implicit-like Euler scheme. (o : stable simulation, $*$: unstable simulation)

3.4.2 Multiple Panels

Now the number of panels on the free surface is increased. The length is kept the same as that of Section 3.4.1, $2a = N\Delta x$ where N is the number of panels on the free surface. The analytic form of the stability curve is derived and time simulations of this problem confirm the stability region.

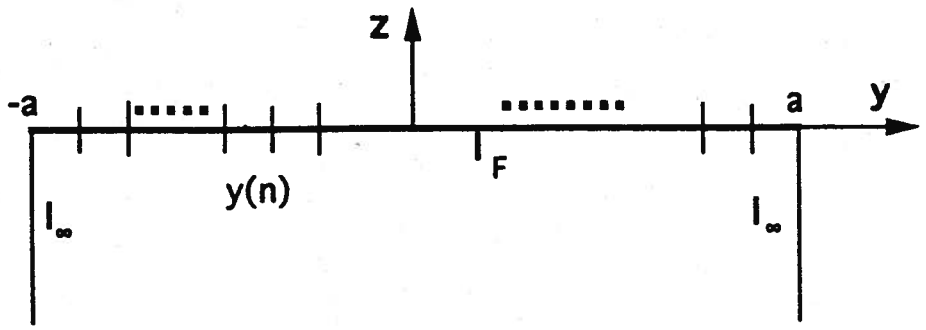

Figure 3.4: Multi-panels of near-field open boundary problem.

The values of the y ordinates on the free surface are

$$\begin{aligned} y(1) &= -a + \frac{a}{N} = \frac{a(1-N)}{N} = \frac{\Delta x(1-N)}{2} \\ y(n) &= -a + \frac{2an}{N} - \frac{a}{N} = \frac{a(2n-1-N)}{N} = \frac{\Delta x(2n-1-N)}{2} \end{aligned}$$

where $y(n)$ is the location of the (n) control point. See Figure 3.4.

The solution for the velocity potential is

$$\begin{aligned} \phi(y(n)) = \frac{A}{\pi}[\, & 2\sin(ka)\cos(\omega t)\ln\frac{ca}{N} + \sin(ka+\omega t)\ln(2n-1) \\ & + \sin(ka-\omega t)\ln(2N+1-2n)] \\ + \frac{A}{\pi}[\, & \sin(ka+\omega t)\, FG2(\frac{ka(2n-1)}{N}) \\ & + \sin(ka-\omega t)\, FG2(\frac{ka(2N+1-2n)}{N}) \end{aligned}$$

$$
\begin{aligned}
&+\cos(ka+\omega t)\,FG1\left(\frac{ka(2n-1)}{N}\right)\\
&+\cos(ka-\omega t)\,FG1\left(\frac{ka(2N+1-2n)}{N}\right)]\\
&-\frac{2a}{N\pi}\sum_{j=2}^{n}\frac{\partial\phi}{\partial n}(n+1-j)[\ln\frac{ca}{N}-1+\frac{1}{2}\ln\frac{(2j-1)^{2j-1}}{(2j-3)^{2j-3}}]\\
&-\frac{2a}{N\pi}\sum_{j=2}^{N-(n-1)}\frac{\partial\phi}{\partial n}(j+n-1)[\ln\frac{ca}{N}-1+\frac{1}{2}\ln\frac{(2j-1)^{2j-1}}{(2j-3)^{2j-3}}]\\
&-\frac{2a}{N\pi}\frac{\partial\phi}{\partial n}(n)\,(\ln\frac{ca}{N}-1)
\end{aligned}
$$

where

$$
\begin{cases}
FG1(z) &= \mathrm{ci}(z)\sin(z)-\mathrm{si}(z)\cos(z)\\
FG2(z) &= -\mathrm{ci}(z)\cos(z)-\mathrm{si}(z)\sin(z)\\
\dfrac{2a}{N} &= \Delta x \qquad\rightarrow\qquad ka=\dfrac{kN\Delta x}{2}\\
\text{and} &\quad \mathrm{si}(z)\text{ and }\mathrm{ci}(z)\text{ are the sine and cosine integrals respectively}\\
&\quad \text{(See pp. 231 - 232 of [1])}
\end{cases}
$$

Rewrite $\phi(y(n))$ as

$$
\begin{aligned}
\phi(y(n))=FG(n)\ &-A_{1n}\frac{\partial\phi}{\partial n}(1)-A_{1(n-1)}\frac{\partial\phi}{\partial n}(2)-\cdots-A_{12}\frac{\partial\phi}{\partial n}(n-1)\\
&-A_{11}\frac{\partial\phi}{\partial n}(n)-A_{12}\frac{\partial\phi}{\partial n}(n+1)-\cdots-A_{1(N-n+1)}\frac{\partial\phi}{\partial n}(N)
\end{aligned}
\tag{3.48}
$$

where

$$
\begin{aligned}
FG(n)=\frac{A}{\pi}[\,&2\sin(ka)\cos(\omega t)\ln\frac{ca}{N}+\sin(ka+\omega t)\ln(2n-1)\\
&+\sin(ka-\omega t)\ln(2N+1-2n)]\\
+\frac{A}{\pi}[\,&\sin(ka+\omega t)\,FG2\left(\frac{ka(2n-1)}{N}\right)\\
&+\sin(ka-\omega t)\,FG2\left(\frac{ka(2N+1-2n)}{N}\right)\\
&+\cos(ka+\omega t)\,FG1\left(\frac{ka(2n-1)}{N}\right)\\
&+\cos(ka-\omega t)\,FG1\left(\frac{ka(2N+1-2n)}{N}\right)]
\end{aligned}
$$

and

$$
\begin{aligned}
A_{11} &= \frac{2a}{N\pi}\{\ln\frac{ca}{N} - 1\} \\
A_{12} &= \frac{2a}{N\pi}\{\ln\frac{ca}{N} - 1 + \frac{1}{2}\ln 3^3\} \\
A_{1n} &= \frac{2a}{N\pi}\{\ln\frac{ca}{N} - 1 + \frac{1}{2}\ln\frac{(2n-1)^{2n-1}}{(2n-3)^{2n-3}}\} \\
A_{1N} &= \frac{2a}{N\pi}\{\ln\frac{ca}{N} - 1 + \frac{1}{2}\ln\frac{(2N-1)^{2N-1}}{(2N-3)^{2N-3}}\}
\end{aligned}
$$

Equation (3.48) can be described in matrix form,

$$
\begin{bmatrix}
A_{11} & A_{12} & A_{13} & \cdots & A_{1N} \\
A_{12} & A_{11} & A_{12} & \cdots & A_{1(N-1)} \\
A_{13} & A_{12} & A_{11} & \cdots & A_{1(N-2)} \\
\vdots & \vdots & \vdots & \vdots & \vdots \\
A_{1N} & A_{1(N-1)} & A_{1(N-2)} & \cdots & A_{11}
\end{bmatrix}
\begin{Bmatrix}
\frac{\partial\phi}{\partial n}(1) \\ \frac{\partial\phi}{\partial n}(2) \\ \frac{\partial\phi}{\partial n}(3) \\ \vdots \\ \frac{\partial\phi}{\partial n}(N)
\end{Bmatrix}
=
\begin{Bmatrix}
FG(1) - \phi(1) \\ FG(2) - \phi(2) \\ FG(3) - \phi(3) \\ \vdots \\ FG(N) - \phi(N)
\end{Bmatrix}
$$

or

$$
\begin{Bmatrix}
\frac{\partial\phi}{\partial n}(1) \\ \frac{\partial\phi}{\partial n}(2) \\ \frac{\partial\phi}{\partial n}(3) \\ \vdots \\ \frac{\partial\phi}{\partial n}(N)
\end{Bmatrix}
= [A^{-1}]
\begin{Bmatrix}
FG(1) \\ FG(2) \\ FG(3) \\ \vdots \\ FG(N)
\end{Bmatrix}
- [A^{-1}]
\begin{Bmatrix}
\phi(1) \\ \phi(2) \\ \phi(3) \\ \vdots \\ \phi(N)
\end{Bmatrix}
$$

This $\frac{\partial\phi}{\partial n}$ at the (j) panel is substituted into the combined linearized free surface boundary condition. In the linear analysis, $\frac{\partial\phi}{\partial z}$ is used for $\frac{\partial\phi}{\partial n}$. The location index will appear as a subscript from now on, that is $\frac{\partial\phi}{\partial n}(i) = \left(\frac{\partial\phi}{\partial n}\right)_i$, $FG(i) = FG_i$.

(1) Explicit Method for the (j) panel, von Neumann analysis

The difference form of the free surface equation for the multi-panel case becomes

$$
\frac{\phi_j^{n+2} - 2\phi_j^{n+1} + \phi_j^n}{(\Delta t)^2} = -g\phi_{zj}^n
$$

$$\phi_j^{n+2} - 2\phi_j^{n+1} + \phi_j^n - g(\Delta t)^2 \sum_{m=1}^{N} (A_{jm}^{-1}\phi_m^n) = -g(\Delta t)^2 \sum_{m=1}^{N} (A_{jm}^{-1} F G_m^n) \tag{3.49}$$

Substituting $\phi = \phi_{exact} + \epsilon(x,t)$ into Equation (3.49) above gives the equation for the magnification factor G as

$$G_j^2 - 2G_j + \{1 - g(\Delta t)^2 (A_{j1}^{-1} e^{-i(j-1)\beta} + A_{j2}^{-1} e^{-i(j-2)\beta} + \cdots + A_{jj}^{-1} + A_{j,j-1}^{-1} e^{i\beta} + \cdots + A_{jN}^{-1} e^{i(N-j)\beta})\} = 0$$

The solution of the above quadratic equation is easily shown to be

$$G_j = 1 \pm \sqrt{g(\Delta t)^2 (A_{j1}^{-1} e^{-i(j-1)\beta} + A_{j2}^{-1} e^{-i(j-1)\beta} + \cdots)} \tag{3.50}$$

where $\beta = k\Delta x$, and k is a wave number related to the error. Equation (3.50) shows that the magnitude of at least one of the two roots is greater than 1 ($|G| \geq 1$).

Therefore, no region of stability exists. Similar to the single panel problem in Equation (3.39), the explicit Euler method for the multiple-panel also is **unconditionally unstable.**

(2) Implicit-like Method at the (j) panel, von Neumann analysis

The free surface difference equation for the implicit-like method becomes

$$\frac{\phi_j^{n+2} - 2\phi_j^{n+1} + \phi_j^n}{(\Delta t)^2} = -g\phi_{xj}^{n+1} \tag{3.51}$$

$$\phi_j^{n+2} - 2\phi_j^{n+1} - g(\Delta t)^2 \sum_{m=1}^{N} (A_{jm}^{-1}\phi_m^{n+1}) + \phi_j^n = -g(\Delta t)^2 \sum_{m=1}^{N} (A_{jm}^{-1} \mathrm{FG}_m^{n+1}). \tag{3.52}$$

In Equation (3.51), ϕ_{xj} at the $(n+1)$ time step is used instead of ϕ_{xj} at the (n) time step as in the explicit scheme. The equation for the magnification factor is

derived by the substitution of $\phi = \phi_{exact} + \epsilon$ into Equation (3.52) :

$$G_j^2 - \{2 + g(\Delta t)^2(A_{j1}^{-1}e^{-i(j-1)\beta} + A_{j2}^{-1}e^{-i(j-2)\beta} + \cdots + A_{jj}^{-1} + A_{j,j-1}^{-1}e^{i\beta} + \cdots + A_{jN}^{-1}e^{i(N-j)\beta})\}G_j + 1 = 0 \quad (3.53)$$

For the numerical scheme to be stable, the magnitude of the two roots of Equation (3.53) should be less than or equal to 1.

Therefore, the region of the stability is defined by

$$\begin{aligned} &\Rightarrow \quad g(\Delta t)^2 < \frac{-4}{\sum_{m=1}^{N} A_{jm}^{-1}} && \text{if } \beta = 0 \\ &\Rightarrow \quad g(\Delta t)^2 < \frac{-4}{\sum_{m=1}^{N} (-1)^{m+j} A_{jm}^{-1}} && \text{if } \beta = \pi \\ &\Rightarrow \quad g(\Delta t)^2 < \frac{-4}{\sum_{m=1}^{N} (A_{jm}^{-1} \cos(m-j)\beta)} && \text{if } 0 < \beta \leq \pi. \end{aligned} \quad (3.54)$$

The implicit-like Euler method for the multi-panel is also **conditionally stable.** Refer to Appendix D for the detailed procedure to find the region when both roots have a magnitude less than or equal to 1.

The stability region for the third panel of twenty is shown in Figure 3.5. Each curve represents the stability lines for $\beta = 0,\ \pi/2,\ \pi$, respectively. The wave number β is related to the wave length of the numbered round-off error, $\epsilon(x,t)$, Equation (3.16). Since ϵ is assumed to be random, no one characteristic wave number can be identified. Hence, for the scheme to be stable, $|G|$ must be less than 1.0 for all β. Figure 3.6 shows the stability regions of the five panels on the free surface. As shown on Figure 3.6, the stability region is changing along the free surface with the lowest FSS number in the middle of the free surface. For the free surface problem to be stable, the minimum FSS number should be chosen from Figure 3.6. Inspection of Figure 3.6 suggests that the more stable panels (*i.e.* the panels whose stability is less sensitive to round-off error) are located near the truncation boundaries. For the

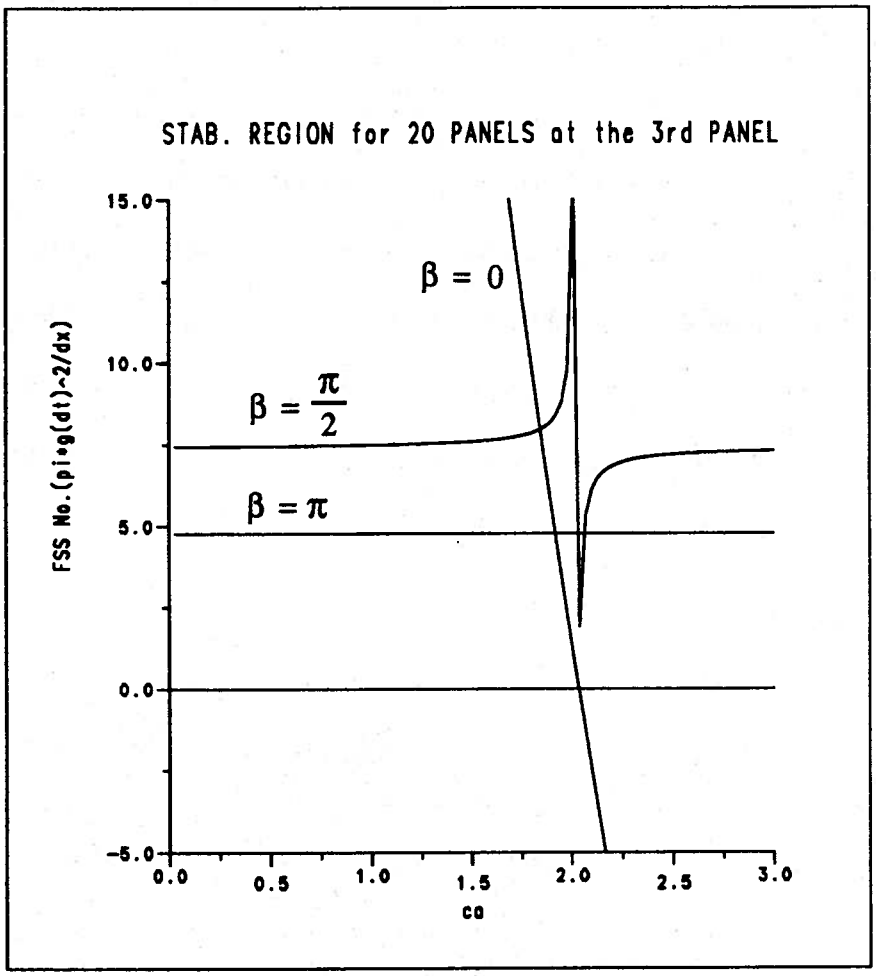

Figure 3.5: Stability region for a multi panel case of the Near-Field Open Boundary problem. This figure shows the stability region for the third panel of a twenty panel free surface domain. The normalized wave number β varies from 0 to π. The curves are drawn to satisfy Equation (3.54). The time marching is based upon the implicit-like Euler scheme.

Near-Field Open Boundary Problem, instabilities associated with numerical errors should initiate near the center and propagate towards the sides. This observation will be verified for the more general problems discussed in the following sections. See Figure 3.17 in Section 3.5.2.

Simulation results are plotted in Figure 3.7 for several typical conditions and the results verify the curves shown in Figure 3.5. To ensure the analytic stability region, Equation (3.54), time simulations for the free surface problem are performed by varying ca and FSS number with twenty panels on the free surface. If the time simulation goes up to 200 time steps without the potential diverging, 'o' is marked in the tested condition. Otherwise '$*$' is marked. The simulated stable region of Figure 3.7 falls within the area bounded by $\beta = 0$ and $\beta = \pi$, Equation (3.54).

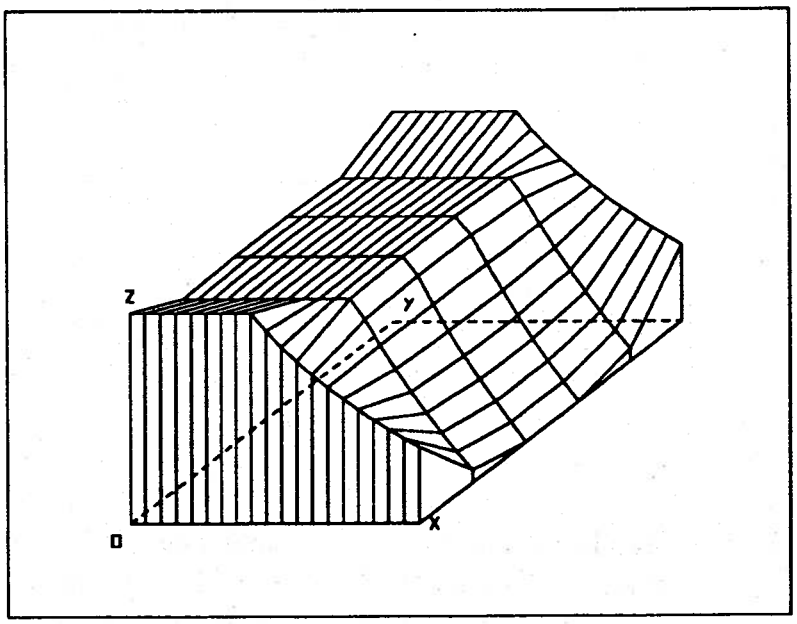

Figure 3.6: Different stability regions for 5 panels on free surface (x axis : ca, y axis : free surface, z axis : FSS number). The curves are drawn to satisfy Equation (3.54).

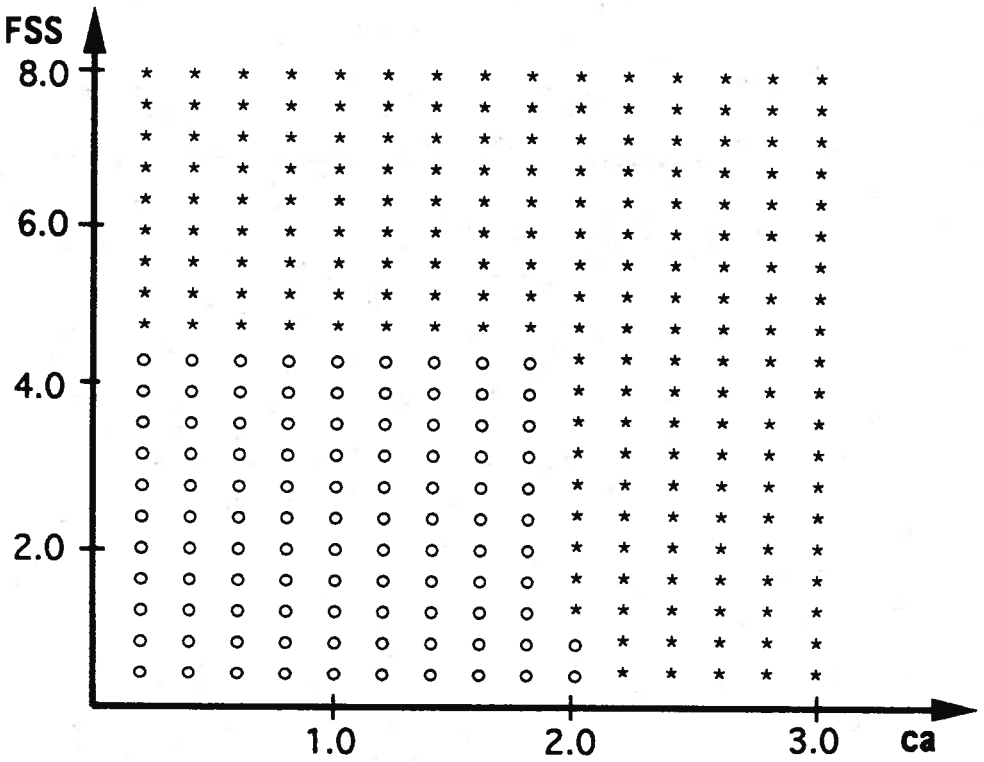

Figure 3.7: Time simulation plots for the multi-panel case of the Near-Field Open Boundary problem with implicit-like Euler scheme. (20 panels on the free surface, o : stable simulation, * : unstable simulation)

3.5 Closed Boundary Problem

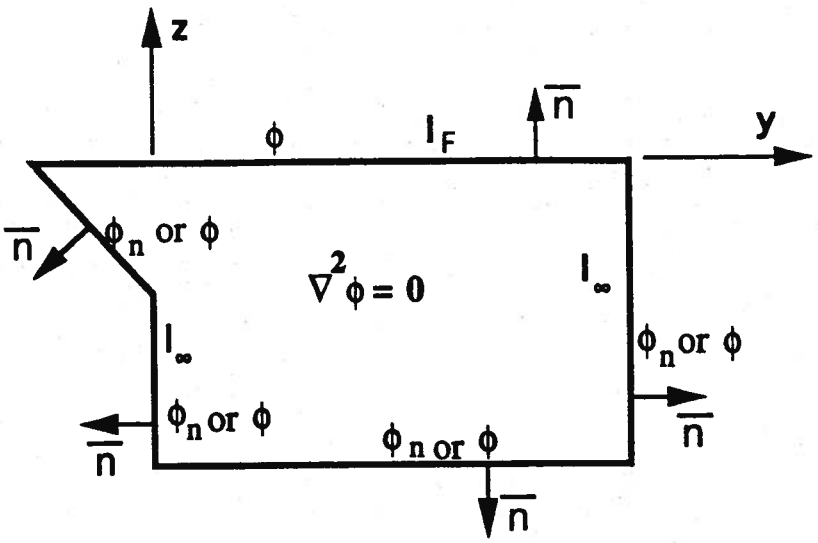

Figure 3.8: Model for the closed boundary problem.

In this section, the complexity of the model is increased to include unknown potentials or derivatives on finite far-field or bottom boundaries. The model geometry and the coordinate system are depicted in Figure 3.8. The free surface boundary condition is imposed on top and ϕ or ϕ_n on the other sides. For the purpose of simulation, the initial conditions on the free surface and other boundaries are given as those of a plane progressive wave. This may be thought of as the far-field solution to the wave maker problem.

The stability criterion is considered for the following cases :

1) Change the non-free surface boundary condition type (ϕ or $\frac{\partial\phi}{\partial n}$).

2) Use von Neumann analysis and Matrix analysis.

3) Use the several kinds of different time-stepping schemes (Euler schemes and fourth-order Runge-Kutta schemes).

4) Consider various shapes like triangles, rectangles and polygons.

Time simulations are performed to illustrate the behavior of each. For a number of special cases, stability boundaries corresponding to time simulation results are compared with the stability boundaries predicted by eigenvalues of the matrix method. Instability types are studied relative to the complex value of the maximum eigenvalue. The accuracy of the numerical simulation is also checked as a function of wave number.

3.5.1 Square Panel

A square panel is considered as the simplest case for the closed boundary problem. One panel is located on the free surface, one panel on the bottom, and one panel on each side. The geometry of the boundary and its coordinate system is shown in Figure 3.9. The boundary value problem is solved with the mixed Eulerian-Lagrangian method. Both a von Neumann stability analysis and a matrix stability analysis are applied in this section. The results of the analytic analysis for the numerical stability are checked with the numerical simulations, varying FSS number ($\frac{\pi g(\Delta t)^2}{\Delta x}$) and $\mathbf{c}\Delta x$.

The equations below represent the case of ϕ given on the free surface and ϕ_n given on the other sides. The approach is quite general and the results for other combinations of ϕ and ϕ_n are shown in Table 3.1 and Figure 3.16.

Following Equation (3.8), the solution for the potential is

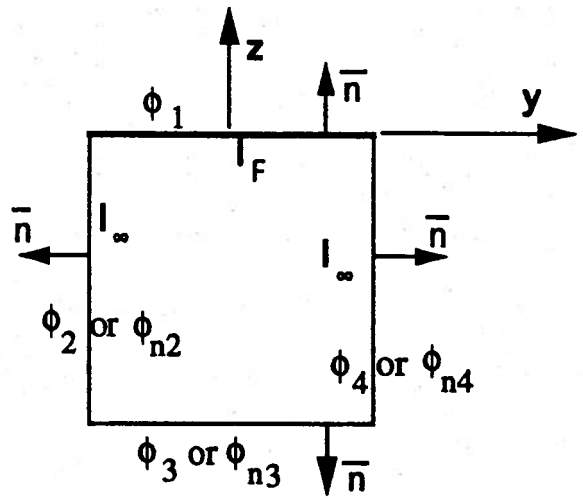

Figure 3.9: Geometry of the square panel of the closed boundary problem. The potential ϕ is given on the top panel and ϕ or ϕ_n for the other panels.

$$\begin{aligned}
\phi_1 = \; & -\frac{2a}{\pi}(\ln ca - 1)\frac{\partial \phi_1}{\partial n} \\
& -\frac{\phi_2}{\pi}(-\tan^{-1} 2) - \frac{1}{\pi}\frac{\partial \phi_2}{\partial n} 2a(\ln \sqrt{5}\, ca - 1 + \frac{1}{2}\tan^{-1} 2) \\
& -\frac{\phi_3}{\pi}(-\tan^{-1} 2) - \frac{1}{\pi}\frac{\partial \phi_3}{\partial n} 2a(\ln \sqrt{5}\, ca - 1 + \frac{1}{2}\tan^{-1} 2) \\
& -\frac{\phi_4}{\pi}(-2\tan^{-1}\frac{1}{2}) - \frac{1}{\pi}\frac{\partial \phi_4}{\partial n} 2a(\ln \sqrt{5}\, ca - 1 + \frac{1}{2}\tan^{-1} 2)
\end{aligned}$$

or more generally

$$\phi_1 = A\frac{\partial \phi_1}{\partial n} + B\phi_2 + C\frac{\partial \phi_2}{\partial n} + B\phi_3 + C\frac{\partial \phi_3}{\partial n} + D\phi_4 + E\frac{\partial \phi_4}{\partial n} \qquad (3.55)$$

$$\phi_2 = B\phi_1 + C\frac{\partial \phi_1}{\partial n} + A\frac{\partial \phi_2}{\partial n} + D\phi_3 + E\frac{\partial \phi_3}{\partial n} + B\phi_4 + C\frac{\partial \phi_4}{\partial n} \qquad (3.56)$$

$$\phi_3 = B\phi_1 + C\frac{\partial \phi_1}{\partial n} + D\phi_2 + E\frac{\partial \phi_2}{\partial n} + A\frac{\partial \phi_3}{\partial n} + B\phi_4 + C\frac{\partial \phi_4}{\partial n} \qquad (3.57)$$

$$\phi_4 = D\phi_1 + E\frac{\partial \phi_1}{\partial n} + B\phi_2 + C\frac{\partial \phi_2}{\partial n} + B\phi_3 + C\frac{\partial \phi_3}{\partial n} + A\frac{\partial \phi_4}{\partial n} \qquad (3.58)$$

where

$$A = -\frac{2a}{\pi}(\ln ca - 1)$$

$$B = \frac{1}{\pi}\tan^{-1} 2$$

$$C = -\frac{2a}{\pi}(\ln\sqrt{5}\,ca - 1 + \frac{1}{2}\tan^{-1} 2)$$

$$D = \frac{2}{\pi}\tan^{-1}\frac{1}{2}$$

$$E = -\frac{2a}{\pi}(\ln\sqrt{5}\,ca - 1 + 2\tan^{-1}\frac{1}{2}).$$

Rewrite Equations (3.55) $\sim$ (3.58) in matrix form for the case of (ϕ_1, ϕ_{n_2}, ϕ_{n_3}, ϕ_{n_4}) known and (ϕ_{n_1}, ϕ_2, ϕ_3, ϕ_4) unknown, then

$$\begin{bmatrix} \\ A_{ij} \\ \\ \end{bmatrix} \begin{Bmatrix} \frac{\partial\phi_1}{\partial n} \\ \phi_2 \\ \phi_3 \\ \phi_4 \end{Bmatrix} = \begin{bmatrix} \\ B_{ij} \\ \\ \end{bmatrix} \begin{Bmatrix} \phi_1 \\ \frac{\partial\phi_2}{\partial n} \\ \frac{\partial\phi_3}{\partial n} \\ \frac{\partial\phi_4}{\partial n} \end{Bmatrix}$$

and multiplying $[A]^{-1}$ on both sides to find

$$[A]^{-1}[A] = [I]$$

$$[A]^{-1}[B] \equiv [C]$$

$$\begin{Bmatrix} \frac{\partial\phi_1}{\partial n} \\ \phi_2 \\ \phi_3 \\ \phi_4 \end{Bmatrix} = \begin{bmatrix} \\ C_{ij} \\ \\ \end{bmatrix} \begin{Bmatrix} \phi_1 \\ \frac{\partial\phi_2}{\partial n} \\ \frac{\partial\phi_3}{\partial n} \\ \frac{\partial\phi_4}{\partial n} \end{Bmatrix}$$

where the unknown normal velocity is

$$\Rightarrow \qquad \frac{\partial\phi_1}{\partial n} = C_{11}\phi_1 + \sum_{j=2}^{4} C_{1j}\,\phi_{nj}^{n} \qquad (3.59)$$

Equation (3.59) is an analytic solution form for $\frac{\partial\phi}{\partial n}$ on the free surface assuming that the given potential on the free surface and the normal derivatives on the other surfaces are constant over each panel or segment. Applying the free surface boundary conditions advances the potential value on the evolved location which for the

linear problem remains in its mean position. The form of the linearized free surface condition is repeated here as

$$\phi_{tt} = -g\phi_z. \tag{3.60}$$

Recall that for the linearized problem, the term $\sum_{j=2}^{4} C_{1j}\,\phi_{nj}^{n}$ of Equation (3.59) plays no role in determining the stability characteristics. It acts as an exciting force in the stability equation. In the following subsections, Equation (3.60) is solved with various numerical schemes when Equation (3.59) is substituted into ϕ_z.

(1) Explicit Euler scheme

The free surface difference equation for the closed boundaries become

$$\phi_1^{n+2} - 2\phi_1^{n+1} + \phi_1^n = -g(\Delta t)^2\{C_{11}\phi_1^n + \sum_{j=2}^{4} C_{1j}\,\phi_{nj}^n\}$$

Following a von Neumann stability analysis yields the quadratic equation for the magnification factor

$$G^2 - 2G + 1 = -g(\Delta t)^2 C_{11}$$

$$\text{or} \quad G^2 - 2G + \{1 + g(\Delta t)^2 C_{11}\} = 0.$$

There is no region where $|G| \leq 1$. Therefore, no stability region exists. So, the explicit Euler scheme is **unconditionally unstable** for the square panel of closed boundary problem.

(2) Implicit-like Euler scheme

The difference equation for the implicit-like Euler scheme is

$$\phi_1^{n+2} - 2\phi_1^{n+1} + \phi_1^n = -g(\Delta t)^2\{C_{11}\phi_1^{n+1} + \sum_{j=2}^{4} C_{1j}\phi_{nj}^{n+1}\} \tag{3.61}$$

which has the associated quadratic equation for the magnification factor

$$G^2 - 2G + 1 = -g(\Delta t)^2 C_{11} G$$

$$\text{or} \quad G^2 - \{2 - g(\Delta t)^2 C_{11}\} G + 1 = 0.$$

The stability region is

$$0 < \frac{g(\Delta t)^2}{2} C_{11} < 2 \tag{3.62}$$

Therefore, the implicit-like Euler scheme is **conditionally stable** in the region where the Equation (3.62) is satisfied. Refer to Appendix D for the procedure to find the stability region of Equation (3.62)

Table 3.1 is the list of the stability regions according to the various boundary condition types for the square panel. This table shows that the boundary condition type can play an important role in determining the numerical stability limit. It also implies that the stable region shown by Dommermuth and Yue (*i.e.* $FSS \leq 8$) sometimes could be unstable. The notation $(\phi_1, \phi_{n2}, \phi_3, \phi_4)$ means ϕ is known on the panels 1, 3, and 4, and ϕ_n is known on panel 2. Here, panel 1 represents the free surface. The stability limit for each boundary condition type is also graphically shown on Figure 3.16.

Time simulations for the square panel are performed for the various ranges of ca and FSS number and typical results are shown in Figure 3.10. For each case, the values of ca and FSS number are fixed and a time simulation is performed. If the simulation continues successfully through 200 time steps, a '*o*' is marked for the test condition. If the simulation diverges, a '*' is marked. For the simulation with a $(\phi_1, \phi_{n2}, \phi_3, \phi_4)$ boundary condition, the results show good comparison with the analytic stability region of Figure 3.16.

Figure 3.11 is the case for a very small FSS number with small $c\,\Delta x$. In this case,

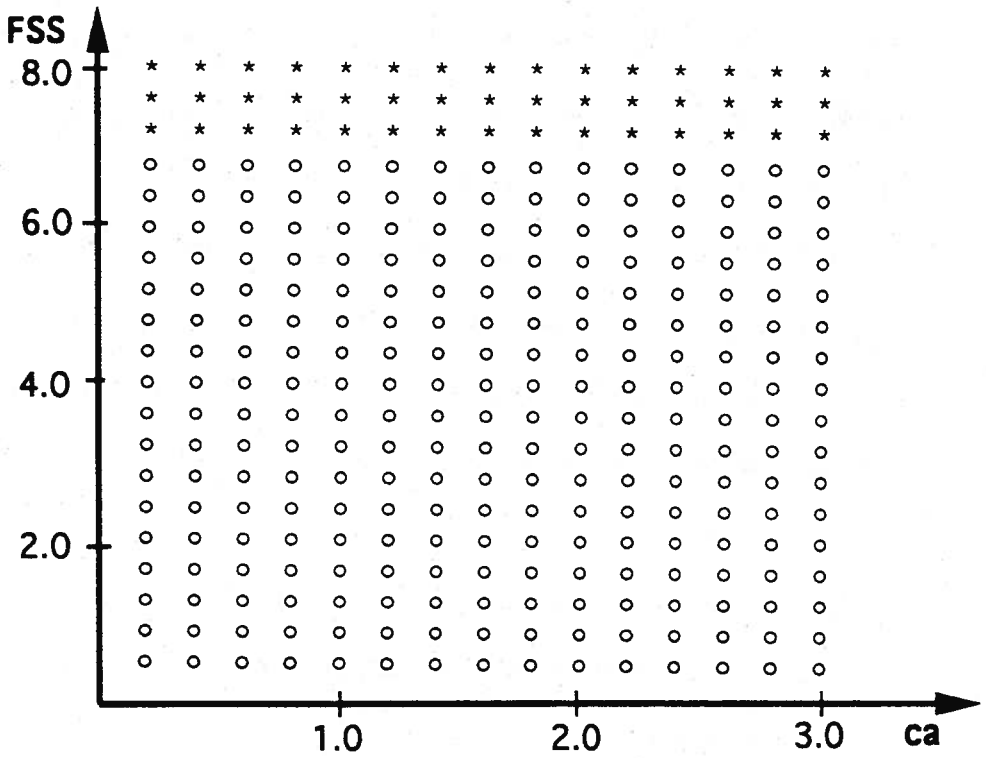

Figure 3.10: Stability region of the square panel by simulation (o : stable simulation, $*$: unstable simulation). $(\phi_1, \phi_{n2}, \phi_3, \phi_4)$ given boundary condition with implicit-like Euler scheme.

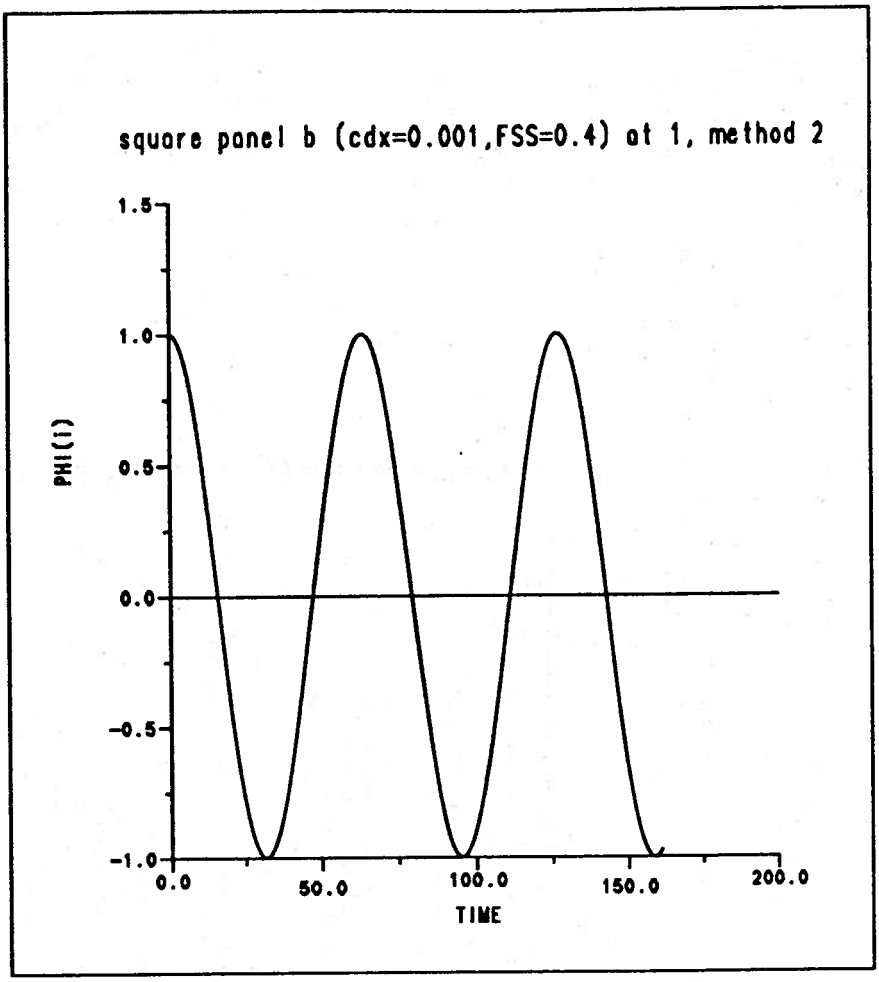

Figure 3.11: Time simulation of the square panel. Boundary conditions given as $(\phi_1, \phi_{n2}, \phi_3, \phi_4)$ with implicit-like Euler scheme for time marching. $ka = 0.001$, FSS number $= 0.4$.

the simulation shows a high accuracy with stability. Keeping $c\,\Delta x$ small, the FSS number is increased to the stability limit to investigate the transition phenomena from a stable to unstable region (Figure 3.12). Figure 3.12 shows the sawtooth contamination on the crest and trough of the sine curve. With an incremental increase in the FSS number, the simulation diverges drastically as in Figure 3.15. Four test conditions for Figure 3.11 $\sim$ 3.15 are marked as circles in Figure 3.16. Figures 3.13 and 3.14 illustrate that the stability does not necessarily guarantee accuracy.

Figure 3.16 shows the various analytic stability regions according to the different

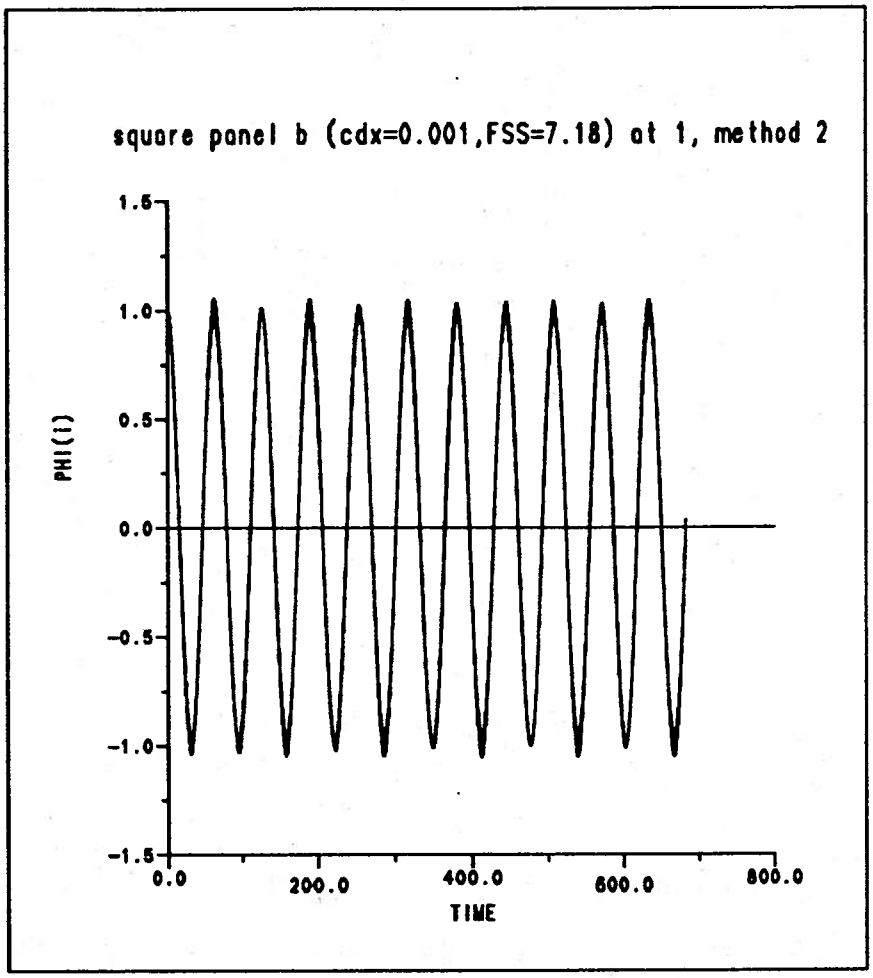

Figure 3.12: Time simulation of the square panel. Boundary conditions given as $(\phi_1, \phi_{n2}, \phi_3, \phi_4)$ with implicit-like Euler scheme for time marching. $ka = 0.001$, FSS number $= 7.180$.

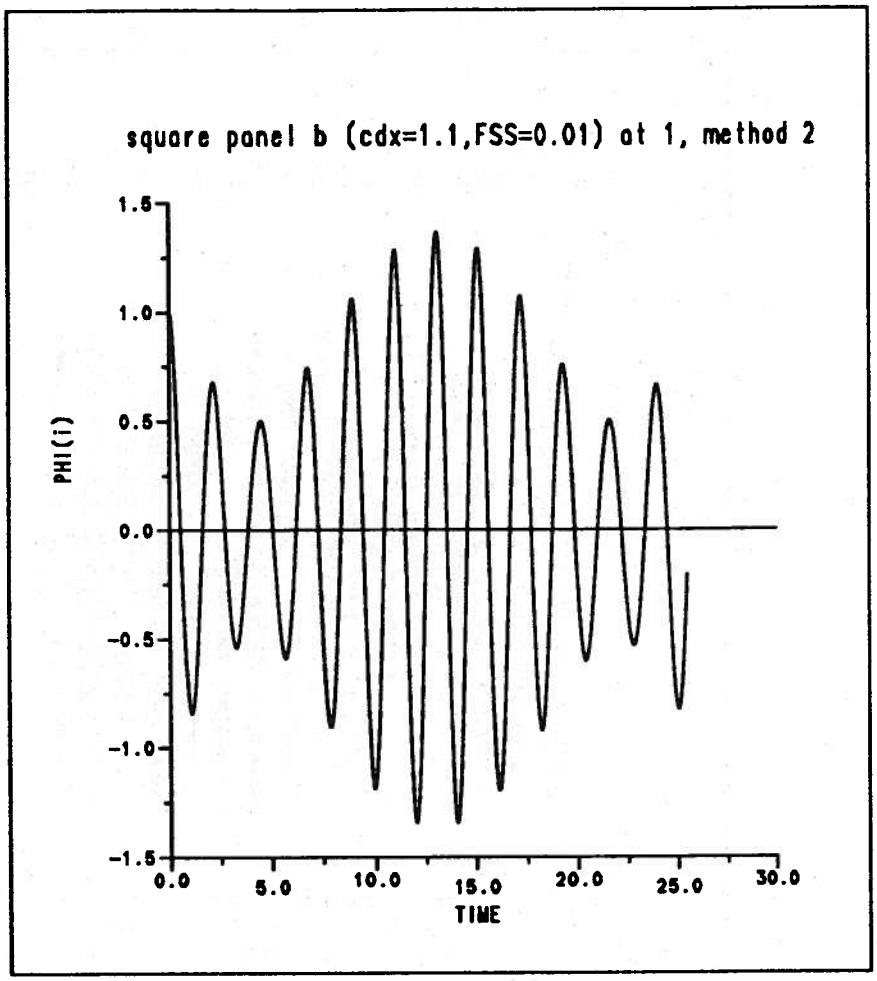

Figure 3.13: Time simulation of the square panel. Boundary conditions given as $(\phi_1, \phi_{n2}, \phi_3, \phi_4)$ with implicit-like Euler scheme for time marching. $ka = 1.1$, FSS number $= 0.01$.

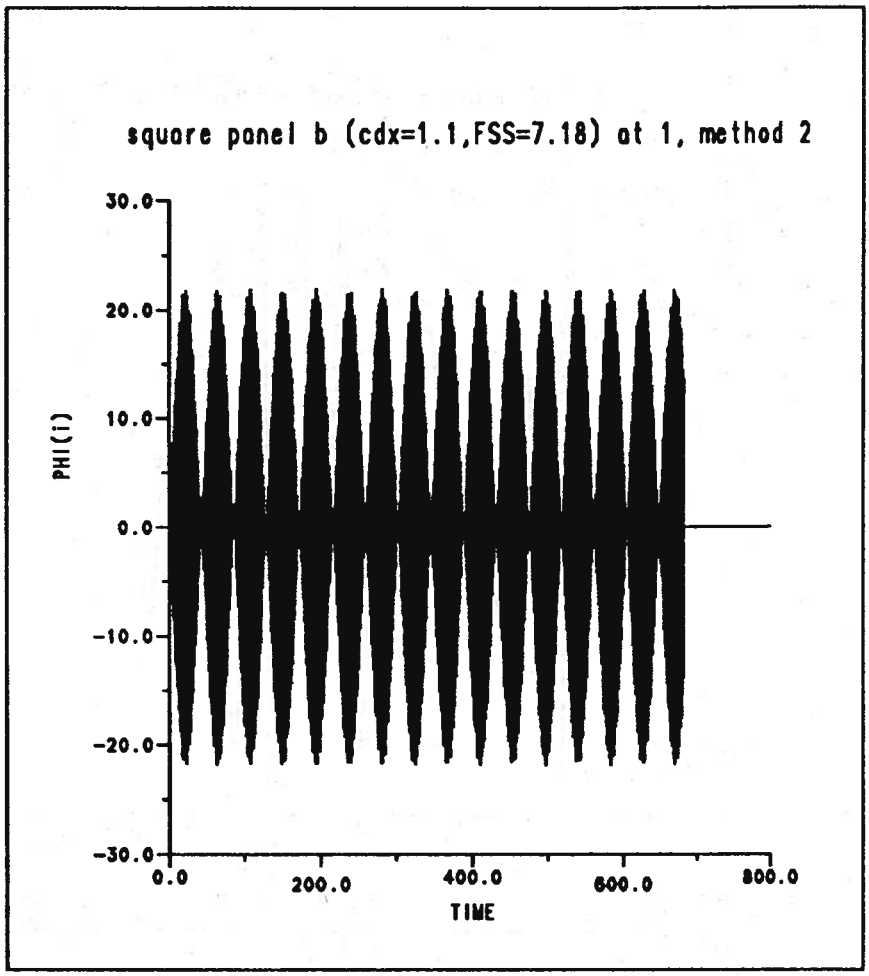

Figure 3.14: Time simulation of the square panel. Boundary conditions given as $(\phi_1, \phi_{n2}, \phi_3, \phi_4)$ with implicit-like Euler scheme for time marching. $ka = 1.1$, FSS number $= 7.180$.

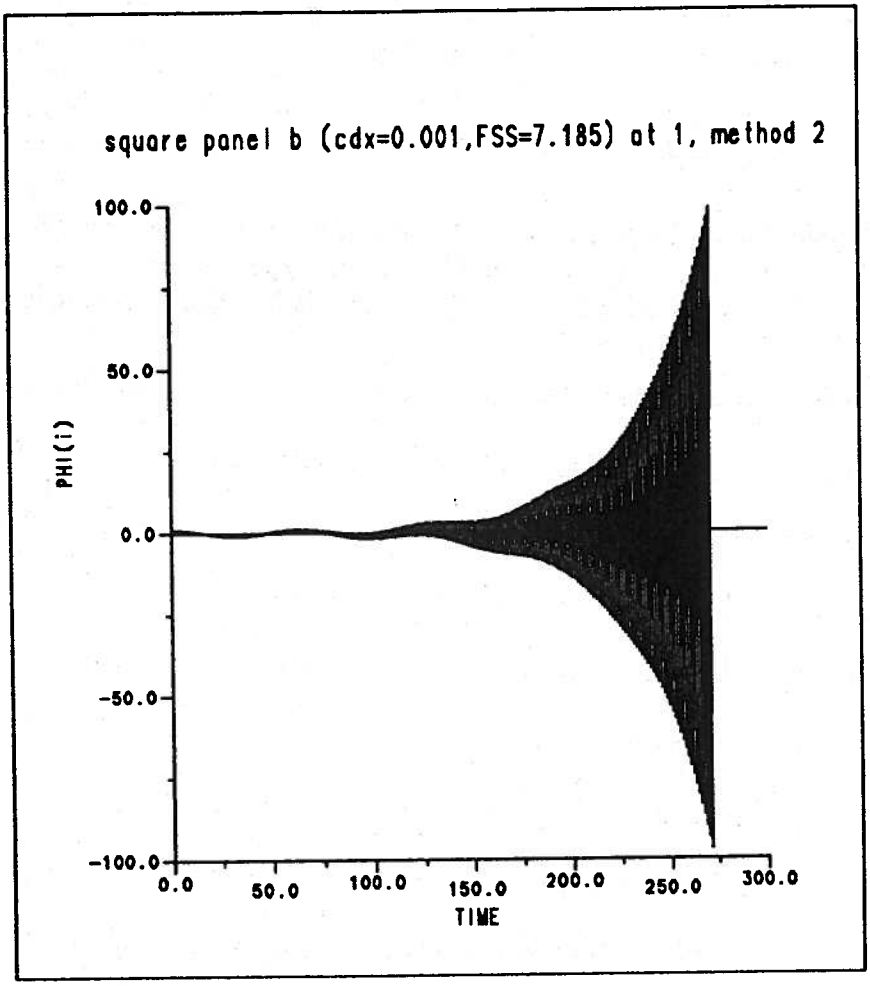

Figure 3.15: Time simulation of the square panel. Boundary conditions given as $(\phi_1, \phi_{n2}, \phi_3, \phi_4)$ with implicit-like Euler scheme for time marching. $ka = 0.001$, FSS number $= 7.185$.

Case	Boundary Condition Type	Stability Limit (FSS number)
1	$\phi_1, \phi_2, \phi_3, \phi_4$	5.47
2	$\phi_1, \phi_{n2}, \phi_3, \phi_4$	7.18
3	$\phi_1, \phi_{n2}, \phi_3, \phi_{n4}$	8.14
4	$\phi_1, \phi_{n2}, \phi_{n3}, \phi_4$	10.70

Table 3.1: Stability limits of the square panel with different boundary condition types. "Boundary Condition Type" represents the known boundary values on each panel. The implicit-like Euler scheme is used for these result.

boundary conditions. The analytic stability region is also compared with the stability region of Yeung(1982), and Dommermuth and Yue(1986). Figure 3.16 has three different curves. One of them is the stability curve by Yeung(1982). He performed the numerical stability analysis for various types of numerical schemes. In his analysis, he assumed the unknown potential derivative ϕ_z on the free surface to be the product of the wave number k and the potential ϕ. By substituting $k\phi$ for ϕ_z and performing a von Neumann analysis, Yeung obtained stability regions for various numerical schemes. In Figure 3.16, the curve of $FSS = 2\pi/ka$ is Yeung's stability limit which is independent of the panel length Δx and boundary conditions. Dommermuth and Yue used fourth-order Runge-Kutta scheme for the time marching and derived the stability region to be FSS number < 8. Their stability region is independent of the boundary condition type.

Figure 3.14 and Figure 3.15 show results that are consistent with Equation (3.62) but contradictory to Yeung's curve. The test conditions of Figure 3.14 are outside the stability region according to Yeung's analysis, but the simulation result indicates that time integration is not unstable even though the accuracy is poor. On the contrary,

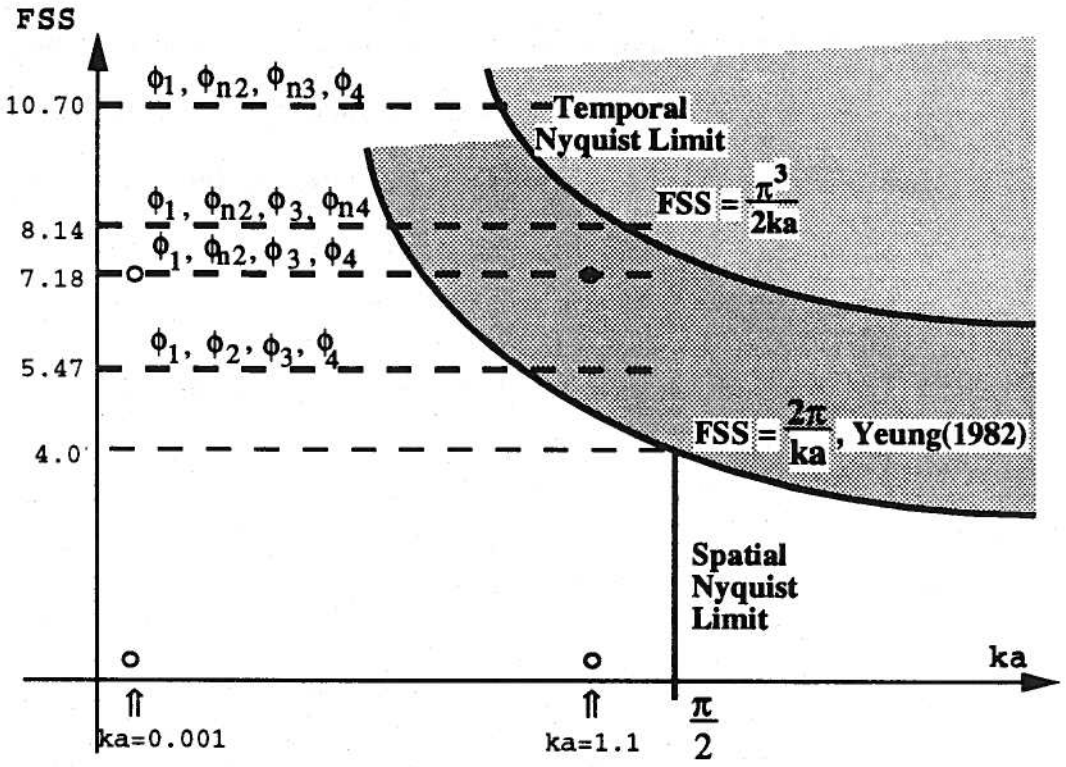

Figure 3.16: Analytic stability region of the square panel in the closed boundary problem using the implicit-like Euler scheme for time marching. 'o' represents the test condition for Figures 3.11 $\sim$ 3.14 respectively.

the test condition of Figure 3.15 is inside the stability region according to Yeung's curve, but the simulation result shows clearly that it is unstable. Figure 3.16 shows that the simulation could be stable if the test condition of Figure 3.15 is performed with different boundary conditions such as $(\phi_1, \phi_{2n}, \phi_3, \phi_{4n})$ or $(\phi_1, \phi_{2n}, \phi_{3n}, \phi_4)$.

Another curve, $ka = \pi/2$ is the spatial nyquist limit which is from the condition $k\Delta x < \pi$. The last curve, $FSS = \pi^3/2ka$ is the temporal nyquist limit which satisfies the condition $\omega\Delta t < \pi$. The nyquist conditions do not change the stability characteristics of the problem but have a strong influence on the accuracy of the calculation.

(3) Implicit Euler scheme

The difference equation for the implicit Euler scheme is

$$\phi_1^{n+2} - 2\phi_1^{n+1} + \phi_1^n = -g(\Delta t)^2 \phi_x^{n+2} \tag{3.63}$$

or substituting Equation (3.59) for ϕ_x

$$\phi_1^{n+2}\{1 + g(\Delta t)^2 C_{11}\} - 2\phi_1^{n+1} + \phi_1^n = -g(\Delta t)^2 \sum_{non\ f.s.} C_{1j}\phi_j^{n+2} \tag{3.64}$$

In a manner similar to that described above, the quadratic equation for the magnification factor becomes :

$$G^2\{1 + g(\Delta t)^2 C_{11}\} - 2G + 1 = 0$$

The stability region is determined by

$$\begin{cases} C_{11} > 0 \quad \text{or} \\ -4 < C_{11}\, g(\Delta t)^2 < -2 \end{cases}$$

where the implicit Euler scheme is **conditionally stable**. Results similar to those shown in Figures 3.10 $\sim$ 3.16 were found for the implicit Euler scheme.

(4) The previous three schemes were evaluated using the von Neumann stability analysis to find the stability regions. For this square panel case, an analytic matrix stability analysis can be obtained also. Following Equations (3.44) ~ (3.47) in Section 3.4.1, the stability equation is identical to those for the von Neumann analysis. Refer to Appendix C for stability results of the fourth order Runge-Kutta scheme. The explicit fourth-order Runge-Kutta scheme has approximately double the range of the FSS parameter of the implicit-like Euler scheme.

3.5.2 Polygonal Domain with N Panels on the Free Surface

Much of the problem formulation and the resulting mathematical equations are the same for the polygonal domain with N panels as for the multi-panel case of the near-field problem (Section 3.4.2). However, the [A] and [B] matrices are quite different. Instead of one panel on each side as in Section 3.5.1, N panels are located on the free surface and a number of panels may be on each side. The geometry of the domain is shown in Figure 3.8. The top of the domain is the free surface.

Recall that the solution for the potential may be expressed as:

$$\phi_i(\vec{x}) = -\sum \left\{ \phi_j \int_{\Delta x_j} \frac{\partial G_{ij}}{\partial n_j} dl_j - \frac{\partial \phi_j}{\partial n} \int_{\Delta x_j} G_{ij} dl_j \right\}$$

$$\begin{bmatrix} & & \\ & A_{ij} & \\ & & \end{bmatrix} \begin{Bmatrix} \vdots \\ \hline \frac{\partial \phi}{\partial n} \\ \vdots \end{Bmatrix} = \begin{bmatrix} & & \\ & B_{ij} & \\ & & \end{bmatrix} \begin{Bmatrix} \vdots \\ \hline \phi \\ \vdots \end{Bmatrix}$$

or

$$\left\{\begin{array}{c}\vdots\\ \hline \frac{\partial\phi}{\partial n}\\ \vdots\end{array}\right\} = \left[\begin{array}{c} \\ C_{ij} \\ \\ \end{array}\right]\left\{\begin{array}{c}\vdots\\ \hline \phi\\ \vdots\end{array}\right\}$$

where

$$\Longrightarrow \left\{\begin{array}{c}\frac{\partial\phi}{\partial n}\\ \vdots\end{array}\right\} = \left[[C^3][C^*]\right]\left\{\begin{array}{c}\vdots\\ \hline \phi\\ \vdots\end{array}\right\} = [C^3]\left\{\begin{array}{c}\frac{\partial\phi}{\partial n} \text{ or } \phi\\ \vdots\end{array}\right\} + [C^*]\left\{\begin{array}{c}\phi\\ \vdots\end{array}\right\} \quad (3.65)$$

$$= \sum_{j=f.s.}^{N} C^*_{ij}\phi_j + \sum_{j=non\ f.s.} C^3_{ij}\cdot(\phi_j \ \ or \ \ \phi_{n_j}) \quad (3.66)$$

With this solution from the BIM, the linearized combined free surface boundary conditions can be satisfied.

(1) Explicit Euler scheme

Substitute Equation (3.66) into the right-hand side of the explicit Euler scheme as shown below to find,

$$\phi_{tt} = -g\phi_z,$$

$$\phi_j^{n+2} - 2\phi_j^{n+1} + \phi_j^n = -g\phi_{zj}^n,$$

$$\phi_j^{n+2} - 2\phi_j^{n+1} + \phi_j^n = -g(\Delta t)^2\{\sum_{m=f.s.}^{N} C^*_{jm}\phi_m^n + \sum_{m=non\ f.s.} C^3_{jm}\cdot(\phi_m^n \ \ or \ \ \phi_{n_m}^n)\},$$

or finally

$$\phi_j^{n+2} - 2\phi_j^{n+1} + \phi_j^n + g(\Delta t)^2\sum_{m=f.s.}^{N} C^*_{jm}\phi_m^n = -g(\Delta t)^2\sum_{m=non\ f.s.} C^3_{jm}\cdot(\phi_m^n \ \ or \ \ \phi_{n_m}^n). \quad (3.67)$$

Following the von Neumann stability analysis, the quadratic form of the magnification factor equation is

$$G_j^2 - 2G_j + 1 + g(\Delta t)^2(\sum_{m=f.s.}^{N} C_{jm}^* e^{i(m-j)\beta}) = 0 \tag{3.68}$$

with roots

$$G_j = 1 \pm \sqrt{-g(\Delta t)^2(\sum_{m=f.s.}^{N} C_{jm}^* e^{i(m-j)\beta})} \tag{3.69}$$

where $\beta = k\Delta x$, and k is the wave number of the Fourier component of the error. The magnitude of least one of the two roots is larger than 1 ($|G| \geq 1$); therefore, no region of stability exists. The explicit Euler scheme is **unconditionally unstable** for the multi-panel closed boundary problem. Similar to the near-field and single panel closed boundary problems, the pure explicit Euler scheme, thus, does not have any stable region.

(2) Implicit-like Euler scheme

The difference equations for the multi-panel implicit-like Euler scheme are

$$\phi_j^{n+2} - 2\phi_j^{n+1} + \phi_j^n = -g\phi_{zj}^n,$$

$$\phi_j^{n+2} - 2\phi_j^{n+1} + \phi_j^n =$$

$$-g(\Delta t)^2\{\sum_{m=f.s.}^{N} C_{jm}^* \phi_m^{n+1} + \sum_{m=non\,f.s.} C_{jm}^3 \cdot (\phi_m^{n+1} \ or \ \phi_{n_m}^{n+1})\},$$

or

$$\phi_j^{n+2} - 2\phi_j^{n+1} + g(\Delta t)^2 \sum_{m=f.s.}^{N} C_{jm}^* \phi_m^{n+1} + \phi_m^n =$$

$$- g(\Delta t)^2 \sum_{m=non\,f.s.} C_{jm}^3 \cdot (\phi_m^{n+1} \ or \ \phi_{n_m}^{n+1}).$$

Based upon a von Neumann analysis, the quadratic form of the magnification factor equation is

$$G_j^2 - \{2 - g(\Delta t)^2(\sum_{m=f.s.}^{N} C_{jm}^* e^{i(m-j)\beta})\}G_j + 1 = 0$$

At the (j) panel, the magnification factor G_j is easily shown to be

$$G_j = 1 - \frac{g(\Delta t)^2}{2}\Big(\sum_{m=f.s.} C^*_{jm} e^{i(m-j)\beta}\Big) \pm \sqrt{-\frac{g(\Delta t)^2}{2}\Big(\sum_{m=f.s.}^{N} C^*_{jm} e^{i(m-j)\beta}\Big) + \frac{g^2(\Delta t)^4}{2}\Big(\sum_{m=f.s.}^{N} C^*_{jm} e^{i(m-j)\beta}\Big)^2} \quad (3.70)$$

The region for the stability can be numerically calculated. Therefore, the implicit-like Euler scheme is **conditionally stable** in the region where Equation (3.70) is satisfied. Equation (3.70) can be used to search for the stable region of each panel on the free surface. For each panel, the local maximum FSS number is calculated and the smallest FSS number among the local maximum FSS numbers is taken to be the stable limit for entire free surface. Table 3.2 shows the distribution of the maximum FSS numbers along the free surface panels. A right triangular domain was selected as an example and the boundary condition was given as the potential derivatives (ϕ_n) on the longest slanted side. On the free surface and on the vertical side, potentials were given as shown on Figure 3.18. Forty panels were located on the free surface, nine panels on the vertical side, and forty-one panels on the slanted side. Panels on the free surface are numbered from the right as 51 to the left as 90. Table 3.2 reveals that the stability limit is greater near both edges and smaller in the middle. This is consistent with the results for the multi-panel near-field open boundary problem (See Figure 3.6 of Section 3.4.2.).

Figure 3.17 is the time simulation result corresponding to the example of Table 3.2. This simulation was performed with the right triangular domain, the same boundary condition and the implicit-like Euler scheme as in Table 3.2. The FSS number was fixed at 4.685 which is a stable number for the edges and an unstable number for the middle panels. The figure shows a growth in the error of the potential on the middle and the effect propagates to the edges. Figure 3.17 is typical of figures

```
40*9*41 RIGHT TRIANGLE:(20011) BOUNDARY CONDITION
                    with Implicit-like Euler scheme
************************************************

  panel no. 51  :  FSSmax = 0.50327953521990E+01
  panel no. 52  :  FSSmax = 0.46935572888574E+01
  panel no. 53  :  FSSmax = 0.46657763639911E+01
  panel no. 54  :  FSSmax = 0.46647364292390E+01
  panel no. 55  :  FSSmax = 0.46654495985777E+01
  panel no. 56  :  FSSmax = 0.46645214740659E+01
  panel no. 57  :  FSSmax = 0.46653739332471E+01
  panel no. 58  :  FSSmax = 0.46646326873699E+01
  panel no. 59  :  FSSmax = 0.46652636309610E+01
  panel no. 60  :  FSSmax = 0.46647314596044E+01
  panel no. 61  :  FSSmax = 0.46651773814673E+01
  panel no. 62  :  FSSmax = 0.46648066659406E+01
  panel no. 63  :  FSSmax = 0.46651111359308E+01
  panel no. 64  :  FSSmax = 0.46648658877095E+01
  panel no. 65  :  FSSmax = 0.46650572343171E+01
  panel no. 66  :  FSSmax = 0.46649158698483E+01
  panel no. 67  :  FSSmax = 0.46650099898935E+01
  panel no. 68  :  FSSmax = 0.46649613650187E+01
  panel no. 69  :  FSSmax = 0.46649653730346E+01
  panel no. 70  :  FSSmax = 0.46650058975132E+01
  panel no. 71  :  FSSmax = 0.46649201553847E+01
  panel no. 72  :  FSSmax = 0.46650525951354E+01
  panel no. 73  :  FSSmax = 0.46648711199720E+01
  panel no. 74  :  FSSmax = 0.46651049612333E+01
  panel no. 75  :  FSSmax = 0.46648142506205E+01
  panel no. 76  :  FSSmax = 0.46651677654242E+01
  panel no. 77  :  FSSmax = 0.46647435023243E+01
  panel no. 78  :  FSSmax = 0.46652480804577E+01
  panel no. 79  :  FSSmax = 0.46646470102447E+01
  panel no. 80  :  FSSmax = 0.46653522313344E+01
  panel no. 81  :  FSSmax = 0.46644836160268E+01
  panel no. 82  :  FSSmax = 0.46654442871698E+01
  panel no. 83  :  FSSmax = 0.46641023690973E+01
  panel no. 84  :  FSSmax = 0.46656975490966E+01
  panel no. 85  :  FSSmax = 0.46661354209918E+01
  panel no. 86  :  FSSmax = 0.46850759928442E+01
  panel no. 87  :  FSSmax = 0.47774251888542E+01
  panel no. 88  :  FSSmax = 0.52561249903248E+01
  panel no. 89  :  FSSmax = 0.72196326036770E+01
  panel no. 90  :  FSSmax = 0.19254511994784E+02
```

Table 3.2: Maximum FSS number along the free surface on the triangular domain. Boundary conditions given as ϕ on the free surface, ϕ on the vertical boundary, and ϕ_n on the slanted boundary. Implicit-like Euler scheme, c=1.0.

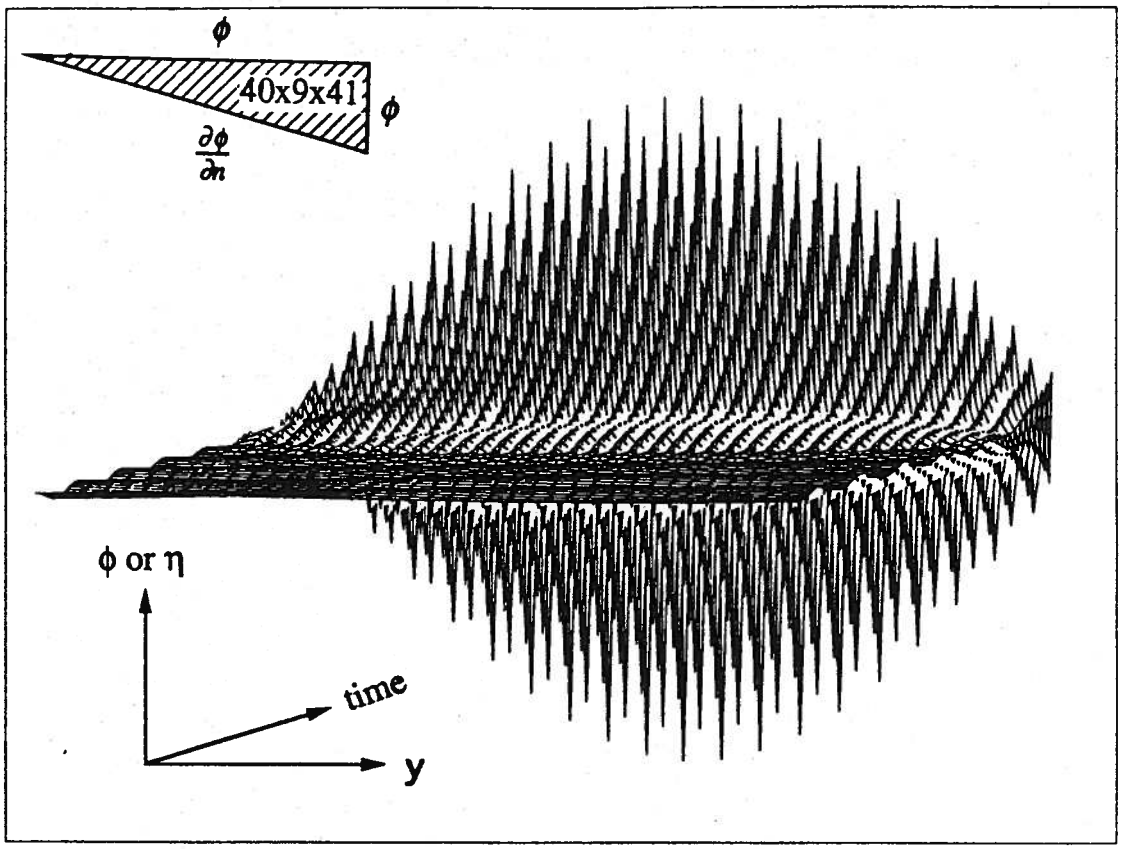

Figure 3.17: Free surface simulation for the triangular domain. Boundary conditions given as ϕ on the free surface, ϕ on the vertical boundary, and ϕ_n on the slanted boundary. Implicit-like Euler scheme. FSS number=4.685. c = 1.0.

which are on the verge of instability.

(3) Euler scheme with matrix stability analysis

The equation for the matrix stability analysis is shown in Section 3.3.2. The eigenvalues of the $[D_{ij}]$ matrix are calculated to see whether any one of the moduli of the eigenvalues is larger than 1. It is unstable if $[D_{ij}]$ has an eigenvalue whose magnitude is larger than 1.

(4) Fourth-order Runge-Kutta case using matrix analysis

With N panels on the free surface, the time simulation of the free surface problem

FSS	Eigenvalue	
	20 * 10 rec.	40 * 9 * 41
1.0	1.0 (r)	1.0 (r)
2.0	1.0 (r)	1.0 (r)
3.0	1.0 (r)	1.0 (r)
4.0	1.0 (r)	1.0 (r)
5.0	1.0* (r)	1.0 (r)
5.028	1.002 (r)	1.026 (r)
5.03	1.004 (r)	1.029 (r)
5.04	1.017 (r)	1.042 (r)
5.10	1.098* (r)	1.118 (r)
5.12	1.12 (r)	1.144 (r)
5.2	1.22 (r)	1.243 (r)
5.4	1.46 (r)	1.488 (r)
6.0	2.22 (r)	2.25 (r)

Table 3.3: Magnitude of maximum eigenvalues associated with rectangular and triangular shaped domains, which have 20 panels and 40 panels on the free surface respectively. Implicit-like fourth-order Runge-Kutta scheme. '*' represents the conditions of Figure 3.19 and Figure 3.20. '(r)' denotes real eigenvalues. c=1.0.

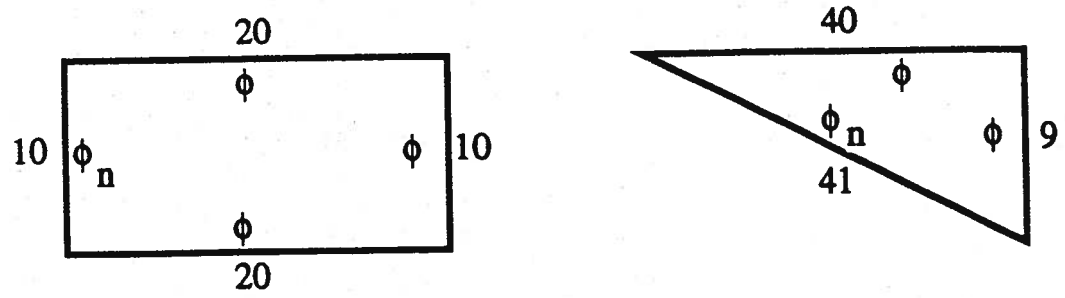

Figure 3.18: Geometry of the domain tested in Figures 3.17, 3.19 $\sim$ 3.21 and Tables 3.2 and 3.3.

is performed. The two types of polygonal domains selected for the stability analysis are depicted in Figure 3.18.

Table 3.3 shows the calculated numerical stability regions which were performed with the matrix stability analysis for the selected rectangular domain and the triangular domain. The numbers in the table represent the magnitude of the maximum eigenvalues. Also indicated are whether the maximum eigenvalues are pure real or complex. An implicit-like fourth-order Runge-Kutta scheme was used for both cases. For the rectangular domain with 20 panels on the free surface, the magnitude of the maximum eigenvalue becomes larger than 1.0 when the FSS number is over 5.028. For the triangular domain with 40 panels on the free surface, the magnitude of maximum eigenvalue also exceeds 1.0 for similar values of the FSS number.

A time simulation for the potential ϕ is done for two typical cases marked as '$*$' on the table, Figures 3.19 and 3.20 show the transition from the stable region to the unstable region. Figure 3.21 shows the distribution of eigenvalues in the complex domain for FSS number = 5.0 and FSS number = 5.1. For the case of the FSS number = 5.1, one of the eigenvalues is out of the unit circle which causes the

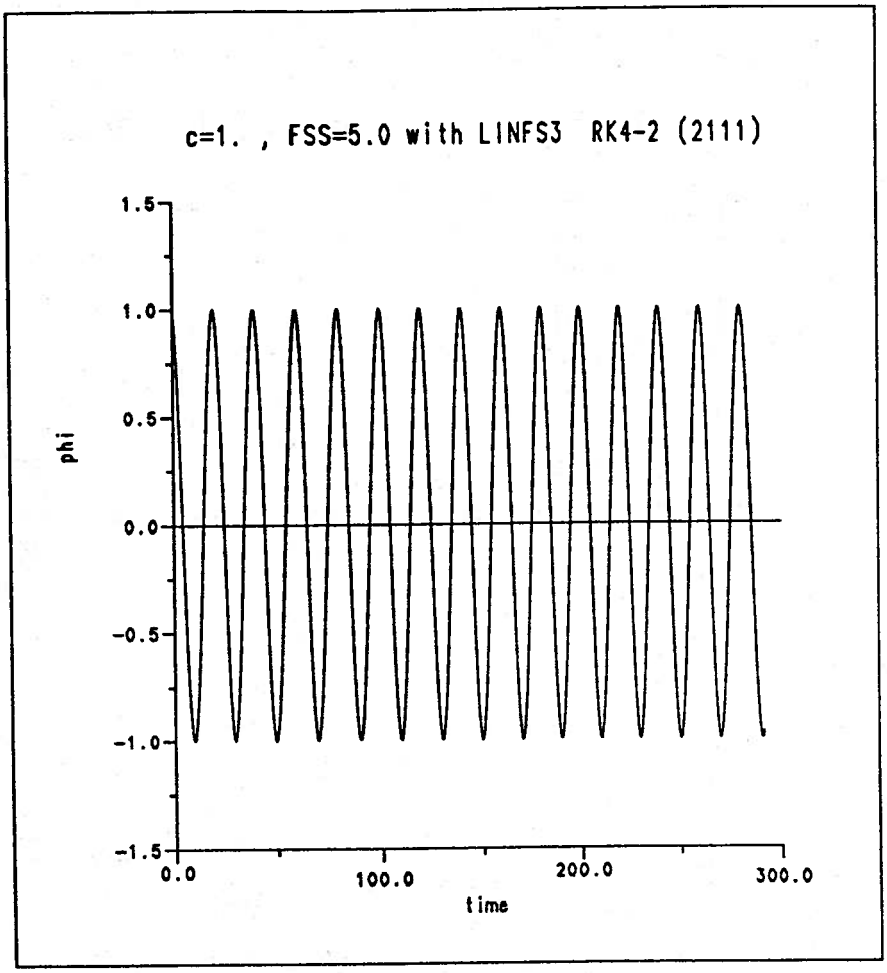

Figure 3.19: Time simulation of the potential on the first free surface panel for the multi panels case. $20 * 10$ rectangular domain. $(\phi_1, \phi_{n2}, \phi_3, \phi_4)$ type boundary condition. Implicit-like fourth-order Runge-Kutta scheme. FSS number $= 5.0$, and $\mathbf{c} = 1.0$.

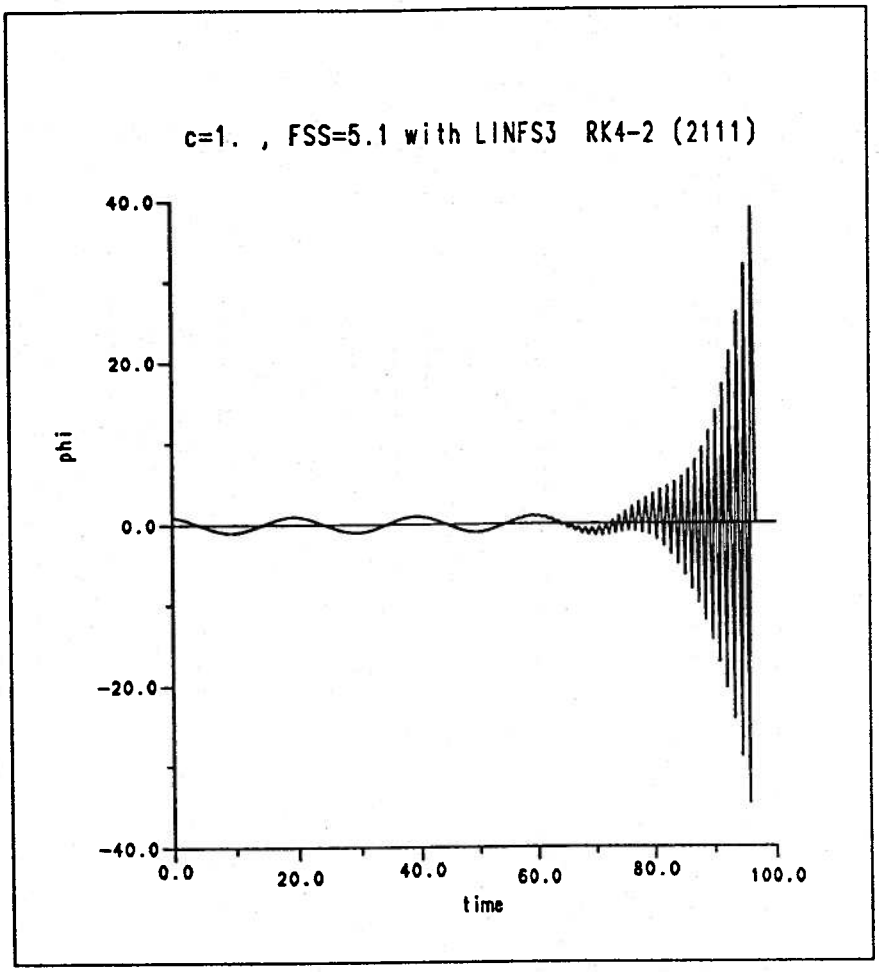

Figure 3.20: Time simulation of the potential on the first free surface panel for the multi panels case. Same as Figure 3.19 except the FSS number is increased slightly. $20 * 10$ rectangular domain. $(\phi_1, \phi_{n2}, \phi_3, \phi_4)$ type boundary condition. Implicit-like fourth-order Runge-Kutta scheme. FSS number = 5.1, and $\mathbf{c} = 1.0$.

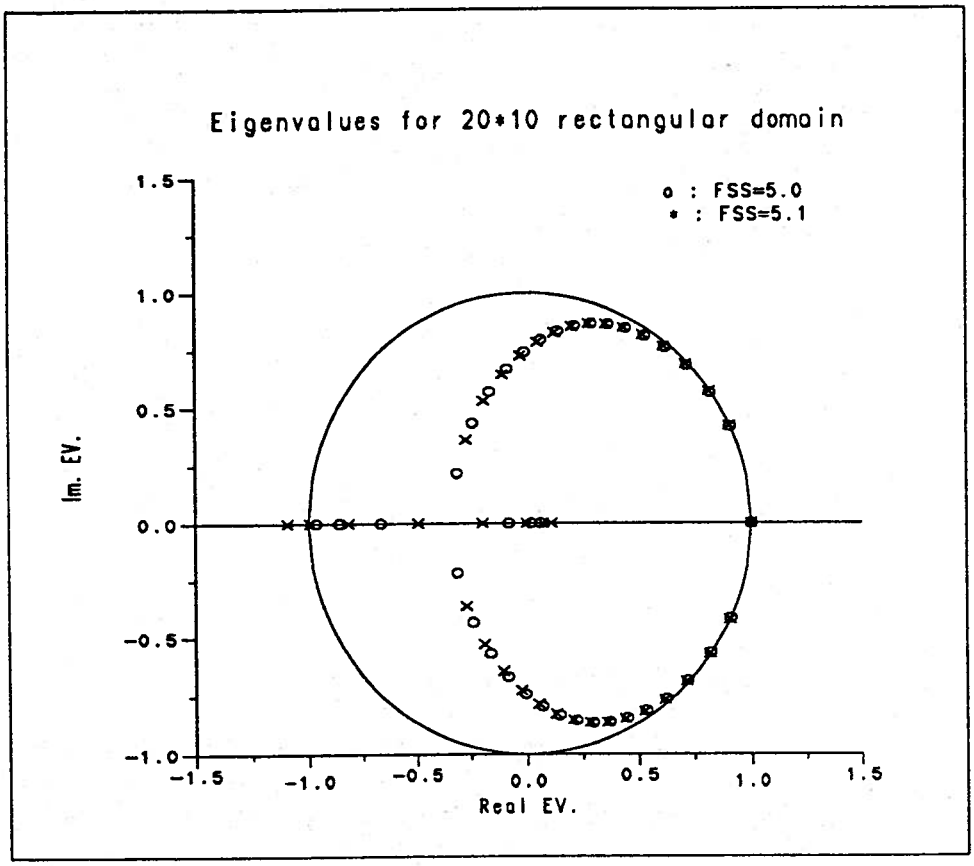

Figure 3.21: Eigenvalues of the matrix stability analysis with the unit circle for reference. Comparison of the eigenvalues between FSS numbers 5.0 and 5.1. $\mathbf{c} = 1.0$, $20 * 10$ rectangular domain. Implicit-like fourth-order Runge-Kutta scheme. $(\phi_1, \phi_{n2}, \phi_3, \phi_4)$ type boundary condition.

instability manifested in Figure 3.20.

3.6 Far-Field Open Boundary Problem

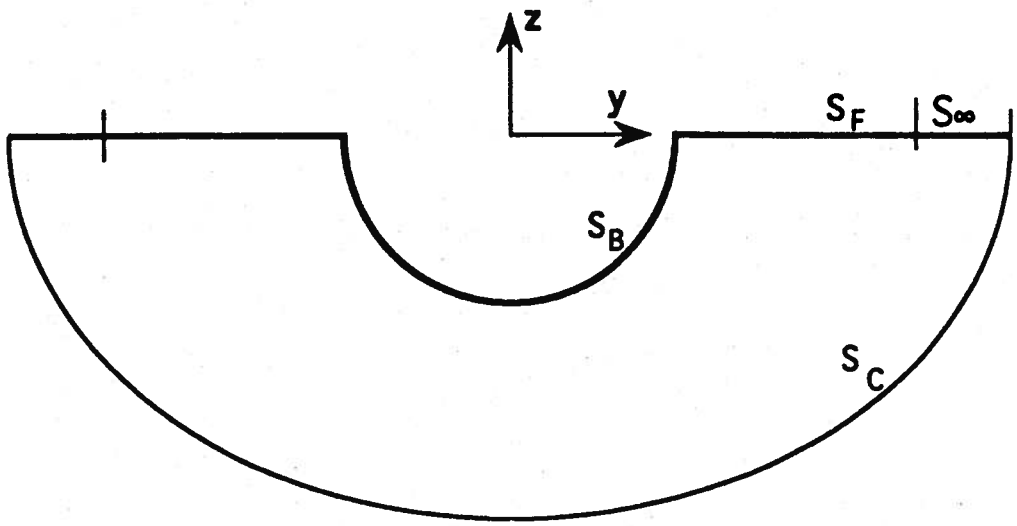

Figure 3.22: Model for the far-field open boundary problem.

Sections 3.4 and 3.5 discussed the near-field open boundary and closed boundary problems respectively. As a third example, the far-field boundary problem is introduced. This far-field open boundary problem, which has the body on the free surface and an infinitely distant far-field, is the same as the impact problem boundary. The free surface boundary conditions and the body geometry are assumed linear and the numerical stability analysis is performed for the various stability parameters.

The fluid is bounded by the free surface S_F and S_∞, by the rigid body S_B, and by the bottom and far-away contour S_c. The surface S changes to a line contour, ℓ, in the two dimensional problem (Figure 3.22). The radiation condition, which treats the infinite distance far-field boundary, is considered following Faltinsen's method for the two dimensional problem and Kang's method for the three dimensional axisymmetric problem. The effect of **c** and the truncation boundary on the numerical stability is

carefully investigated. The accuracy of the numerical scheme is checked with the continuity equation (conservation of mass).

Two methods of free surface gridding are used for the far-field open boundary problem :

1. regular spacing (constant panel length)
2. cosine spacing (Near the oscillating body, the free surface has cosine spacing; away from the body the segments are of equal length. For the nonlinear problem, this panel length is fixed during any one individual time-step.).

This investigation is essentially numerical. The complexity of the boundary value problem, including boundary conditions and time-stepping algorithms, restricts stability analysis to numerical studies. For the Far-Field, Open Boundary Problem, several different types of exciting functions on the body can be considered. These include forced oscillations starting from rest or impulsive motion with constant velocity. In this thesis, only the result for the forced oscillations starting from rest is discussed. Various numerical schemes are investigated for the matrix stability analysis. The time simulation of the wave surface evolution or the potential value on the free surface is performed to verify the limits of the stability region. The numerical stability investigation and its simulation results for two-dimensional body and for three-dimensional axisymmetric body are discussed in the following sections.

3.6.1 Two-Dimensional Forced Oscillation Starting from Rest

The forced oscillation of a body piercing the free surface has been numerically investigated using the various time-stepping schemes and the results are presented here. The modified Green function was included in the formulation. The effects of the constant added to the Green function and the non-dimensional free surface

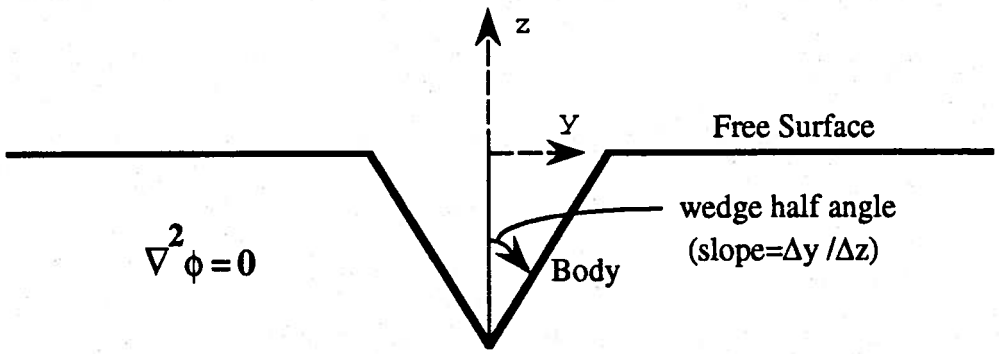

Figure 3.23: Forced oscillation for the far-field open boundary problem.

stability parameter FSS number ($= \frac{\pi g(\Delta t)^2}{\Delta x}$) on the stability region were observed.

The body on the free surface is assumed to be symmetrical. Hence, the number of the unknown values on the free surface and the body is half of the whole number of panels on the domain surface. Only the right-half of the domain is considered from now on and the number of panels represents the number on the right-half domain surface. The body geometry and the coordinate system for this section is illustrated in Figure 3.23.

When $\vec{x}$ is on the free surface, the integral equation for two dimensions is

$$\phi(\vec{x},t) = -\frac{1}{\pi}\int_{l_B+l_\infty}\left\{\phi(\vec{\xi},t)\,\frac{\vec{n}(\vec{\xi})\cdot(\vec{x}-\vec{\xi})}{|\vec{x}-\vec{\xi}|^2} + \frac{\partial\phi}{\partial n}(\vec{\xi},t)\,\ln c\,|\vec{x}-\vec{\xi}|\right\}dl$$
$$-\frac{1}{\pi}\int\!\!\!\!\!\!-_{l_f}\{\qquad\}\,dl. \tag{3.71}$$

and when $\vec{x}$ is on the body

$$\phi(\vec{x},t) = -\frac{1}{\pi}\int_{l_f+l_\infty}\left\{\phi(\vec{\xi},t)\,\frac{\vec{n}(\vec{\xi})\cdot(\vec{x}-\vec{\xi})}{|\vec{x}-\vec{\xi}|^2} + \frac{\partial\phi}{\partial n}(\vec{\xi},t)\,\ln c\,|\vec{x}-\vec{\xi}|\right\}dl$$
$$-\frac{1}{\pi}\int\!\!\!\!\!\!-_{l_B}\{\qquad\}\,dl. \tag{3.72}$$

Following Faltinsen(1977) for the two-dimensional case and Kang(1988) for three-

dimensional axisymmetric cases, the far-field truncation limits will be derived. The behavior of the potential ϕ in the far-field is considered to be the same as the value of a vertical dipole at the origin of the coordinate system. The strength of the vertical dipole is determined by matching it to the value of $\frac{\partial \phi}{\partial z}$ on the last panel at the truncation boundary.

The free surface is divided into two parts; one inside the truncation limit and the other outside the truncation limit. Hence, the integral for the potential ϕ over the free surface can be expressed in the two-dimensional case as

$$\int_{f.s.} \left\{ \frac{\partial \phi}{\partial n'} - \phi \frac{\partial}{\partial n'} \right\} G \, dl = \int_{\ell_F} \left\{ \frac{\partial \phi}{\partial n'} - \phi \frac{\partial}{\partial n'} \right\} G \, dl + \int_b^\infty \left\{ \frac{\partial \phi}{\partial z'} - \phi \frac{\partial}{\partial z'} \right\} G \, dl \quad (3.73)$$

where G is the Green function, b is the distance from the origin to the numerical truncation boundary, and ℓ_F is the actual computed free surface for $x \leq b$. The analytic approximation of the truncation boundary effect for the two-dimensional problem by Faltinsen(1977) is :

$$\int_b^\infty \left\{ \frac{\partial \phi}{\partial n'} - \phi \frac{\partial}{\partial n'} \right\} \log |\vec{x} - \vec{\xi}| dx \sim \int_b^\infty \frac{A}{x^2} \log |\vec{x} - \vec{\xi}| dx \quad (3.74)$$

where A is the strength of the vertical dipole at the origin. In a similar way, the contribution of the integration from $-\infty$ to $-b$ is calculated and summed to Equation (3.74) for the approximate truncation boundary effect.

Table 3.4 shows the numerical stability results with the changing parameters c and FSS number. This analysis was performed with 10 panels on the half wedge-type body which has 45 degree slope (*i.e.* 45 degree wedge half angle) and 20 panels on the free surface. The explicit fourth-order Runge-Kutta scheme was used for this analysis. The numbers in the table represent the maximum modulus of the eigenvalues in the matrix stability analysis, so that the condition which has the value larger than 1 is unstable and the condition which has the value less than or equal

c	0.01		0.1		1.0	
FSS	w/	w/o	w/	w/o	w/	w/o
1.0	1.0(c)	1.0(c)	1.144*(r)	0.9999*(c)	1.067(r)	1.117(r)
2.0	1.0(c)	1.0(c)	1.209(r)	0.9999(c)	1.096(r)	1.169(r)
3.0	1.0(c)	1.0(c)	1.262(r)	0.9999(c)	1.112(r)	1.211(r)
4.0	1.0(c)	1.0(c)	1.308(r)	0.9999(c)	1.138(r)	1.247(r)
5.0	1.0(c)	1.0(c)	1.350(r)	0.9999(c)	1.156(r)	1.280(r)
9.0				0.9994*(c)		
10.0				1.255*(c)		

Table 3.4: Magnitude of maximum eigenvalues associated with the forced oscillation, far-field open boundary problem. 45 degree half angle, wedge-shaped two-dimensional body on the free surface with 10 panels on the body, 20 on the free surface. Wave number k=0.3927. Explicit fourth-order Runge-Kutta scheme. '*' represents the conditions of Figure 3.19 and Figure 3.20. (r) and (c) denote real or complex eigenvalues respectively. w/ : with truncation effect, w/o : without truncation effect.

to 1 is stable. The stable region is observed by varying c from 1.0 to 0.1 to 0.01. The results suggest that the proper manipulation of c in the two-dimensional Green function controls the numerical stability for this linearized problem. The possibility of stability control for other problems with specific numerical schemes is worthy of further investigation. In Table 3.4, the cases which are selected for a time simulation and eigenvalue investigation are marked with an '*'.

The effect of the treatment of the truncation boundary on the stability was also investigated. For the two-dimensional problem, Faltinsen(1977)'s single dipole approach is followed where $\frac{\partial \phi}{\partial n}$ on the free surface outside the truncation limit is considered as the same function as a single dipole at the origin. Considering this truncation

effect, different influence coefficient matrices with correspondingly different stability regions are calculated.

Eigenvalue and simulation results shown in Figures 3.24 though 3.29 reflect the differences in the various cases. As can be seen in Table 3.4 and Figure 3.24 and Figure 3.25, the maximum eigenvalue of 1.144 is pure real and while the maximum eigenvalue of 1.255 is composed of a real and imaginary part. Figure 3.25 implies a diverging error with fluctuation while Figure 3.24 implies an exponentially diverging error. In Figure 3.26, the truncation effect was included following Faltinsen's concept and Figures 3.27, 3.28, and 3.29 are the results which do not include Faltinsen's truncation effect. Figure 3.26 and Figure 3.27 are similar to the types of instability shown in the Introduction. The case of Figure 3.26 has the maximum modulus of eigenvalue 1.144, but it is pure real and the case of Figure 3.27 has a maximum modules of 1.255, but it is complex. It follows that the behavior of the instability can be predicted by the complex number of largest eigenvalue. Dommermuth and Yue(1986) and Dommermuth et al.(1988) mentioned that the so-called Courant condition, $(\Delta t)^2 \leq \frac{8}{\pi}\frac{\Delta x}{g}$, (or $FSS \leq 8$) should be satisfied for the stability of the free surface problem when the linearized fourth-order Runge-Kutta scheme is used. This stability condition by Dommermuth and Yue clearly does not apply for the results shown in Table 3.5 and Figures 3.24 through 3.29. The reason is that their stability analysis was based simply on the Courant condition and on the assumption that $\phi_z = k\phi$.

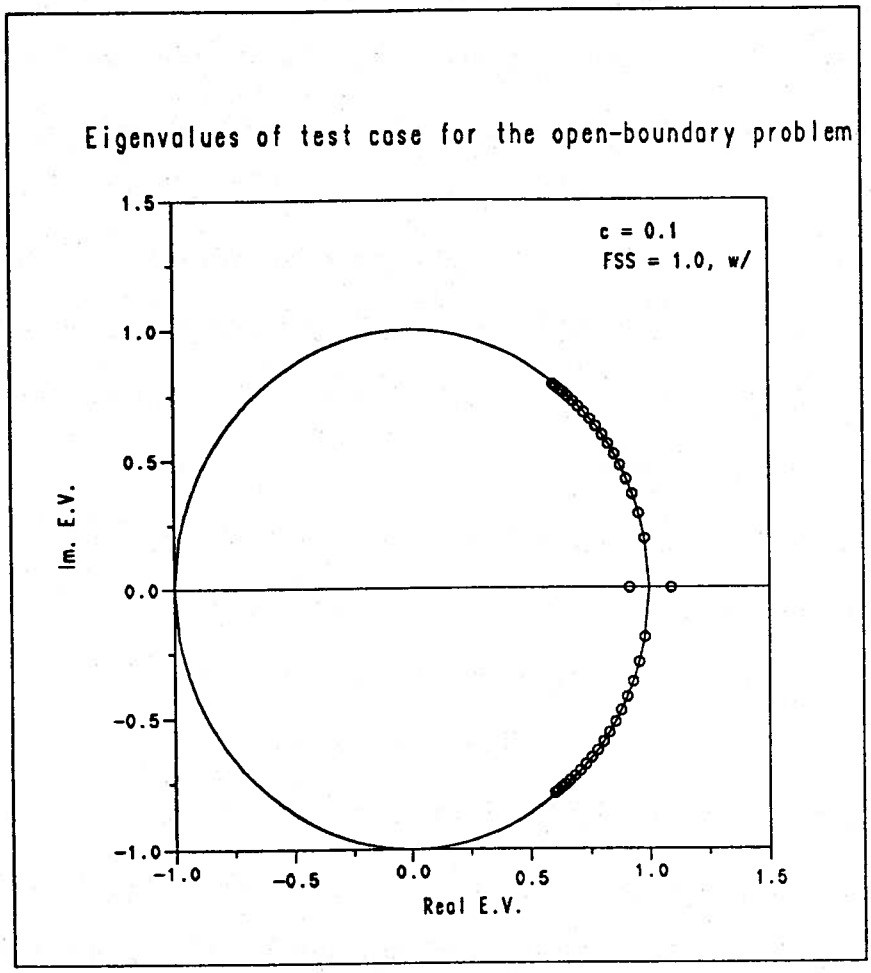

Figure 3.24: Eigenvalues of the forced oscillation, far-field open boundary problem. 45 degree half angle, wedge-shaped two-dimensional body on the free surface with 10 panels on the body, 20 on the free surface. Explicit fourth-order Runge-Kutta scheme. $\mathbf{c} = 0.1$, 'o' represents the eigenvalues for FSS number $= 1.0$ with the truncation effect.

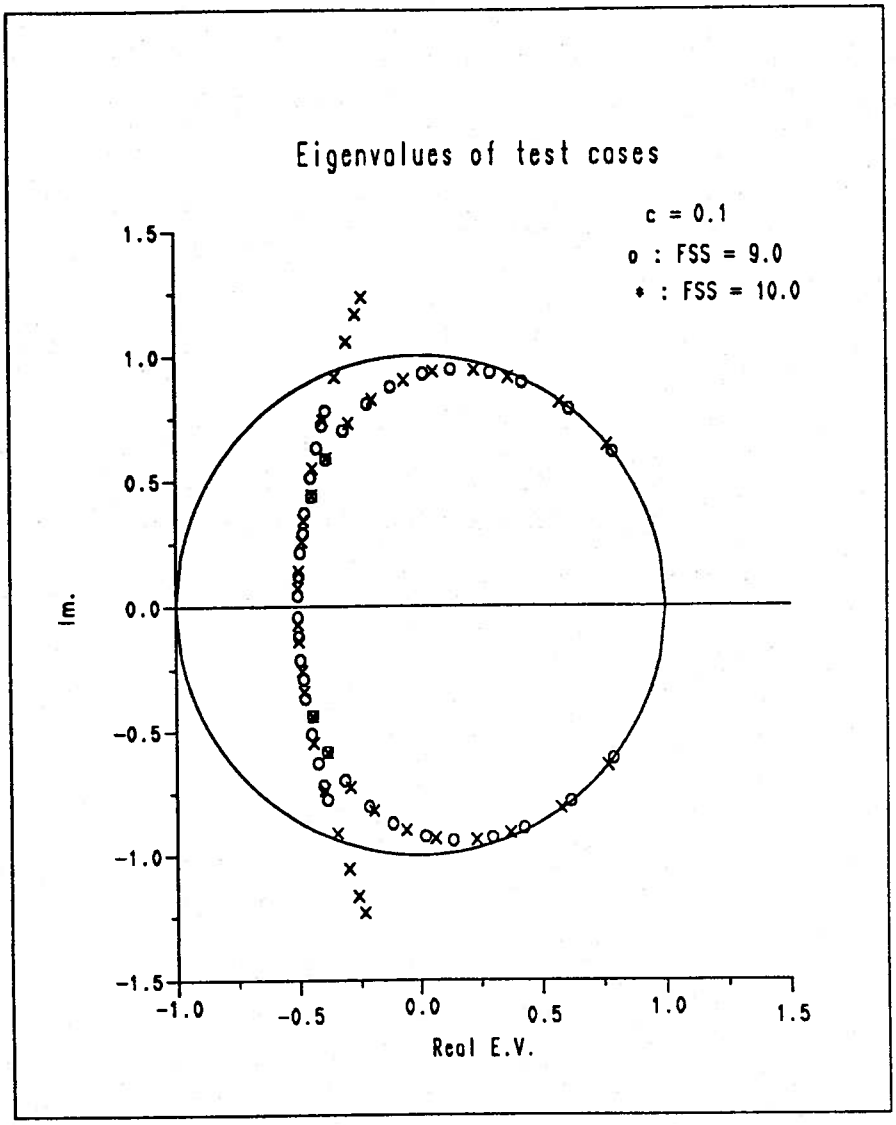

Figure 3.25: Eigenvalues of the forced oscillation, far-field open boundary problem. 45 degree half angle, wedge-shaped two-dimensional body on the free surface with 10 panels on the body, 20 on the free surface. Explicit fourth-order Runge-Kutta scheme. c = 0.1, 'o' represents the eigenvalues for FSS number = 9.0 and '×' for FSS number = 10.0 without the truncation effect.

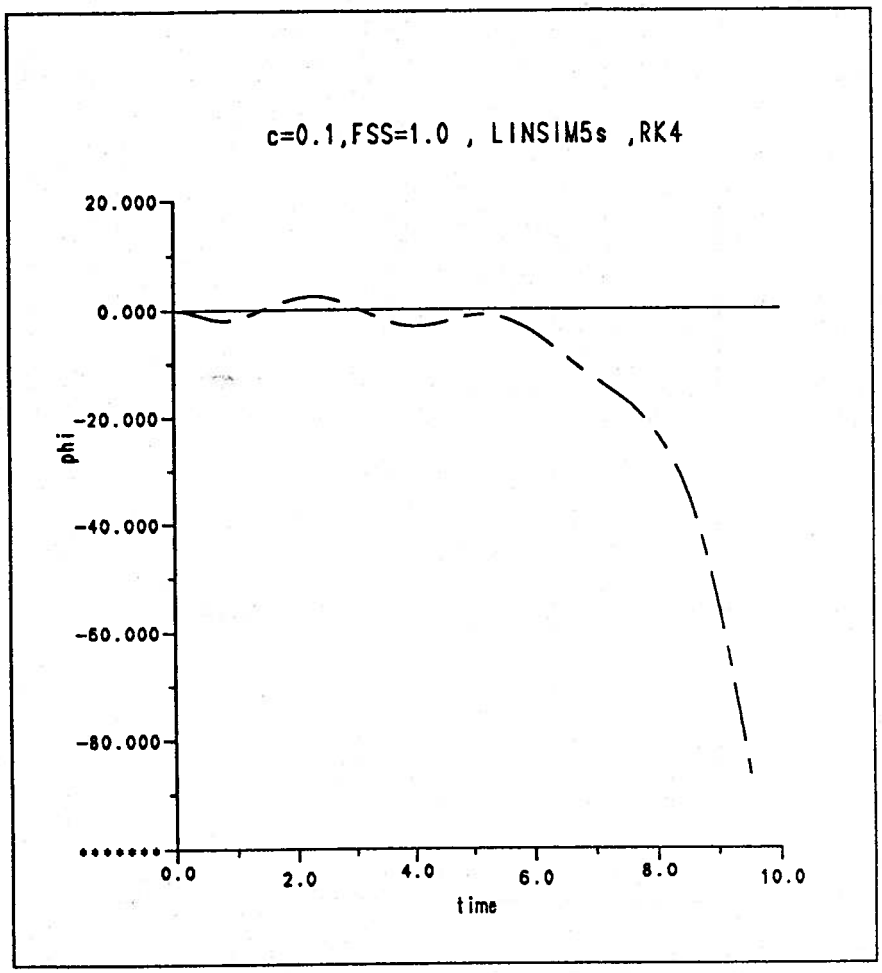

Figure 3.26: Time simulation for the forced oscillation, far-field open boundary problem. 45 degree half angle, wedge-shaped two-dimensional body on the free surface with 10 panels on the body, 20 on the free surface. Explicit fourth-order Runge-Kutta scheme. $\mathbf{c} = 0.1$, FSS number $= 1.0$ with the truncation effect.

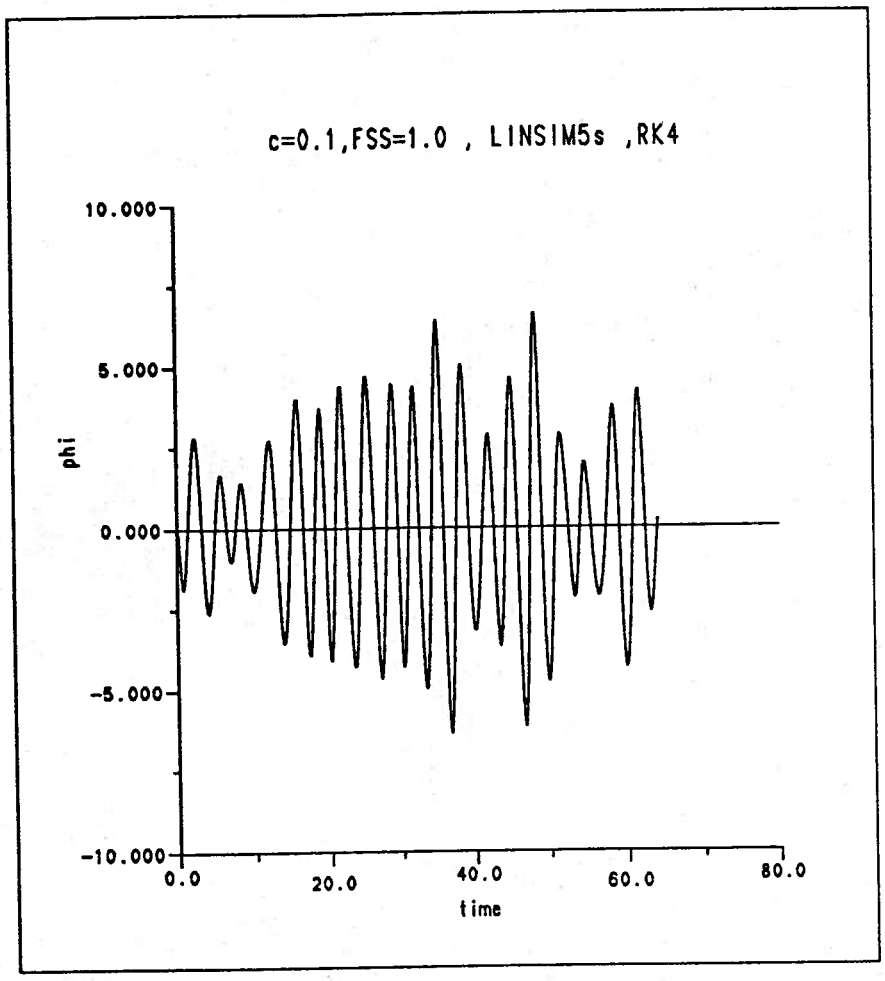

Figure 3.27: Time simulation for the forced oscillation, far-field open boundary problem. 45 degree half angle, wedge-shaped two-dimensional body on the free surface with 10 panels on the body, 20 on the free surface. Explicit fourth-order Runge-Kutta scheme. $\mathbf{c} = 0.1$, FSS number $= 1.0$ without the truncation effect.

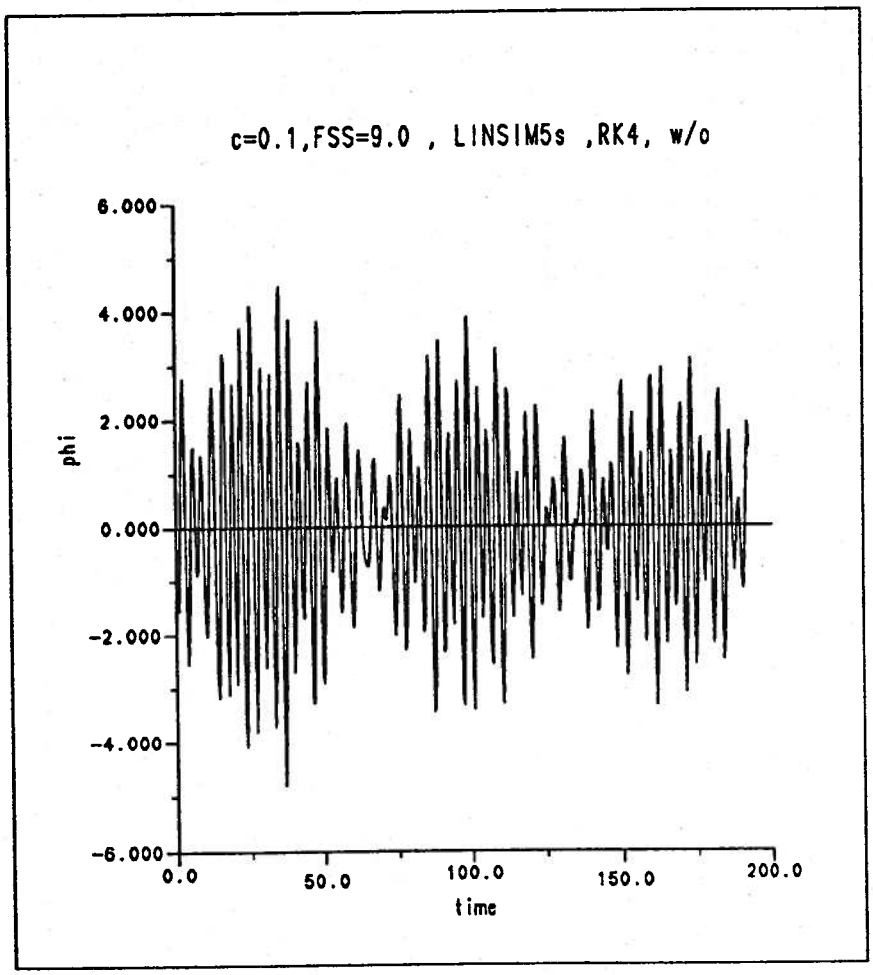

Figure 3.28: Time simulation for the forced oscillation, far-field open boundary problem. 45 degree half angle, wedge-shaped two-dimensional body on the free surface with 10 panels on the body, 20 on the free surface. Explicit fourth-order Runge-Kutta scheme. $\mathbf{c} = 0.1$, FSS number $= 9.0$ without the truncation effect.

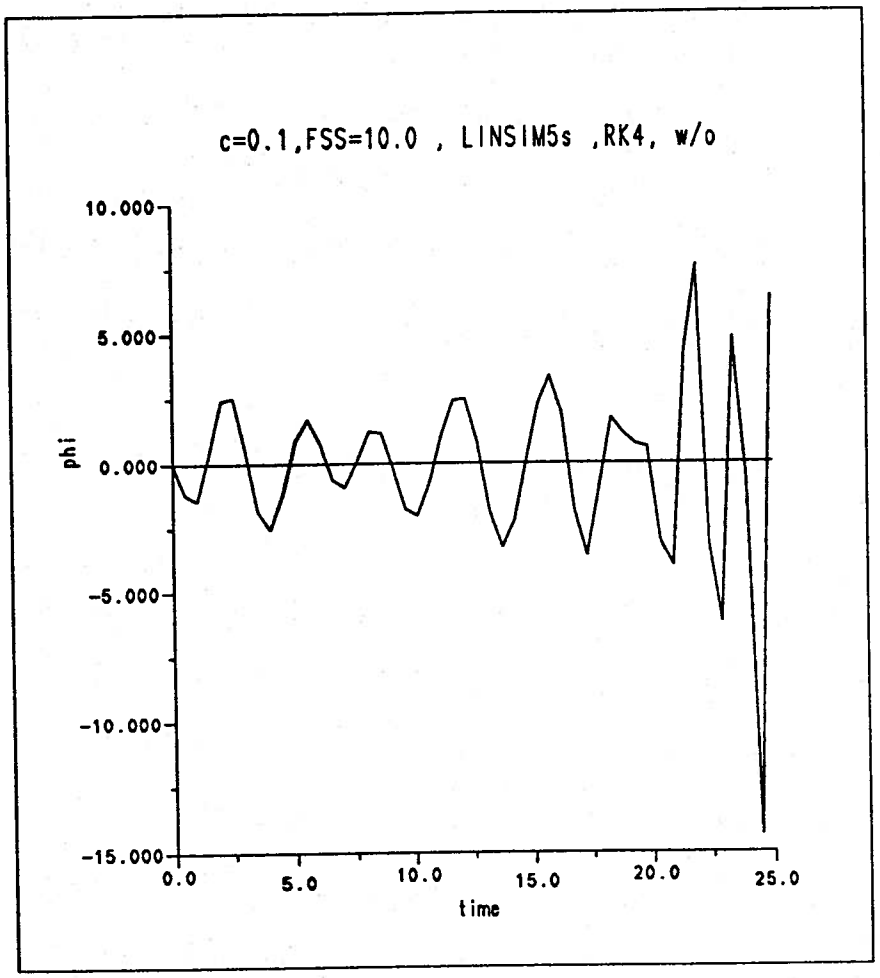

Figure 3.29: Time simulation for the forced oscillation, far-field open boundary problem. 45 degree half angle wedge-shaped two-dimensional body on the free surface with 10 panels on the body, 20 on the free surface. Explicit fourth-order Runge-Kutta scheme. $\mathbf{c} = 0.1$, FSS number $= 10.0$ without the truncation effect.

3.6.2 Axisymmetric Forced Oscillation Starting from Rest

In this section, a three-dimensional axisymmetric body is forced to oscillate on the free surface. As in Section 3.6.1, only the half-body and half of the whole domain surface is used by symmetry. The slope of the inverted cone has a 45 degree angle (*i.e.* 45 degrees half angle). The three dimensional modified Green function is used to formulate the integral equation of the BIM.

As a far-field closure, the truncation effect is considered by the method of Kang(1988). The integral for the potential ϕ over the free surface in the three-dimensional case is :

$$\int_{f.s.} r' \left[\frac{\partial \phi}{\partial n'} - \phi \frac{\partial}{\partial n'}\right] G^a \, ds = \int_{S_F} r' \left[\frac{\partial \phi}{\partial n'} - \phi \frac{\partial}{\partial n'}\right] G^a \, ds + \int_{r_o}^{\infty} r' \left[\frac{\partial \phi}{\partial z'} - \phi \frac{\partial}{\partial z'}\right] G^a \, ds \tag{3.75}$$

where G^a is the three-dimensional Green function which, through the advantage of axisymmetry, is integrated analytically in θ direction, r_o is the radius of the numerical truncation boundary and S_F is the actual computed free surface for $r \leq r_o$.

The truncated far-field effect can be integrated approximately with the distribution of potential from single dipole method. The potential on the free surface outside the truncation limit can be expanded by the Taylor series as :

$$\phi(z = \eta) = \phi(z = 0) + \eta \frac{\partial \phi}{\partial z}(z = 0) + \cdots \tag{3.76}$$

$$\begin{aligned} &\phi(z = 0) = 0 \\ &\frac{\partial \phi}{\partial z}(z = 0) \sim \frac{1}{r^3} \\ &\eta = \int_0^t \frac{\partial \phi}{\partial z}(z = 0) dt \sim \int_0^t \frac{1}{r^3} dt. \end{aligned} \tag{3.77}$$

So, to the first order, $\phi(z = \eta)$ becomes approximately

$$\phi(z = \eta) \sim \eta \frac{\partial \phi}{\partial z}(z = 0) \sim \int_0^t \frac{1}{r^3} dt \frac{1}{r^3} \sim \frac{1}{r^6} \tag{3.78}$$

Substituting Equation (3.78) into Equation (3.75) and comparing the order of magnitude with the assumption of large r_o, the following analytic approximation for the truncation boundary effect at the boundary point $\vec{x}$ is derived. For a detailed derivation of G^a, refer to Section 4.1 :

$$\begin{aligned}
&\int_{r_o}^{\infty} r' \left[\frac{\partial \phi}{\partial z'} - \phi \frac{\partial}{\partial z'}\right] G^a \, dr' \\
&\quad \cong -\frac{r_o^3}{2\pi}\frac{\partial \phi}{\partial z}(r_o) \int_0^{2\pi} d\theta \int_{r_o}^{\infty} \frac{dr'}{r'^2(r'^2 - 2rr'\cos\theta + r^2 + z^2)^{1/2}} \\
&\quad = -\frac{r_o^3}{2\pi}\frac{\partial \phi}{\partial z}(r_o) \left[\left(\frac{4\rho_1 E(m)}{r_o} - 2\pi\right)/(r^2+z^2) - \frac{2r}{(r^2+z^2)^{3/2}}(I_1 - I_2)\right]
\end{aligned} \tag{3.79}$$

where

$$I_1 = \int_0^1 \log \frac{\sqrt{r^2+z^2} - r\sqrt{1-u^2}}{\sqrt{r^2+z^2} + r\sqrt{1-u^2}} du$$

$$I_2 = \int_0^1 \log \frac{(r^2+z^2) - rr_o\sqrt{1-u^2} + \sqrt{(r^2+z^2)(r_o^2 - 2rr_o\sqrt{1-u^2} + r^2 + z^2)}}{(r^2+z^2) + rr_o\sqrt{1-u^2} + \sqrt{(r^2+z^2)(r_o^2 + 2rr_o\sqrt{1-u^2} + r^2 + z^2)}} du.$$

Equation (3.79) is an analytic approximation of the truncation boundary effect for the three-dimensional axisymmetric problem. As can be seen in Equation (3.79), the truncation effect is represented as a function of the unknown value $\frac{\partial \phi}{\partial z}$ at r_o.

The various stability regions are investigated with respect to

- the Green function constant,
- the far-field closure,
- the FSS number, and
- the various numerical schemes.

Table 3.5 shows the numerical stability results for two-dimensional cases with the same conditions as the three-dimensional cases (10 panels on the half-body, 90 panels on the free surface, wave number $k = 0.1309$, amplitude $A = 1.0$, and the

c	0.01		0.02		0.1		1.0	
FSS	w/	w/o	w/	w/o	w/	w/o	w/	w/o
1.0	1.0	1.0	1.127	1.0(c)	1.041	1.086	1.027(r)	1.043
2.0	1.0	1.0	1.184	1.0(c)	1.058	1.124	1.038(r)	1.062
3.0	1.0	1.0	1.230	1.0(c)	1.072	1.154	1.046(r)	1.076
4.0	1.0	1.0	1.270	1.0(c)	1.083	1.179	1.054(r)	1.088
5.0	1.0	1.0	1.307	1.0(c)	1.093	1.203	1.060(r)	1.099
9.0				1.0(c)				
10.0				1.275(c)				

Table 3.5: Magnitude of maximum eigenvalues associated with the forced oscillation, far-field open boundary problem. 45 degree half angle, wedge-shaped two-dimensional body on the free surface with 10 panels on the body, 90 on the free surface. Wave number $k = 0.1309$. Explicit fourth-order Runge-Kutta scheme. (r) and (c) denote real or complex eigenvalues respectively. w/ : with truncation effect, w/o : without truncation effect.

same numerical scheme) to study the effect of three-dimensions. Table 3.6 shows the numerical stability results for the three-dimensional axisymmetric case. The distribution of the eigenvalues for the three-dimensional axisymmetric case of FSS number = 10.0 are plotted in Figure 3.30.

In the analysis, it is found that the far-field closure consideration is not a major factor for the stability analysis in the three-dimensional axisymmetric case. In two-dimensions, as already shown in Section 3.6.1, the stability region can be altered by the Green function constant and the stability region is very sensitive to the far-field closure condition. The sensitiveness to the far-field closure is quite reasonable in the two-dimensional case. Wave energy propagated from the body is not diminished in

1/c	10.0		1.0		0.01		0.0	
FSS	w/	w/o	w/	w/o	w/	w/o	w/	w/o
1.0	1.0	1.0	1.0	1.0	1.0	1.0	1.0	1.0
↓	↓	↓	↓	↓	↓	↓	↓	↓
9.0	1.0	1.0	1.0	1.0	1.0	1.0	1.0	1.0
9.33	1.0	1.0	1.0	1.0	1.0	1.0	1.0	1.0
10.0	1.275	1.275	1.275	1.275(c)	1.275	1.275	1.275	1.275(c)
11.0	1.755	1.755	1.755	1.755	1.755	1.755	1.755	1.755
12.0	2.307	2.307	2.307	2.307	2.307	2.307	2.307	2.307

Table 3.6: Magnitude of maximum eigenvalues associated with the forced oscillation, far-field open boundary problem. 45 degree half angle cone-shaped three-dimensional axisymmetric body on the free surface with 10 panels on the half-body, 90 on the free surface. Explicit fourth-order Runge-Kutta scheme. (c) denotes complex eigenvalues. w/ : with truncation effect, w/o : without truncation effect.

the far-field for two-dimensions and thus far-field closure is much more important than in the three-dimensional case. In Figure 3.30, critical eigenvalues (*i.e.* $|\lambda| > 1$) with or without the boundary condition are nearly the same whereas phase differences for some non-critical eigenvalues (*i.e.* $|\lambda| \leq 1$) are detected.

The effect of the Green function constant is also very weak in the three-dimensional axisymmetric case. However, a distinct stability region can be seen by the FSS number which has a boundary at FSS number = 9.334. This is compared to the necessary stability boundary for plane progressive waves mentioned by Dommermuth and Yue(1986), FSS number = 8.0.

The numerical stability criteria is highly dependent on the choice of the numerical time-stepping scheme and the choice of the field equation solver. Several runs with implicit-like fourth-order Runge-Kutta schemes and Kang's fourth-order Runge-Kutta scheme were performed and **no stable regions were found.** In the implicit-like Runge-Kutta scheme, the modulus of the maximum eigenvalues converged to 1.0 in the limit as the FSS number went to zero. Hence, for the very small numbered range of the FSS number $0.0 \sim 0.5$, an implicit-like method may also be admissible in the calculation of the impact problem for a short time calculations. Figures 3.31 and 3.32 show the distribution of eigenvalues for the three-dimensional axisymmetric body when the FSS number = 0.6 and when FSS number = 3.0 respectively. The magnitude of the maximum eigenvalues is 1.005 for FSS number = 0.6 and is 1.2 for FSS number = 3.0 (1.0002 for FSS number = 0.2, 1.002 for FSS number = 0.4). These two figures indicate how the maximum eigenvalues are changing with increasing FSS number.

The linear stability analysis discussed in this chapter has laid the foundation for understanding the nonlinear calculations. Effects on numerical stability, such as time

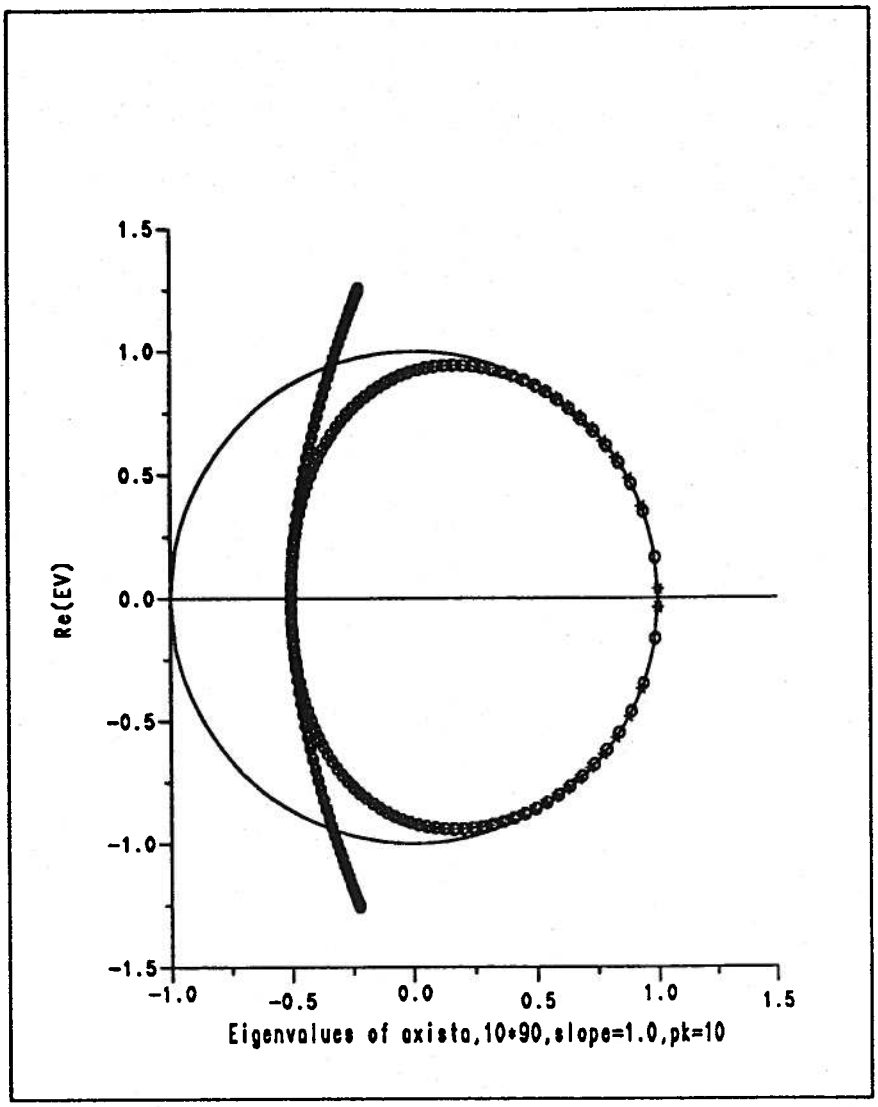

Figure 3.30: Eigenvalues of the forced oscillation, far-field open boundary problem. 45 degree half angle, cone-shaped three-dimensional axisymmetric body on the free surface with 10 panels on the half-body, 90 on the free surface. Explicit fourth-order Runge-Kutta scheme. '*' represents $1/c = 0.0$ and with the truncation effect, 'o' represents $1/c = 1.0$ and without the truncation effect. FSS number = 10.0.

differencing schemes, boundary formulations and temporal and spatial discretizations have been investigated. While these findings may have to be refined in the cases of steep, breaking waves or jets due to impact, the next chapter will demonstrate that the linear results are valid for moderately nonlinear wave calculations.

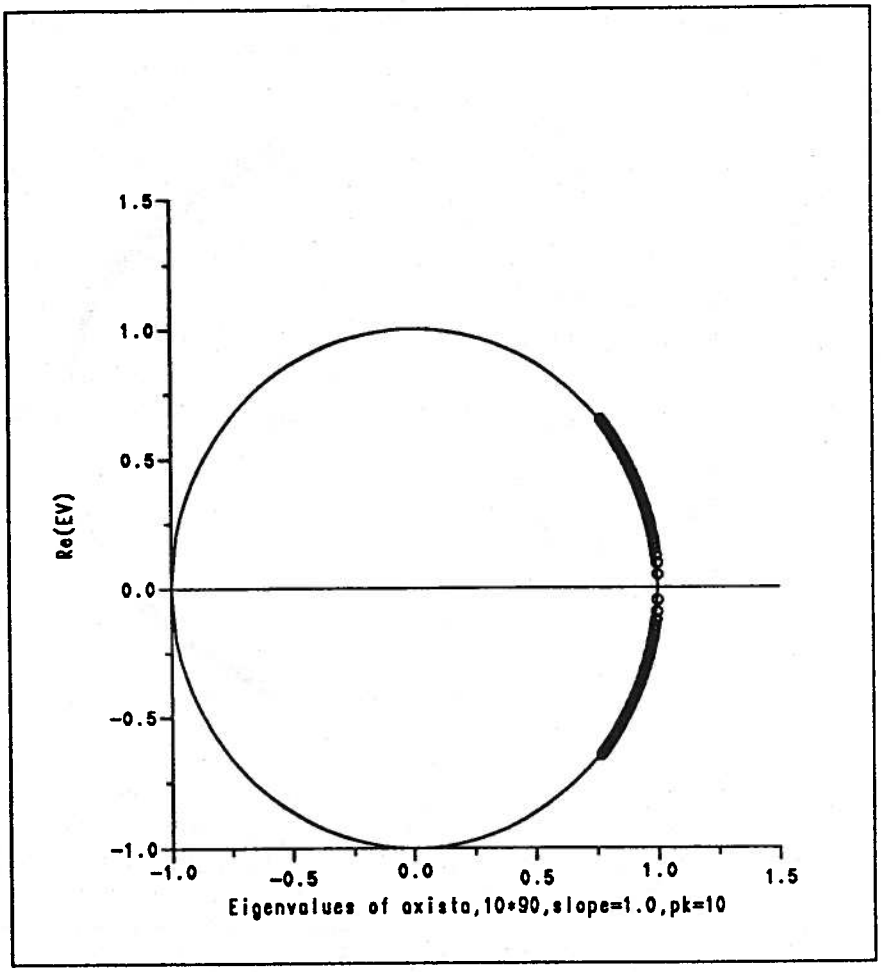

Figure 3.31: Eigenvalues of the forced oscillation, far-field open boundary problem. 45 degree half angle, cone-shaped three-dimensional axisymmetric body on the free surface with 10 panels on the half-body, 90 on the free surface. Implicit-like fourth-order Runge-Kutta scheme. c = 1.0 and FSS number = 0.6. Maximum modulus of the eigenvalue is 1.005.

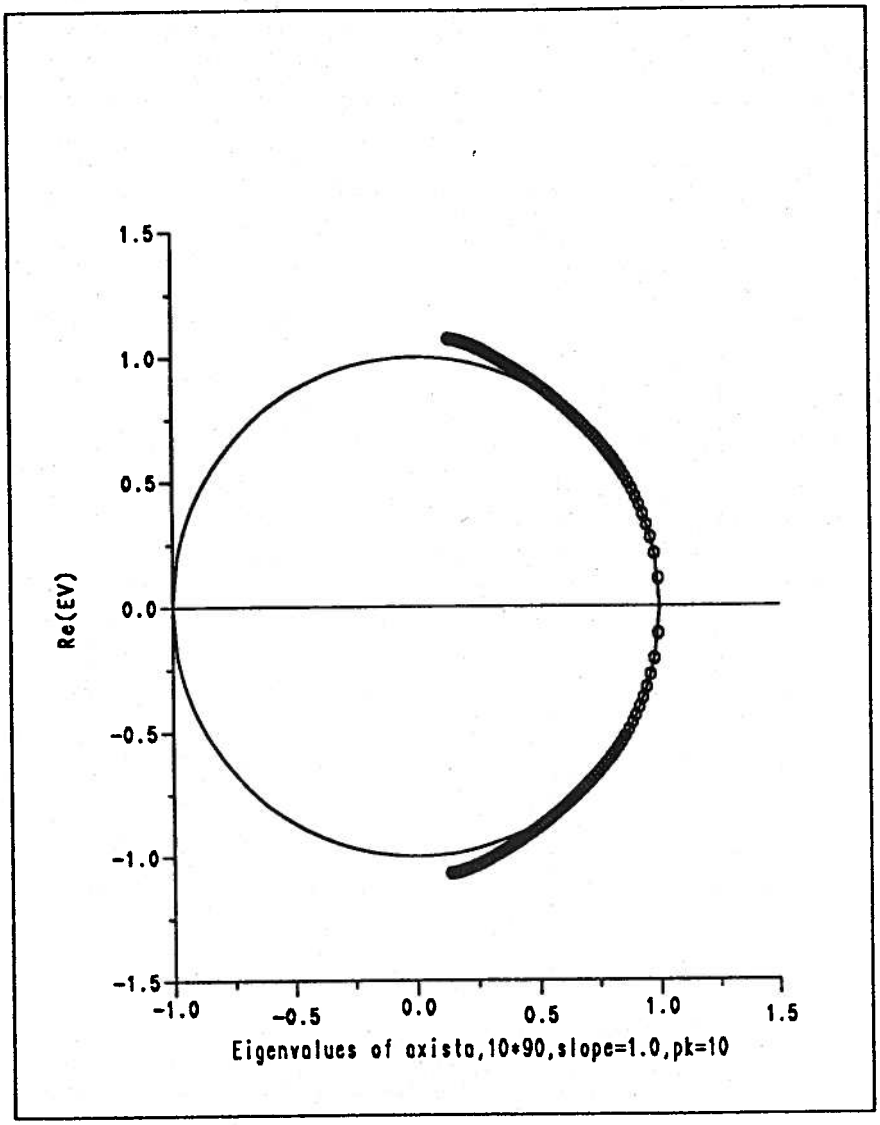

Figure 3.32: Eigenvalues of the forced oscillation, far-field open boundary problem. 45 degree half angle, cone-shaped three-dimensional axisymmetric body on the free surface with 10 panels on the half-body, 90 on the free surface. Implicit-like fourth-order Runge-Kutta scheme. c = 1.0 and FSS number = 3.0.

CHAPTER IV

NONLINEAR NUMERICAL STABILITY ANALYSIS

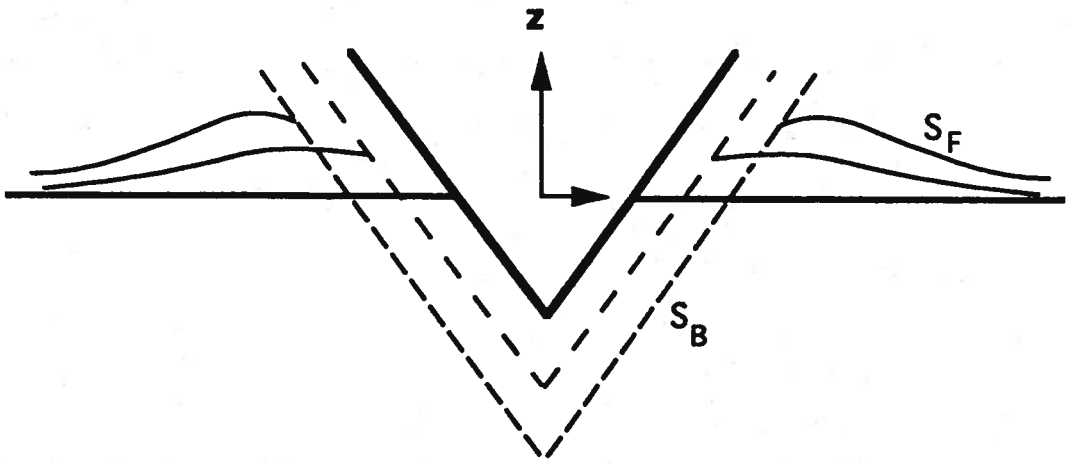

Figure 4.1: Problem domain of nonlinear analysis

In Chapter 3, the numerical stability analysis is studied with the linear free surface boundary conditions and with a linear body shape. This linear analysis is applied to several examples to see how the stability region changes with the FSS number, the Green function coefficient **c**, and the far-field condition.

With the basic knowledge of the linear numerical stability analysis firmly established, the nonlinear numerical stability analysis for the forced oscillation problem

is examined with two-dimensional and three-dimensional axisymmetric body on the free surface. The analysis is performed with nonlinear free surface boundary conditions. This analysis is applied to the impact problem of the two-dimensional and three-dimensional axisymmetric body. This nonlinear impact problem uses the same coordinate system as that of Figure 2.1, but with the body and the free surface location changing with time (See Figure 4.1).

Most of the problem solving procedures are the same as in Chapter 3 (linear analysis) except that the boundary conditions are nonlinear. The Boundary Integral Method (BIM) is used for solving Laplace's equation, and the fourth-order Runge-Kutta schemes are used for the time-stepping procedure with nonlinear free surface conditions. At each time step, the body and the free surface shape are regridded using modified Lagrangian polynomials[1]. The fourth-order Runge-Kutta schemes, however, assume that the influence coefficient matrix does not change during the intermediate steps.

4.1 Formulation

As mentioned in Section 2.1, there are one governing equation (Laplace's equation) and four boundary conditions for the impact problem. :

- Governing equation (Laplace's equation)

$$\nabla^2\phi = 0 \qquad \text{in the fluid domain,} \tag{4.1}$$

- Kinematic free surface boundary condition

$$\frac{D(z-\eta)}{Dt} = (\frac{\partial}{\partial t} + \nabla\phi \cdot \nabla)(z-\eta) = 0 \qquad \text{on } z = \eta(x,y,t), \tag{4.2}$$

[1]It's original name is the non-uniform parametric blended Lagrangian polynomials.

- Dynamic free surface boundary condition

$$\frac{p}{\rho} + \frac{\partial \phi}{\partial t} + \frac{1}{2}|\nabla\phi|^2 + gz = C(t)$$

$$\longrightarrow \quad \frac{D\phi}{Dt} = -g\eta + \frac{1}{2}\nabla\phi \cdot \nabla\phi \qquad \text{on} \quad z = \eta(x,y,t), \tag{4.3}$$

- Body boundary condition

$$\vec{V} \cdot \vec{n} = \nabla\phi \cdot \vec{n} \qquad \text{on the body, and} \tag{4.4}$$

- Far-field condition

$$\phi_n \to 0 \text{ as } |r| \to \infty. \tag{4.5}$$

Laplace's equation is solved on the boundary shape which moves at each time step. Free surface boundary conditions are applied to the free surface with the nonlinear terms included. The water depth h is assumed to be infinitely deep.

Due to the nonlinearities, a number of factors have to be considered in addition to the previously described linear numerical stability analysis:

- the body-wave intersection point, and

- the regridding algorithm.

At each time step, the matrix stability analysis is performed and compared with the results of the linear stability analysis to investigate the effect of nonlinear calculations.

With the aid of Green's second identity and Laplace's equation (Equation (2.1) and Equation (2.9)), the integral equation for the potential is derived on the free surface and the body :

$$\phi(\vec{x},t) = -\iint (\phi \frac{\partial G}{\partial n} - G\frac{\partial \phi}{\partial n})\, dS \tag{4.6}$$

Using the advantage of axisymmetric bodies, the above equation is integrated analytically in the angular direction :

$$\phi(\vec{x},t) = -\int\int_0^{2\pi} \frac{\partial G}{\partial n} r d\theta\, \phi\, dl + \int\int_0^{2\pi} G r d\theta \frac{\partial \phi}{\partial n}\, dl \tag{4.7}$$

$$= -\int \frac{\partial G^a}{\partial n'} \phi\, dl + \int G^a \frac{\partial \phi}{\partial n'}\, dl \tag{4.8}$$

where

$$G^a = \int_0^{2\pi} \frac{1}{4\pi R}\, d\theta = \frac{1}{\pi \rho_1} K(m) \tag{4.9}$$

$$\frac{\partial G^a}{\partial n'} = \int_0^{2\pi} \frac{\partial}{\partial n'}\left(\frac{1}{4\pi R}\right) d\theta$$

$$= \frac{(z-z')}{\pi \rho_1 \rho^2} E(m)\, n_{z'}$$

$$+ \frac{1}{4\pi}\left[\frac{4(r-r')}{\rho_1 \rho^2} E(m) + \frac{2}{\rho_1 r'}(E(m) - K(m))\right] n_{r'} \tag{4.10}$$

$$\rho^2 = (r-r')^2 = (z-z')^2 \tag{4.11}$$

$$\rho_1^2 = (r+r')^2 = (z-z')^2 \tag{4.12}$$

$$m = 1 - \frac{\rho^2}{\rho_1^2} \tag{4.13}$$

In Equation (4.10), $K(m)$ and $E(m)$ represent the complete elliptic integrals of the first and the second kind respectively. The source point (r', z') is defined as the position of the ring source at coordinate $\vec{X}=(r', \theta, z')$ and the field point (r, z) as the position of the control point.

As the field point $\vec{x}$ in Equation (4.6) approaches the boundary of the domain V, a principal value integral equation for the potential on the boundary is obtained. This principal value integral equation and the four boundary conditions result in a unique solution.

4.2 Far-Field Closure

As mentioned briefly in the Introduction, the far-field closure treatment is important in the body-wave interaction problem and several approaches have been proposed. One of them is the use of the periodicity characteristics of waves when there is no body on the free surface by the assumption that the waves are propagated periodically without any dispersion or dissipation. This periodicity, however, can not be applied easily to the body-wave interaction problem.

In this thesis, the potential in the far-field is considered as that of a single vertical dipole at the origin of the coordinate system. This vertical dipole is designed to have a strength so that the nonlinear inner solution matches the linear outer solution at the truncation limit. Thus, this artificial dipole strength at the origin is changed every time step according to the normal derivative of the potential at the truncation limit. This single dipole method, when used in the initial value problem, is valid until the traveling wave arrives at the truncation boundary.

The surface of the domain V is composed of body surface S_B, free surface inside the truncation limit S_F, free surface outside the truncation limit S_∞, and far-field surface S_c. Among them, the effect of far-field surface S_c can be ignored by the assumption in Equation (4.5). The effect of the free surface outside the truncation limit S_∞ for the three-dimensional axisymmetric case is derived in Section 3.6. Rewriting, the truncation boundary effect at the boundary point $\vec{x}$ is :

$$\begin{aligned}
&\int_{r_o}^{\infty} r' \left[\frac{\partial \phi}{\partial z'} - \phi \frac{\partial}{\partial z'}\right] G^a \, dr' \\
&\quad \cong -\frac{r_o^3}{2\pi}\frac{\partial \phi}{\partial z}(r_o) \int_0^{2\pi} d\theta \int_{r_o}^{\infty} \frac{dr'}{r'^2(r'^2 - 2rr'\cos\theta + r^2 + z^2)^{1/2}} \qquad (4.14) \\
&\quad = -\frac{r_o^3}{2\pi}\frac{\partial \phi}{\partial z}(r_o) \left[\left(\frac{4\rho_1 E(m)}{r_o} - 2\pi\right)/(r^2 + z^2) - \frac{2r}{(r^2 + z^2)^{3/2}}(I_1 - I_2)\right]
\end{aligned}$$

where

$$I_1 = \int_0^1 \log \frac{\sqrt{r^2+z^2} - r\sqrt{1-u^2}}{\sqrt{r^2+z^2} + r\sqrt{1-u^2}} du$$

$$I_2 = \int_0^1 \log \frac{(r^2+z^2) - rr_o\sqrt{1-u^2} + \sqrt{(r^2+z^2)(r_o^2 - 2rr_o\sqrt{1-u^2} + r^2 + z^2)}}{(r^2+z^2) + rr_o\sqrt{1-u^2} + \sqrt{(r^2+z^2)(r_o^2 + 2rr_o\sqrt{1-u^2} + r^2 + z^2)}} du.$$

Equation (4.14) is an analytic approximation of the truncation boundary effect for the three-dimensional axisymmetric problem. The effect of the truncation limit on the numerical stability region is studied with this equation.

4.3 Intersection Point

In the body-wave interaction problem, the domain boundary is composed of two major parts of the computational surface – the body surface S_B and the free surface S_F – and these two surfaces meet in one line. (This line is referred to as the 'intersection point' hereafter, since this thesis examines only the two-dimensional or three-dimensional axisymmetric problems.).

In a simplified mathematical model, the intersection point is represented as having a sharp corner which may not be in keeping with physical reality. (The effect of surface tension will certainly act to reduce 'sharp corners'.) The sharp corner induces a jump in the physical value and introduces singularities into the mathematical calculations. To eliminate these singularities from the mathematical model, the body and the free surface can be designed to meet tangentially at the intersection point. This could be achieved by requiring the first panel of the free surface to have a higher-order shape. Such a design is beyond the scope of this work and is an extension for further study.

At the intersection point, the body boundary condition, usually given as a Neumann type (derivatives of the potential), meets the free surface boundary condition,

usually a Dirichlet type (potentials). The confluence of these two boundary conditions causes a weak singularity in the integral equation. This weak singularity on the intersection point has a global influence and causes numerical difficulties for the nonlinear problem.

Kang(1989) derived the analytic calculation for the removal of the singularity by ordering the integrand in the integral equation and cancelling out the singular terms which are of the lowest order. He performed the calculations of the impact problem by assuming that the body meets the free surface with a 90 degree angle at all time. However, as the vertical velocity of the body increases or the frequency of the oscillating body becomes higher, the intersection angle between the body and the free surface can not be assumed to be at a right angle.

In this thesis, the position and the potential of the computational surface is calculated at the center of the panel in the BIM. By locating the control point at the center of the panel, the logarithmic singularity at the intersection point is removed. However, locating the control point at the center introduces the difficulty of tracing the intersection point where the continuity condition is satisfied. The kinematic continuity condition at the intersection point is, as illustrated in Figure 4.2,

$$(\phi_n)_F = (\phi_s)_B \cdot \sin(\theta_1 - \theta_2) + (\phi_n)_B \cdot \cos(\theta_1 - \theta_2) \tag{4.15}$$

$$(\phi_s)_F = (\phi_s)_B \cdot \cos(\theta_1 - \theta_2) - (\phi_n)_B \cdot \sin(\theta_1 - \theta_2) \tag{4.16}$$

where $(\phi_n)_F$: normal velocity of the water particle on the free surface,

$(\phi_s)_F$: tangential velocity of the water particle on the free surface,

$(\phi_n)_B$: normal velocity of the water particle on the body, and

$(\phi_s)_B$: tangential velocity of the water particle on the body.

The tangential velocity of the intersection point is determined by the modified

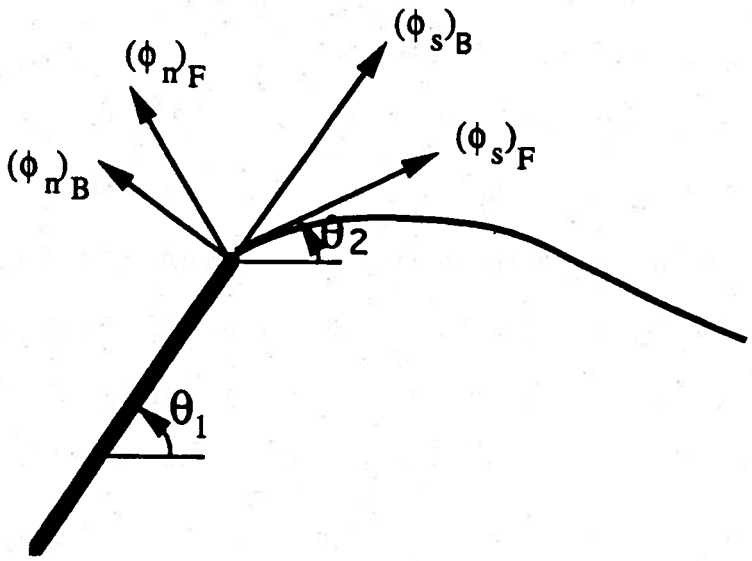

Figure 4.2: Intersection point configuration

Lagrangian polynomials interpolation scheme. The normal velocity of the intersection point is determined by the body boundary condition to be the same as the normal velocity of the body. Note that the normal velocity of the body is calculated by

$$dz = \int_{t^n}^{t^{n+1}} \dot{z} dt \tag{4.17}$$

$$\phi_n(i,n) = \frac{dz \cdot |\vec{e}_n|}{dt} \tag{4.18}$$

rather than from the time derivative of the body oscillation.

The steps in Equations (4.17) and (4.18) prevent a possible discrepancy between $\phi_z(i)\, dt \cdot |\vec{e}_z|$ and dz where $\phi_n(i,n)$ represents the normal velocity of the (i) surface panel at the (n) time step.

4.4 Regridding Algorithm

As a first step to solving the impact problem, Laplace's equation, which is the governing equation of the domain, is solved with the BIM numerical scheme. The first step determines the unknown values on each boundary; potentials of the water particles on the body and the potential derivatives of the water particle on the free surface. This information (ϕ and $\frac{\partial \phi}{\partial n}$) of the particles is used to find the evolved new locations of body and free surface, and to find the new potential values of the new free surface location using free surface boundary conditions.

As time marches, this mixed Eulerian-Lagrangian method inevitably causes the Lagrangian control points to be concentrated on the crest of the free surface wave where the gradient of the potential is large. This concentration induces the panel length to become smaller and smaller. Eventually it falls below the required length to satisfy the local Courant-Friedrichs-Lewy(CFL) stability condition. This condition is the necessity condition for a numerical stability; the time step dt should be decided so that the control point does not move out of the domain of dependence in time marching. It is practically impossible to reduce the time step dt to keep the CFL condition if the panel length becomes smaller and smaller due to the concentration of the Lagrangian markers.

To prevent the concentration of Lagrangian markers on the top of the free surface wave, a regridding algorithm is introduced in time-step iteration. This idea of using a regridding algorithm to remove the instability of the mixed Eulerian-Lagrangian scheme was suggested by Dommermuth and Yue(1988). They mentioned that the numerical scheme instability is eliminated if they keep the CFL-like condition such as, $\Delta t^2 \leq \frac{8}{\pi} \frac{\Delta x}{g}$.

In this thesis, a regridding algorithm is used to remove one possible cause of numerical instability. After solving the governing equation using the BIM, the new locations of the body and the free surface are calculated using the body and free surface boundary conditions. A new location of the body-wave intersection point is also calculated to get the wetted body length. Starting from the new body-wave intersection point, the total arc length of the free surface is calculated. The free surface is then regridded to have constant panel lengths. For the portion where the high gradient potential exists, more panels are allocated to prevent the possible loss of accuracy due to the regridding algorithm. After the regridding procedure, the new location of the control points and the potential values on the new control points of the free surface are recalculated. To investigate the numerical stability region relative to a FSS number, the time step dt is tuned to keep the FSS number constant according to the panel length dx at every time step.

4.5 Pressure Calculation

As the body starts to move from rest, the body experiences a changing hydrodynamic force imposed on it. The fluid force is estimated by the pressure integration over the wetted surface. An exact force prediction leads to reliable structural analysis for safe design of ship structures.

The equation for the pressure calculation on the body is derived from Bernoulli's equation for inviscid, incompressible, and irrotational flow.

$$\begin{aligned} \frac{p}{\rho} &= -\frac{\partial \phi}{\partial t} - \frac{1}{2}\nabla\phi \cdot \nabla\phi - gz \\ &= -\frac{d\phi}{dt} + \vec{V} \cdot \nabla\phi - \frac{1}{2}\nabla\phi \cdot \nabla\phi - gz \end{aligned} \tag{4.19}$$

where $\vec{V}$: velocity of the body

$\nabla\phi$: velocity of the particle

To get $\frac{d\phi}{dt}$ on the body, Kang's scheme is used which was extended to the three-dimensional case from the two dimensional case (Vinje and Brevig(1982)). He derived the body boundary condition for the boundary value problem of $\frac{d\phi}{dt}$ and solved $\frac{d\phi}{dt}$ using boundary value problem with the boundary conditions on the free surface and on the body.

On the body, the normal derivative of $\frac{d\phi}{dt}$ is derived using rigid dynamics and a vector identity :

$$\begin{aligned}
\frac{d}{dt}(\frac{\partial\phi}{\partial n}) &= \frac{d}{dt}(\vec{n}\cdot\nabla\phi) \\
&= \vec{n}\cdot\frac{d}{dt}\nabla\phi + \nabla\phi\cdot\frac{d\vec{n}}{dt} \\
&= \vec{n}\cdot(\frac{\partial}{\partial t}\nabla\phi + (\vec{V}\cdot\nabla)\nabla\phi) + \nabla\phi\cdot(\vec{\omega}\times\vec{n}) \qquad (4.20)\\
&= \vec{n}\cdot(\nabla\frac{\partial\phi}{\partial t} + \nabla(\vec{V}\cdot\nabla\phi) + \vec{\omega}\times\nabla\phi) + \nabla\phi\cdot(\vec{\omega}\times\vec{n}) \\
&= \vec{n}\cdot\nabla(\frac{\partial\phi}{\partial t} + \vec{V}\cdot\nabla\phi) = \vec{n}\cdot\nabla(\frac{d\phi}{dt}) \\
&= \frac{\partial}{\partial n}(\frac{d\phi}{dt})
\end{aligned}$$

where

$$\frac{\partial}{\partial n}(\frac{d\phi}{dt}) = \vec{n}\cdot(\frac{\partial V_T}{\partial t} + \dot{\vec{\omega}}\times\vec{r} - \vec{\omega}\times\vec{V}_T), \qquad (4.21)$$

V_T : translational velocity of body,

$\vec{\omega}$: rotational velocity of body, and

$\dot{\vec{\omega}}$: rotational acceleration of body.

So,

$$\frac{\partial}{\partial n}(\frac{d\phi}{dt}) = \vec{n}\cdot\frac{\partial V_T}{\partial t} = n_z a_z. \qquad (4.22)$$

Since $\vec{V}\cdot\nabla\phi$ satisfies Laplace's equation, $\frac{d\phi}{dt}$ also satisfies Laplace's equation. With Laplace's equation and the various boundary conditions, the boundary value problem is solved for $\frac{d\phi}{dt}$ on the body and $\frac{\partial}{\partial n}(\frac{d\phi}{dt})$ on the free surface. Once $\frac{d\phi}{dt}$ on

the body is obtained, the pressure on the body is calculated with Equation (4.19). Equation (4.19) is composed of three parts – the unsteady time varying pressure component, $\frac{d\phi}{dt}$, the dynamic pressure component with the nonlinear term, $\vec{V} \cdot \nabla\phi - \frac{1}{2}\nabla\phi \cdot \nabla\phi$, and the static pressure term which is proportional to depth, $-gz$. Figure 4.3 shows the dynamic pressure distribution on the body for the test case of Figure 4.5, which is the oscillating body with amplitude 0.5. The ratio of the dynamic pressure including the nonlinear term to the static pressure is approximately 1% ~ 3%.

In Figure 4.3, the origin or left side represents the tip of the cone which is the deepest point and the right side represents the intersection point to the free surface. The horizontal axis is the body surface, the y axis is time, and the vertical axis is the magnitude of pressure. The real length of the wetted body along the y axis is not constant, but the wetted body length is adjusted to be equal for plotting purposes. The magnitude on the left side of the figure is smaller than that of the right side which suggests that the water particle velocity near the surface is larger in magnitude than that farther from the surface. This effect is partly from the nonlinear term in the pressure calculation, $\nabla\phi \cdot \nabla\phi$. The undulation frequency of the dynamic pressure in time (Figure 4.3) is twice the oscillating frequency of the body. The reason for this phenomena can be found from the mathematical form for this figure, $(-\vec{V} \cdot \nabla\phi - \nabla\phi \cdot \nabla\phi)$. In Figure 4.3, the amplitude of the undulation on the left side is less than that on the right side reflecting the effects of depth of the water. Another phenomena which can be observed is a small phase difference between the bottom and the free surface. The bottom leads the phase and this phase difference is not found in the other terms of the pressure.

Figure 4.4 shows the distribution of the unsteady term, $\frac{d\phi}{dt}$. The same plotting

technique as in Figure 4.3 is used in this figure. The undulation frequency is the same as that of the body. The magnitude of the values are about eight times the values of the dynamic pressure. There is no phase difference in this figure.

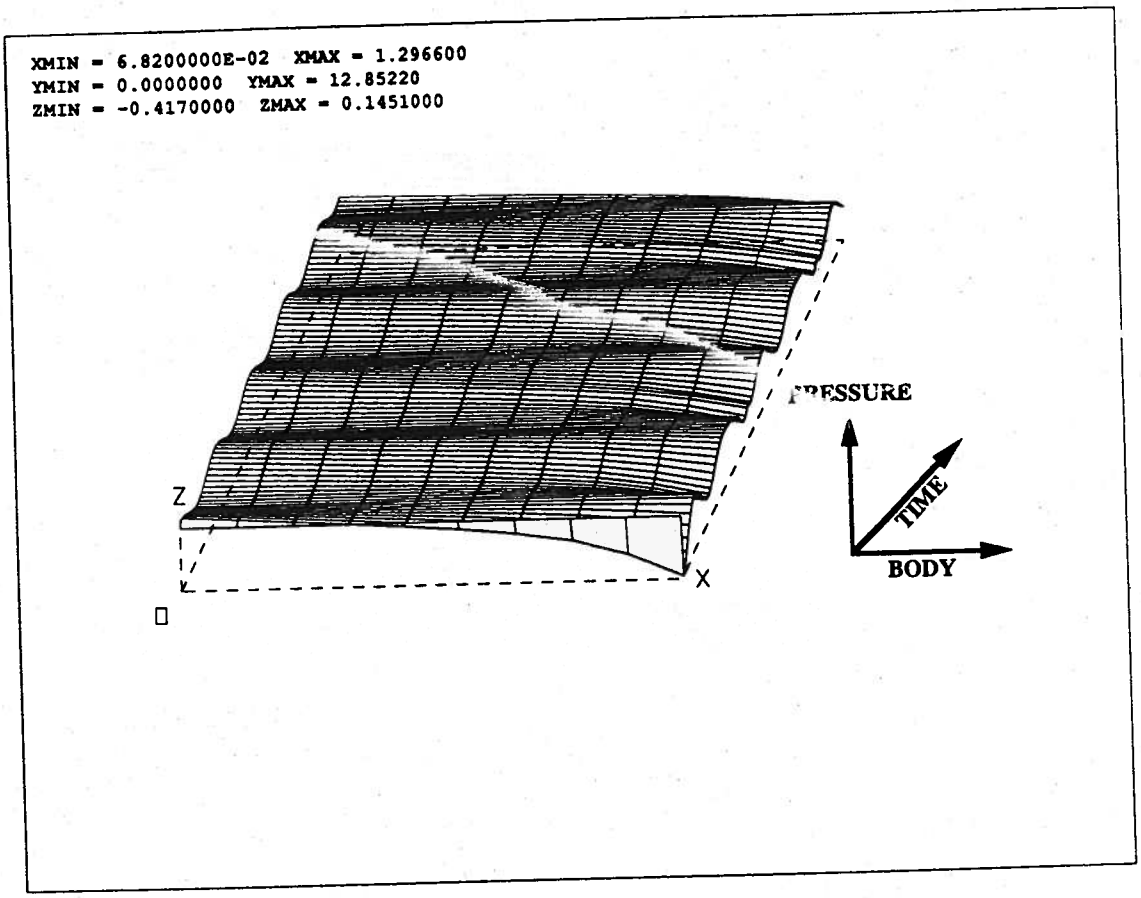

Figure 4.3: Pressure distribution on the body due to dynamic term $(-\vec{V} \cdot \nabla\phi - \nabla\phi \cdot \nabla\phi)$. Two-dimensional wedge-shaped body with 45 degrees dead-rise angle. 10 panels on the body and 90 panels on the free surface. Amplitude=0.5, $k = 0.1309$, FSS number=1.0, c = 0.02, without the truncation effect. Explicit fourth-order Runge-Kutta method.

The intersection point is the location where the total pressure is changed from positive to zero. So, the total pressure at the intersection point acts as a checking device for the jet-formation. If a part of the body becomes unwetted below the intersection point for some reason (Figure 4.11), the total pressure of that part was

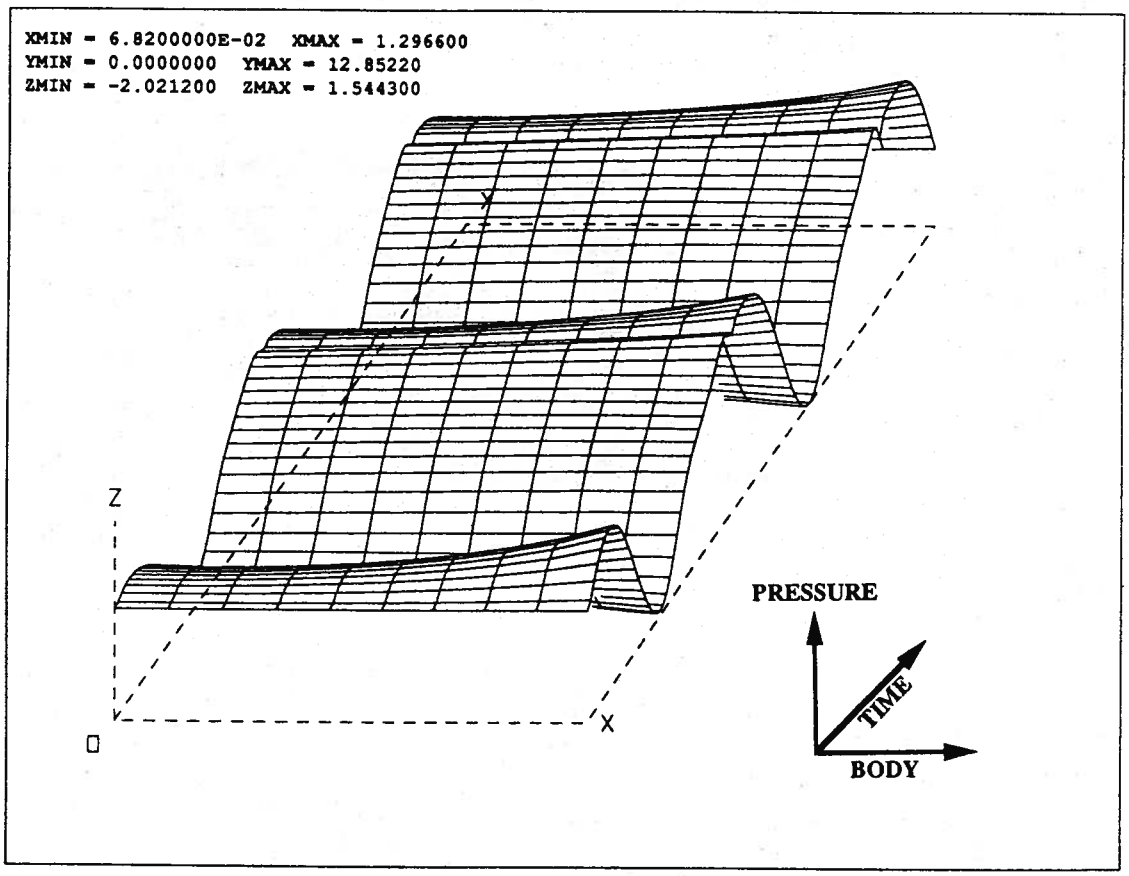

Figure 4.4: Unsteady term of the pressure distribution on the body ($\frac{d\phi}{dt}$). Two-dimensional wedge-shaped body with 45 degrees deadrise angle. 10 panels on the body and 90 panels on the free surface. Amplitude=0.5, $k = 0.1309$, FSS number=1.0, $\mathbf{c} = 0.02$, without the truncation effect. Explicit fourth-order Runge-Kutta method.

revealed to be a negative value.

4.6 Stability Results

In Chapter III, both the Euler schemes (second order) and the fourth-order Runge-Kutta schemes are used in the fundamental study of the numerical stability for various cases. In this section, only the fourth-order Runge-Kutta schemes are used for the numerical calculations and the investigation of the stability regions. The Runge-Kutta scheme has four intermediate steps between one time step calculation of the free surface η and the potential ϕ. Using the Runge-Kutta scheme for the potential on the free surface η, the influence coefficient matrix values are assumed to be fixed in the intermediate steps. However, the body and the free surface locations are updated at each intermediate step.

The numerical procedure for the nonlinear simulation of the oscillating body-wave interaction problem is shown in Figure 4.12. The body is oscillating with frequency ω on the free surface or moves down with the constant velocity into the water. The free surface evolves following the nonlinear free surface boundary conditions from an initially calm water level. At each time step, the evolved free surface is used for the calculation of the new influence coefficient matrix for the BIM. The locally linear numerical stability analysis is performed while the potential is calculated with nonlinear boundary conditions. The numerical stability analysis, therefore, reflects the nonlinear boundary condition effects in a global sense even though the analysis is locally linear.

Table 4.1 shows the two-dimensional nonlinear stability analysis. The numbers in the table represent the maximum modulus of the eigenvalues during the simulation. The maximum modulus is calculated at each time step since it is changing due to

nonlinearities.

The test conditions are initial depth of body : 1.0,
body oscillating amplitude : 0.5,
$z = -0.5 \sin \omega t$,
wave number $k = 0.1309$,
number of panels on the body : 10, and
number of panels on the free surface : 90.

The test conditions above are set to be the same as in Section 3.6.1 for comparison with the linear results. The Green function constant effect is also investigated and it acts as a control parameter. When c is 1.0, no stability regions are found for any FSS number. But when c is 0.01, this scheme becomes conditionally stable. In the nonlinear analysis, the magnitude of the maximum eigenvalues is found to vary slightly relative to the linear results. Thus the stability range in the linear analysis is almost the same as the range in the nonlinear analysis. In nonlinear calculations, the variation of the stability area is less than 1 % with respect to time. This implies that the nonlinear effect on the numerical stability analysis by the nonlinear boundary condition is not so critical. This also supports the idea that the linear stability analysis is valid for the nonlinear calculation of the mildly steep wave problem unless a jet is formed with high entrance velocity of the body into the water or low deadrise angle of the body.

These results show that the linear stability analysis is a good first estimate of the nonlinear stability properties. The computer time used for the simulation and eigenvalues calculation in one case of Table 4.1 is about 70 minutes CPU time on a 'Stella GS2000' graphics super computer.

Figure 4.5 and Figure 4.7 show typical examples of the stable and unstable sim-

c	0.01		0.1		1.0	
FSS	w/	w/o	w/	w/o	w/	w/o
1.0	1.0	1.0	1.040 ~ 1.041	1.086 ~ 1.078	1.026 ~ 1.027	1.043 ~ 1.041
2.0	1.0	1.0	1.058 ~ 1.057	1.124 ~ 1.117	1.038 ~ 1.035	1.043 ~ 1.062
3.0	1.0	1.0	1.072 ~ 1.069	1.154 ~ 1.148	1.050 ~ 1.048	1.076 ~ 1.073
4.0	1.0	1.0	1.083 ~ 1.081	1.179 ~ 1.178	1.061 ~ 1.060	1.105 ~ 1.101
5.0	1.0	1.0	1.093 ~ 1.088	1.203 ~ 1.202	1.072 ~ 1.071	1.113 ~ 1.111

Table 4.1: The maximum modulus of the eigenvalues from the nonlinear time simulation results of two-dimensional wedge-shaped body case with 45 degrees deadrise angle. 10 panels on the body and 90 on the free surface. Explicit fourth-order Runge-Kutta method. 'w/' represents 'with the truncation effect' and 'w/o' represents 'without the truncation effect'

ulations. The left edge of the figures is the location of the wedge-type body which has 45 degrees half-wedge angle. Figure 4.6 and Figure 4.8 are wider plots of Figure 4.5 and Figure 4.7, respectively. They include the behavior of the potential near the far-field truncation limit. The horizontal axis in the figures represents the wave profile as time changes and the vertical axis the time step (Figures 4.5 ~ 4.8). The panel length Δx is $\lambda/90$ ($\simeq 0.533$) and the time step size Δt is $\sqrt{\Delta x \cdot FSS/(\pi g)}$ ($\simeq 0.132$ for Figures 4.5 and 4.6, and $\simeq 0.228$ for Figures 4.7 and 4.8). For the unstable case in Figures 4.7, 4.8, and 4.10, the time step size Δt is $\sqrt{3}$ times lager than that for the stable case (Figures 4.7 and 4.6). Thus, the far-field values are soon contaminated and the error propagates quickly. Figure 4.10 is the potential distribution for the case of Figure 4.7. In the figure, the horizontal axis represents the free surface, and the vertical axis the potential values. The potential values drop exponentially as time increases. It occurs as the wave generated by the oscillation of

the body propagates to the truncation boundary. It is imagined that the unstable characteristics of the condition are manifested by the reflection of the waves at the truncation limit.

In Figure 4.9 and Figure 4.10, the horizontal axis represents the free surface from the intersection point to the far-field truncation limit. The actual length is changing at each time step due to the change of the intersection point. In these figures, though, all the free surface lengths are fixed to the initial lengths for the purposes of plotting.

Table 4.2 shows the stability analysis of the nonlinear axisymmetric case. The test condition is set to be the same as that of Section 3.6.2 for comparison. Most of the stability criteria is confirmed to be the same as the linear result when the FSS number is under 7.0. As the FSS number exceeds 7.0, the free surface in the vicinity of intersection point forms a jet-like behavior and the stability region disappears. This table again confirms that the linear stability analysis is valid for the nonlinear calculation of the moderately steep wave problem until a jet is formed.

Figure 4.11 shows a jet-formation near the intersection point for decreasing dead-rise angle. Near the intersection point, the free surface forms a parallel surface to the body separated by a very narrow distance. This creates the sharp turn on the free surface geometry near the body. The narrow distance between the body surface and the jet surface causes difficulties in the numerical calculation by the source distribution method since the influence coefficient matrix has large off-diagonal terms. For the sharp corner on the free surface near the body, the proper curve-fitting scheme should be carefully chosen. The analytic solution of the similarity solution for the jet could be a good alternative for the jet shape near the body. This jet formation near the body is observed in the nonlinear analysis which is not captured in linear simulations. Once the jet is formed, the influence coefficient near the jet becomes

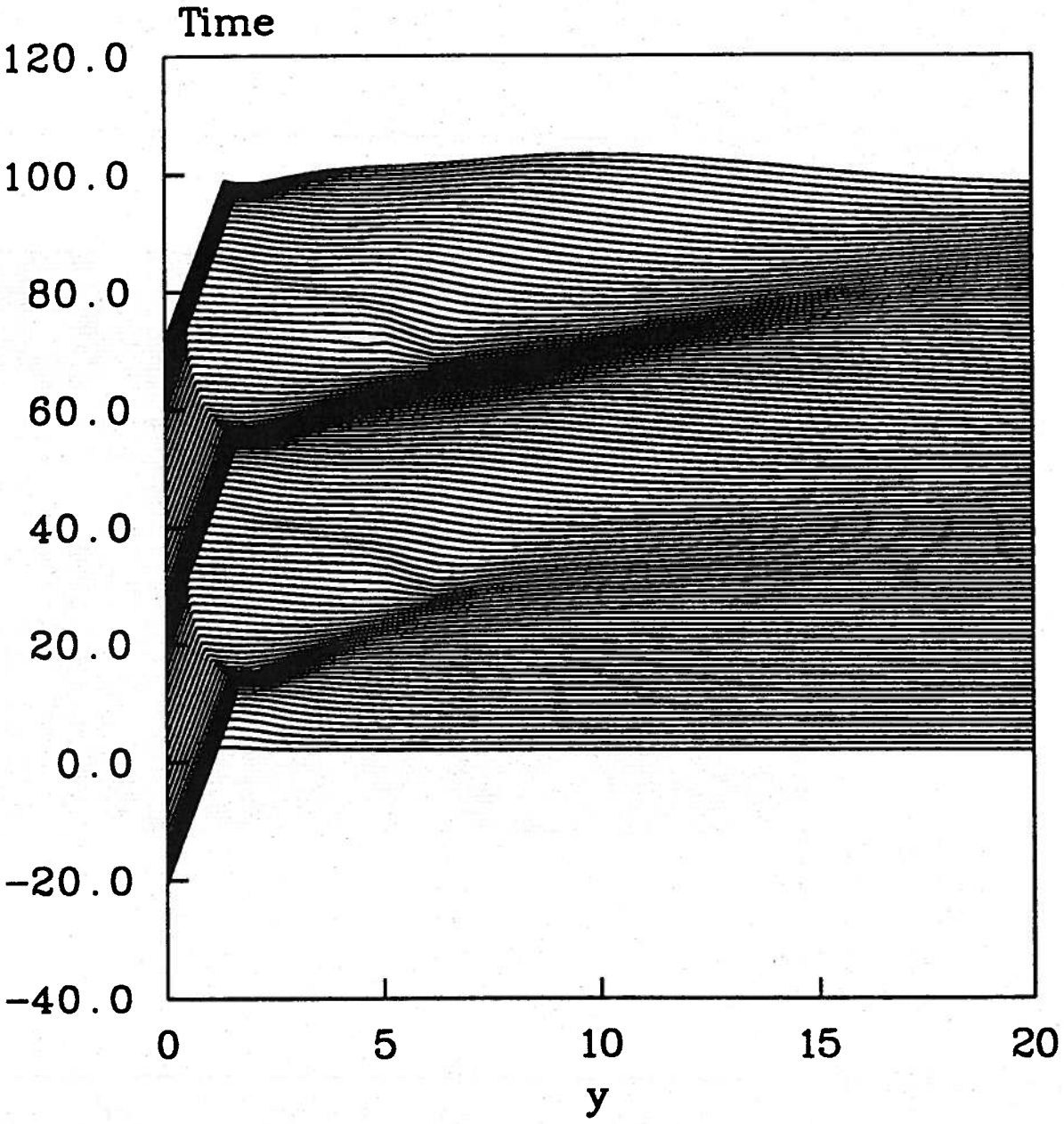

Figure 4.5: Free surface elevation of the nonlinear simulation, stable case. Two-dimensional, oscillating wedge-shaped body with 45 degrees deadrise angle. 10 panels on the body and 90 panels on the free surface. Amplitude=0.5, $k = 0.1309$, FSS number=1.0, $\mathbf{c} = 0.02$, without the truncation effect. Explicit fourth-order Runge-Kutta method.

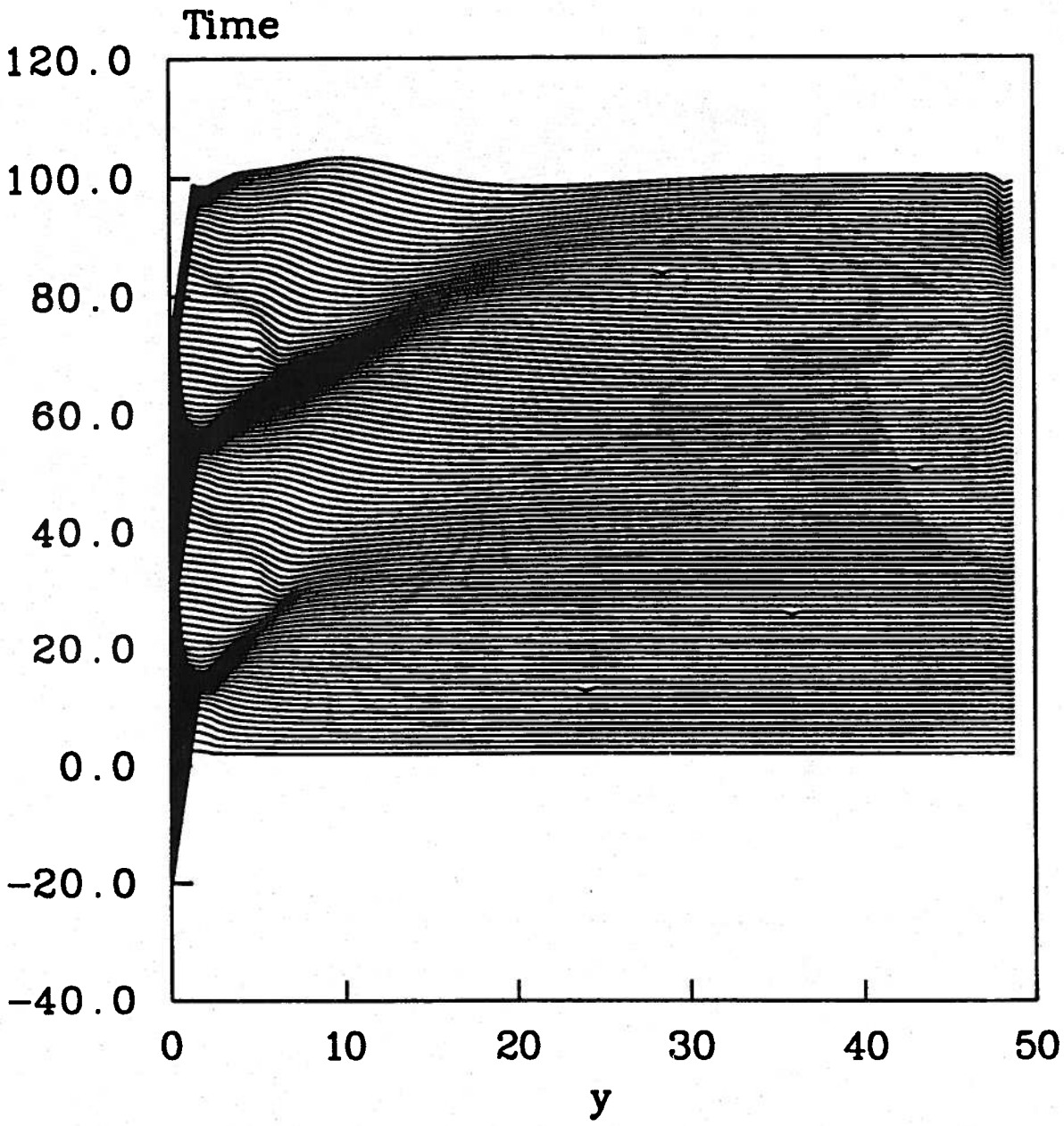

Figure 4.6: Free surface elevation of the nonlinear simulation with the far-field limit, stable case. Two-dimensional wedge-shaped body with 45 degrees dead-rise angle. 10 panels on the body and 90 panels on the free surface. Amplitude=0.5, k = 0.1309, FSS number=1.0, c = 0.02, without the truncation effect. Explicit fourth-order Runge-Kutta method.

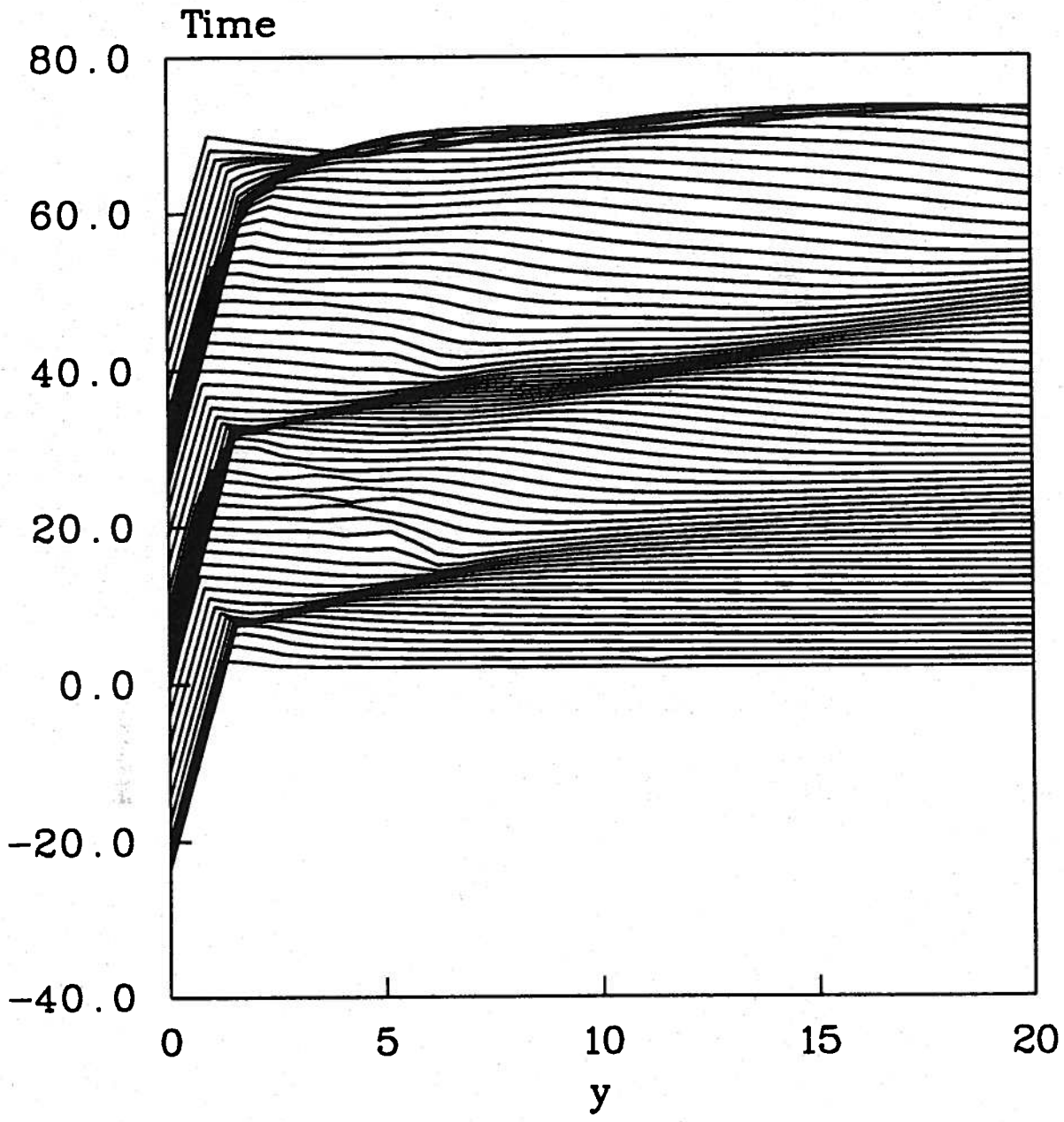

Figure 4.7: Free surface elevation of the nonlinear simulation, unstable case. Two-dimensional wedge-shaped body with 45 degrees deadrise angle. 10 panels on the body and 90 panels on the free surface. Amplitude=0.5, k = 0.1309, FSS number=3.0, c = 0.02, with the truncation effect. Explicit fourth-order Runge-Kutta method.

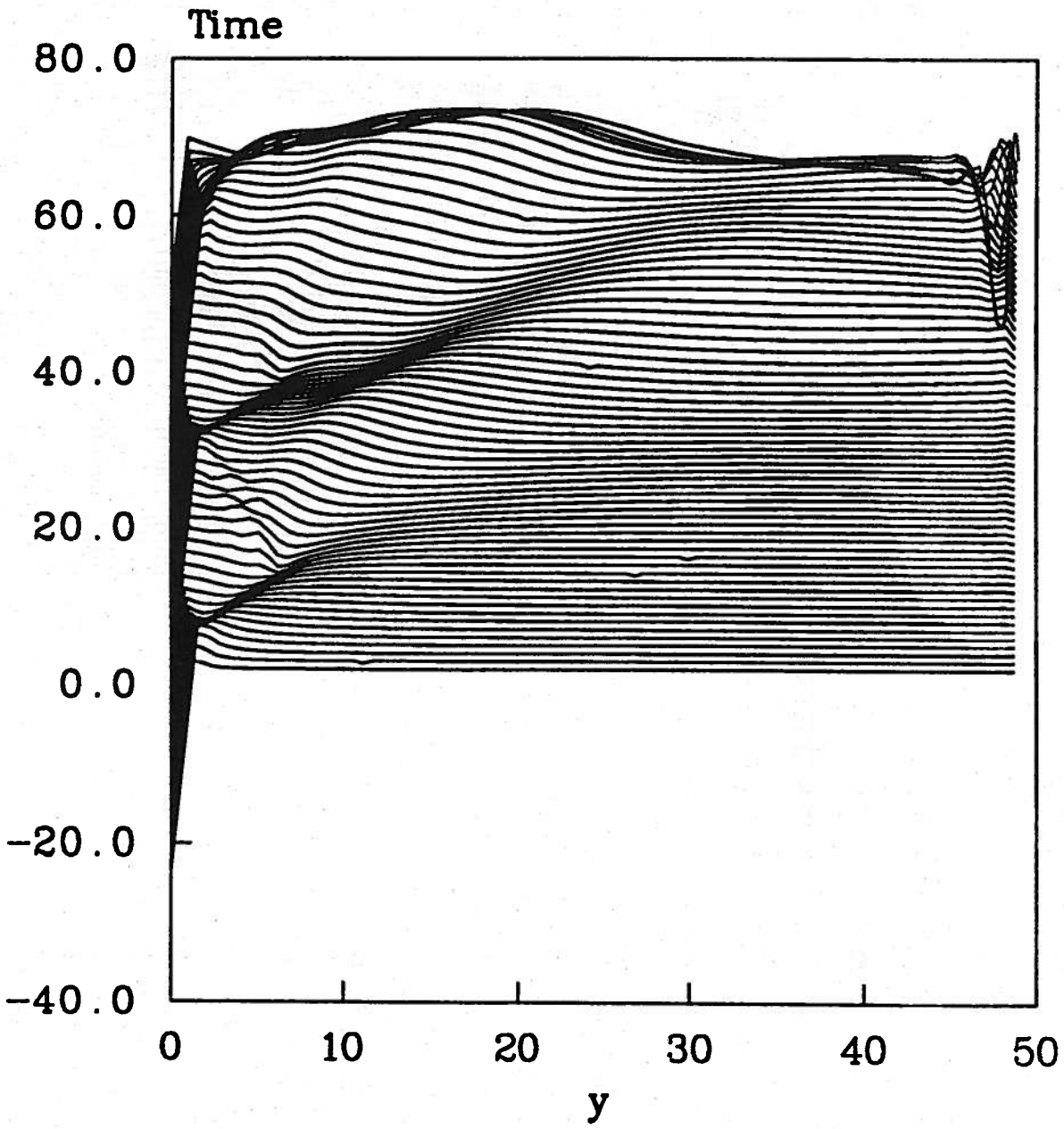

Figure 4.8: Free surface elevation of the nonlinear simulation with the far-field limit,unstable case. Two-dimensional wedge-shaped body with 45 degrees deadrise angle. 10 panels on the body and 90 panels on the free surface. Amplitude=0.5, $k = 0.1309$, FSS number=3.0, $\mathbf{c} = 0.02$, with the truncation effect. Explicit fourth-order Runge-Kutta method.

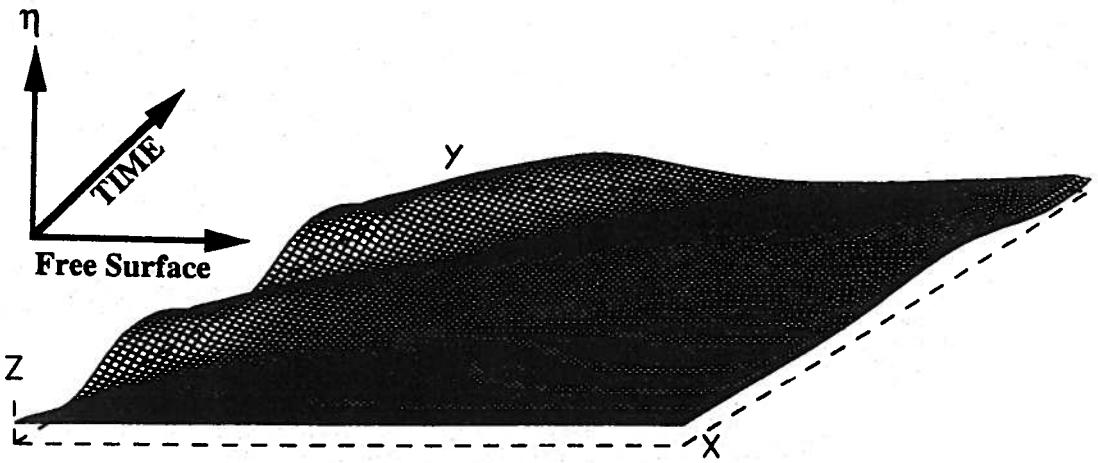

Figure 4.9: Time simulation of the nonlinear potential value distribution, stable case. All the test conditions are the same as Figure 4.5. Two-dimensional wedge-shaped body with 45 degrees deadrise angle. 10 panels on the body and 90 panels on the free surface. Amplitude=0.5, k = 0.1309, FSS number=1.0, c = 0.02, without the truncation effect. Explicit fourth-order Runge-Kutta method.

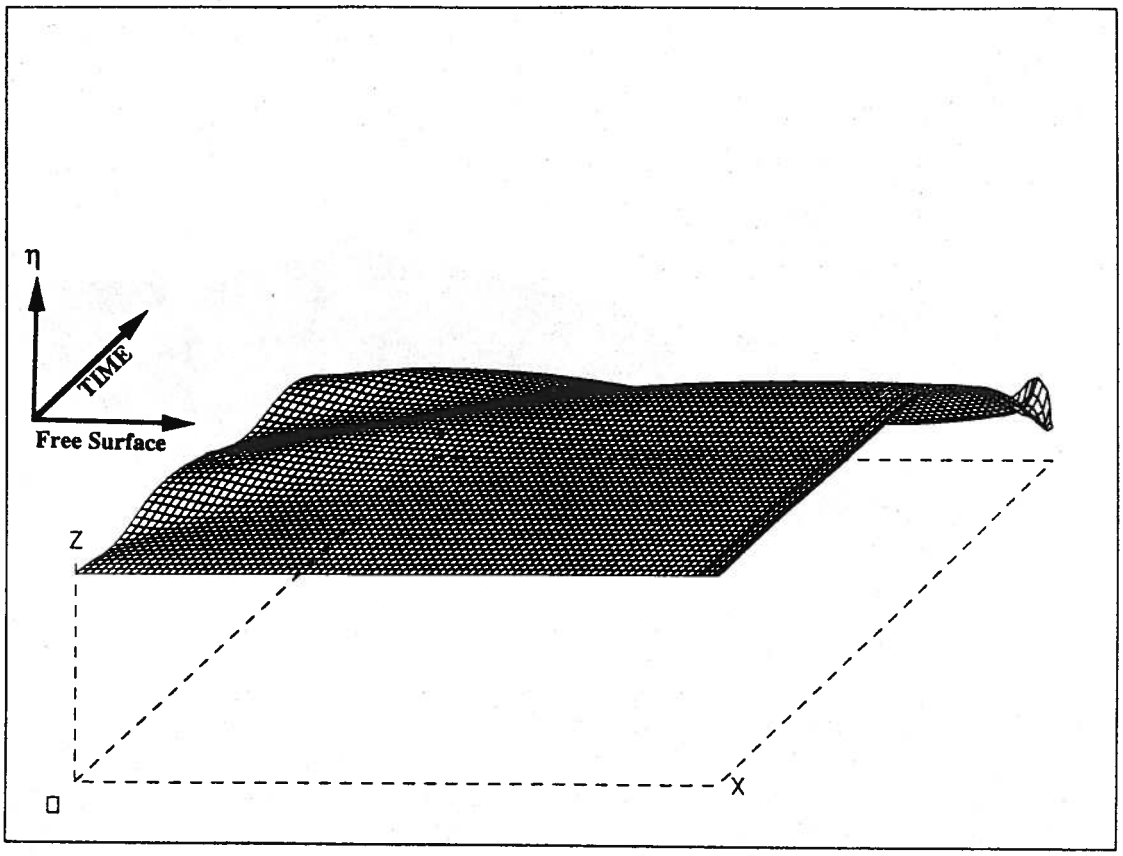

Figure 4.10: Time simulation of the nonlinear potential value distribution, unstable case. All the test conditions are the same as Figure 4.7. Two-dimensional wedge-shaped body with 45 degrees deadrise angle. 10 panels on the body and 90 panels on the free surface. Amplitude=0.5, $k = 0.1309$, FSS number=3.0, $c = 0.02$, with the truncation effect. Explicit fourth-order Runge-Kutta method.

1/c	10		0.01		0.0	
FSS	w/	w/o	w/	w/o	w/	w/o
1.0	1.0	1.0	1.0	1.0	1.0	1.0
↓	↓	↓	↓	↓	↓	↓
7.0	1.0	1.0	1.0	1.0	1.0	1.0
8.0	stable but soon blow up					
9.0	unstable					

Table 4.2: The maximum modulus of the eigenvalues from the nonlinear time simulation results of three-dimensional axisymmetric case with 10 panels on body, 90 on the free surface. Explicit fourth-order Runge-Kutta method. 'w/' represents 'with the truncation effect' and 'w/o' represents 'without the truncation effect'

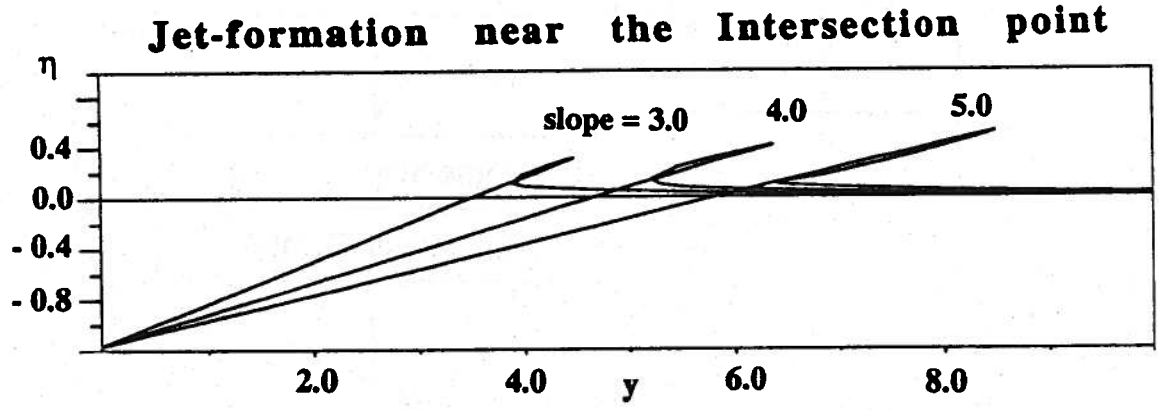

Figure 4.11: Jet-formation at the intersection point. 'slope' represents $\Delta y/\Delta z$. Two-dimensional wedge-shaped body with 45 degrees. FSS number = 5.0 and $\mathbf{c} = 1.0$.

large causing numerical overflow. For a better calculation of the impact force, a proper treatment of the jet needs to be investigated intensively.

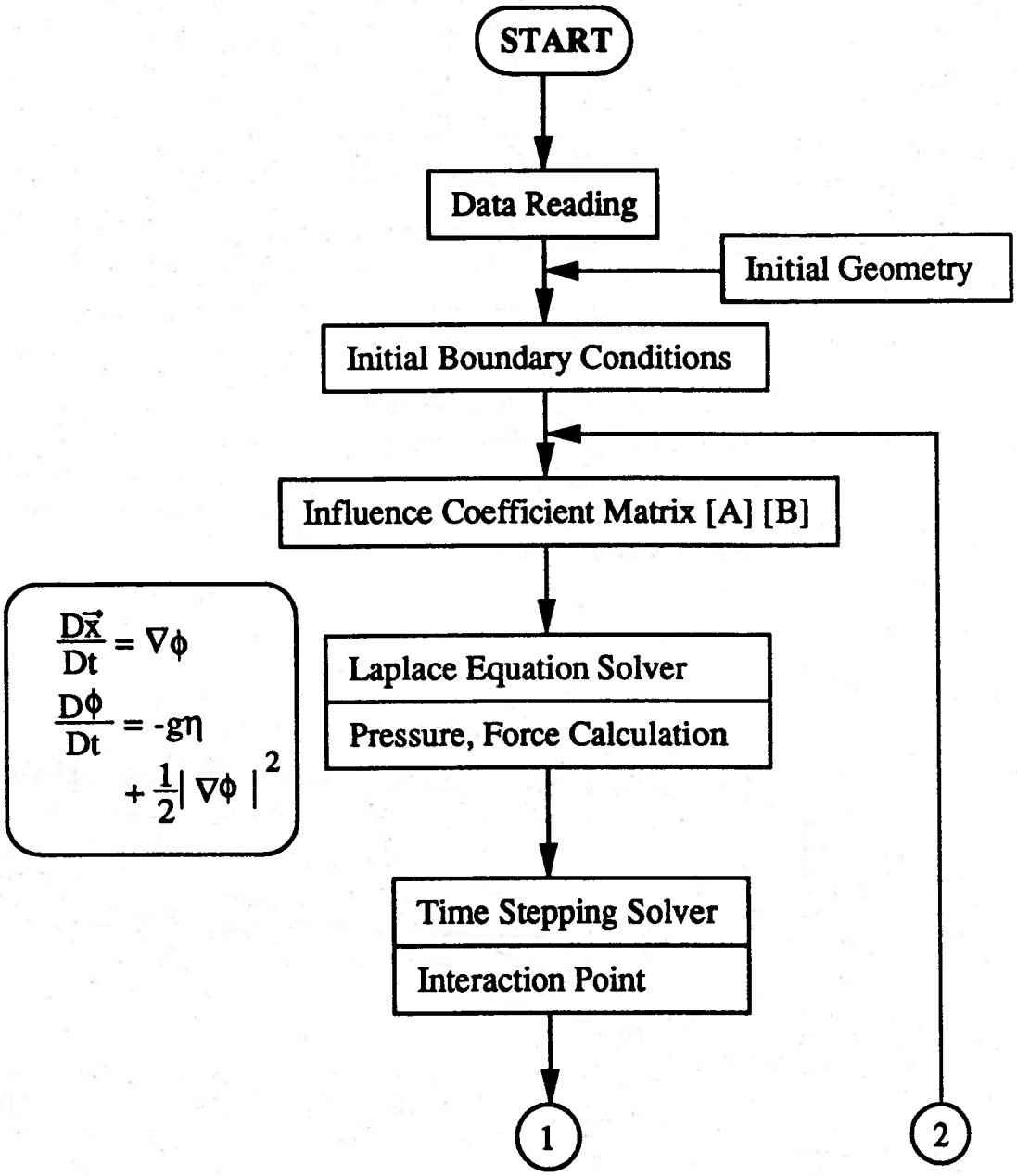

Figure 4.12: Flow chart of the numerical procedure for the nonlinear impact problem. The numerical stability analysis is locally linear, but the time simulation is nonlinear.

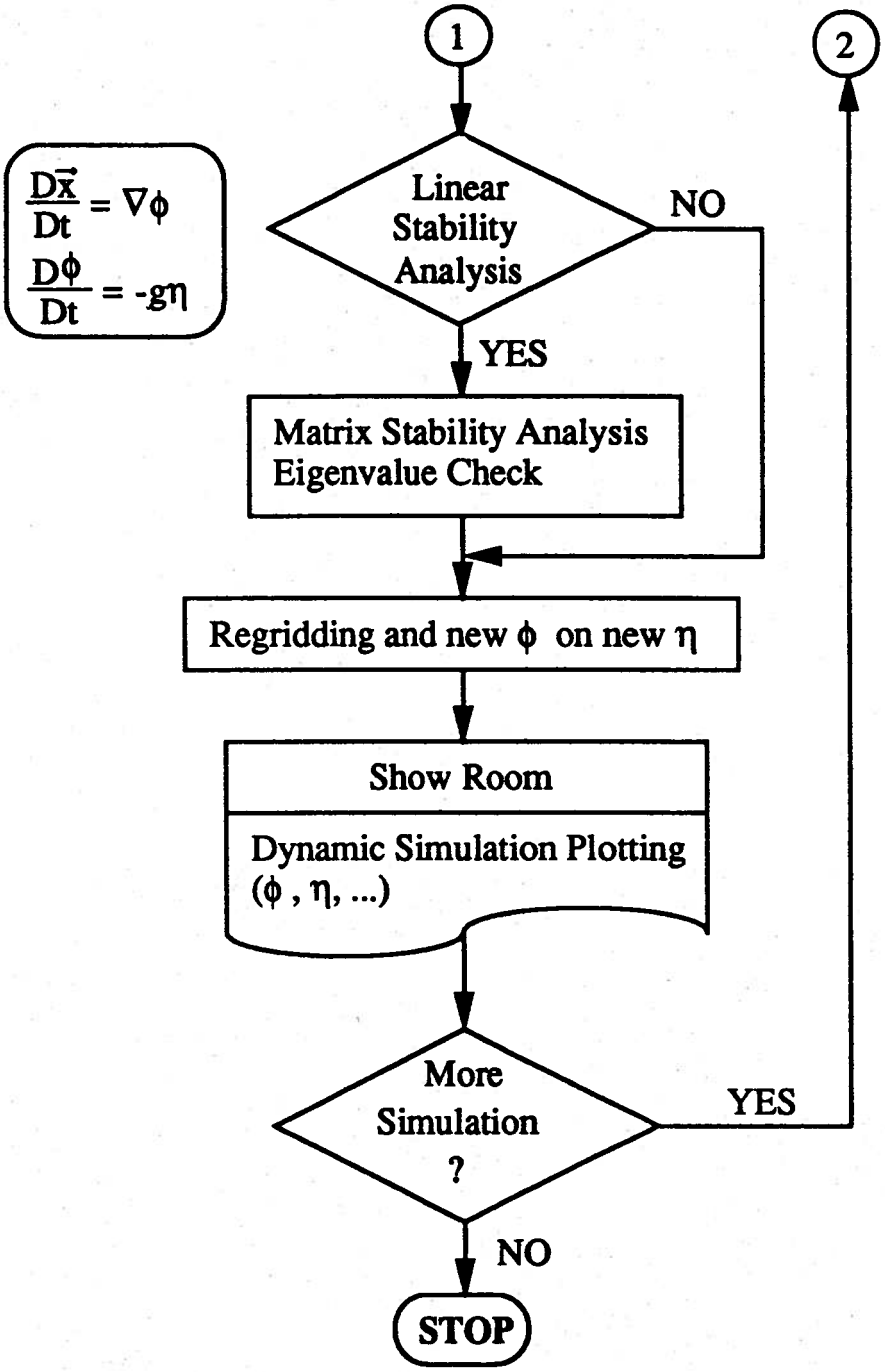

Fig. 4.12 *continued* : Flow chart of the numerical procedure

CHAPTER V

CONCLUSIONS AND FUTURE WORK

The goal of this study is to better understand the complex behavior of body-free surface interaction problems, specifically the hydrodynamics associated with intersecting, non-wallsided bodies experiencing large amplitude motions. As a body moves through the free surface, there are several important factors to consider when predicting forces and motions. These factors include entrance angle, shape of the body, and entrance velocity. For large entrance velocities or large degrees of flare, the body will experience an impact-like behavior which induces a jet to be formed at the body.

Due to the nonlinearities in the body and free surface boundary conditions, this problem is generally only tractable through computation or simulation. Previous studies have encountered numerical instabilities restricting the usefulness of this method. Either the simulation program stops due to floating point difficulties or smoothing techniques are applied raising questions about the validity and accuracy of the computed values.

The purpose of this work is to examine the fundamental causes and solutions surrounding numerical stability and instability. Analytic determination and evaluation of stability regions have been completed leading to closed form solutions for stability

criteria. These criteria have been supported by numerical time simulations.

Initially, simple models for the hydrodynamics are developed yielding basic information on the importance of various parameters and algorithms used in the problem solution schemes. This approach gives confidence in numerical results when closed form analytic solutions are not available. The approach is to increase the level of complexity of the model to finally include the fully nonlinear body and free surface boundary conditions.

5.1 Conclusions

Following the fundamental study of the numerical stability analysis methods, three different boundary problems with increasing degrees of complexity are examined. The different problems dealt with in this thesis are :

1. The near-field boundary problem with one panel on the free surface.
2. The near-field boundary problem with N panels on the free surface.
3. The closed boundary problem with one panel on the free surface (square panel).
4. The closed boundary problem with N panels on the free surface (polygonal shape).
5. The far-field open boundary problem for two-dimensional or three-dimensional axisymmetric bodies (linear forced motion problem).
6. Nonlinear far-field open boundary problem for two-dimensional or three-dimensional axisymmetric bodies (nonlinear forced motion problem).

Linear boundary conditions are used for the cases $1 \sim 5$ and nonlinear boundary conditions are applied for case 6.

From these case studies, this thesis specifically shows :

- *The effects of the Green Function constant* **c**, *Free Surface Stability (FSS) number, the number of panels* N, *panel length* Δx, *and time step size* Δt *on stability*

  The Green function constant **c** acts as a numerical stability moderator for the open-boundary problem. As shown in Table 3.4 and Table 3.5, the stable region for the implicit-like fourth-order Runge-Kutta scheme is created by changing the value of **c**. The value of **c** which changes the unstable region to the stable region is dependent on the far-field truncation limit when using a fixed number of panels on the free surface. This truncation boundary is expressed in terms of the wave number k. The limit is calculated as the wave length traveling with the group velocity for two periods of time. Two examples for the stability regions for changing Green function constant **c** is shown in Tables 3.4 and 3.5. The wave number k of Table 3.4 is 0.3927 with 10 panels on the body and 20 panels on the free surface and the limit value of **c** is 0.1. The wave number of Table 3.5 is 0.1309 with 10 panels on the body and 90 panels on the free surface and the limit value of **c** is 0.02.

  Table 5.1 shows the maximum eigenvalue results for Table 3.4 only with a different wave number, $k = 0.1309$ which is the same as the case of Table 3.5. In Table 5.1, the stable region is limited to $\mathbf{c} = 0.02$. This result shows the main factor in the limiting value of **c** is the truncation boundary represented by the wave number k. The wave number k is used to determine the far-field boundary limit which directly affects the panel length for a fixed number of panels.

c	0.02		0.1		1.0	
FSS	w/	w/o	w/	w/o	w/	w/o
1.0		1.0(c)	1.09(r)	1.191(r)	1.058(r)	
2.0		1.0(c)	1.129(r)	1.281(r)	1.083(r)	
3.0		1.0(c)	1.160(r)	1.354(r)	1.102(r)	
4.0		1.0(c)	1.187(r)	1.419(r)	1.119(r)	
5.0		1.0(c)		1.479(r)		
9.0		0.9999(c)				
10.0		1.255(c)				

Table 5.1: Magnitude of maximum eigenvalues associated with far-field open boundary problem. 45 degree half angle, wedge-shaped two-dimensional body on the free surface with 10 panels on the body, 20 on the free surface. Wave number k=0.1309. Explicit fourth-order Runge-Kutta scheme was used. (r) and (c) denote real or complex eigenvalues respectively. w/ : with truncation effect, w/o : without truncation effect

The FSS number is defined by the panel length Δx and the time step size Δt ($\frac{\pi g(\Delta t)^2}{\Delta x}$). It is found that the numerical stability region is determined roughly by the choice of the numerical scheme and the boundary condition type. For example, the N panel near-field boundary problem has a value of $FSS \simeq 5.0$ as its stability limit for the implicit-like Euler scheme; the square panel closed boundary problem has a value of $FSS \simeq 7.180$ as its stability limit for the implicit-like Euler scheme with the $(\phi, \phi_n, \phi, \phi)$ boundary condition; and the polygonal domain closed boundary problem has a value of $FSS \simeq 4.685$ for the implicit-like scheme with the $(\phi, \phi_n, \phi, \phi)$ boundary condition. The N panel polygonal shapes are essentially independent of the domain geometry for large N. A number of boundary problems are tabulated with boundary conditions, numerical schemes, and stability limits in Table 5.2.

For a fixed time step Δt and a fixed free surface length $\ell_{f.s.}$, the combined effects of the panel length Δx and number of panels can be studied by increasing the number of panels. This induces two important phenomena. First, increasing the number of panels results in small $k \cdot \Delta x$, increasing the level of accuracy of the calculation. Concurrently, increasing the number of panels increases the FSS number so that the numerical scheme approaches the stability limit. This situation is illustrated by the square panel cases with four different conditions (Figures 3.11 $\sim$ 3.16).

Now, consider the case of Δt and Δx being reduced with the same ratio r in a fixed $\ell_{f.s.}$, such that

$$\left.\begin{aligned} FSS_1 &= \tfrac{\pi g(\Delta t)^2}{\Delta x} \\ FSS_2 &= \tfrac{\pi g r^2 (\Delta t)^2}{r \Delta x} \end{aligned}\right\} \quad \frac{FSS_2}{FSS_1} = r,$$

then the FSS number becomes smaller with the ratio r, so that the numerical

Boundary Problem Case	Boundary Condition	Numerical Scheme used	Stability Limit (FSS number)
N panel near-field	ϕ(free surface)	implicit-like Euler	$\simeq 5.0$
square panel closed	ϕ, ϕ_n, ϕ, ϕ	implicit-like Euler	$\simeq 7.180$
polygonal closed	ϕ, ϕ_n, ϕ, ϕ	implicit-like Euler	$\simeq 4.685$
polygonal closed	ϕ, ϕ_n, ϕ, ϕ	implicit-like R.K.	$\simeq 5.0$
polygonal closed	ϕ, ϕ_n, ϕ, ϕ	explicit R.K.	$\simeq 14.3$
far-field 2-D and 3-D open (linear or nonlinear)	ϕ(free surface) ϕ_n(body)	explicit R.K.	$\simeq 10.0$

Table 5.2: FSS number for the various boundary conditions and numerical schemes. The first variable on the boundary condition column is for the free surface. For the polygonal closed boundary problem case, 20 panels, 40 panels, and 90 panels on the free surface were tested. R.K. means the fourth-order Runge-Kutta scheme.

Author(s)	Δx	$k \cdot \Delta x$	Δt	FSS number
Longuet-Higgins and Cokelet (1976)	$2\pi/30$	$2\pi/30(=0.209)$	$\Delta x/V_g$	2.632
Faltinsen (1977)	$\pi a/14$	$0.5\pi/14(=0.112)$	$0.16\sqrt{a/g}$	0.358
Dommermuth and Yue (1986)	$\lambda/40$	$2\pi/40(=0.157)$	$T/40$	0.494
Kang (1988)	$\lambda/80$	$2\pi/80(=0.079)$	$T/100$	0.079

Table 5.3: FSS number for the test conditions of various published papers. λ is the wave length, T is the wave period, and V_g is the group velocity of wave.

scheme is more stable. Also $k\Delta x$ is reduced with the ratio r, so that accuracy becomes higher.

- *Comparison of the previously published papers' test conditions*

  To be in a stable region, the FSS number should be kept small, whereas $k \cdot \Delta x$ should be kept small for accuracy. For reference, the FSS number of the other paper's test conditions are calculated and compared in Table 5.3. All the test conditions are in a fairly low FSS numbered area. Due to the lack of information about the numerical schemes used, it is not possible to check whether the test conditions are in the stable range or not. However, Faltinsen's scheme seems to be unconditionally unstable since his examples were unstable for very small FSS number (=0.358). Refer to Figure 1.2.

- *Conditional/unconditional stability and instability for various time-stepping schemes*

For the simple cases such as one panel in a near-field boundary problem, or the square panel in a closed boundary problem, the analytic form for the stable region is derived. As the panel number increases or as complexity is added, the stability region is investigated numerically. As shown in Sections 3.4 ~ 3.6, the explicit Euler scheme is **unconditionally unstable** and the other schemes, such as the implicit-like Euler, the implicit Euler, the explicit and the implicit-like fourth-order Runge-Kutta schemes are **conditionally stable.**

- *The effect of radiation conditions*

  The radiation condition is an important consideration in two-dimensional numerical analysis. In the far-field open boundary problem, the effect of the truncation limit plays a significant role in the stability analysis. However, in the three-dimensional problem, there is no apparent effect observed for the cases studied in this thesis. Faltinsen's method for the radiation boundary is approximately valid until the wave propagated from the body reaches the boundary. A typical example of the far-field contamination is shown in Figure 4.8.

- *The effect of nonlinearities*

  For an explicit Runge-Kutta scheme, moderate nonlinearities do not produce a significantly different stability region when compared to similar linear problems.

- *The effect of two-dimensional versus three-dimensional problems*

  Two-dimensional and three-dimensional bodies have significant differences in numerical stability region when an explicit fourth-order Runge-Kutta scheme is used. The numerical stability region becomes larger in three dimensions. In the

three-dimensional case, the numerical stability region is essentially independent of the Green function constant c.

- *Problems associated with jet-like behavior i.e. near-singular behavior of G(P,Q) for two panels parallel and close to each other.*

  Stability is a less important issue here. Exceeding certain limits of entrance velocity or deadrise angle will produce a jet-like behavior. The free surface near the body and the body surface itself will form parallel panels. For source distributions, these parallel panels induce a near singular behavior on each other. In this situation, the near singular behavior dominates the problem and another BIM, such as normal dipoles or vortex distributions, is suggested.

5.2 Future Work

- *Force calculations of nonlinear three-dimensional axisymmetric body-wave interaction problem*

  For bodies of decreasing deadrise angles, calculate the impact force acting on the body and compare it with experimental results and with other numerical results. This will be the base study for the jet consideration.

- *The treatment of the jet at the intersection area*

  The main criteria for jet formation should be investigated. Before the jet criteria is met, no special treatment is needed. After the jet criteria is passed, a number of possible treatments should be seriously examined for validity. Vorus(1992) examined two-dimensional jet flow calculations in the planing hull impact problem. Using the assumption of zero-gravity waves, he extended the similarity solutions of Dobrovol'skaya(1969) and Hughes(1972). Considering

gravity and finding the transition region from no-jet flow to jet flow within a certain parameter ranges will be necessary to make real progress with this problem.

- *Far-field accuracy study with the analytic solution of the Cauchy-Poisson problem*

  Expand the Cauchy-Poisson solution in an asymptotic way with large distance r and small time t. The obtained asymptotic solution can be assumed to be valid outside the truncation boundary in the impact problem. As time continues, the far-field solution can be obtained by evaluating the convolution integral. This far-field treatment, which is a function of time and space, will increase the accuracy of the results presented here.

- *Analytic desingularization at the intersection point for the non-wallsided body using Kang's method*

  A special treatment is needed for the singular integral near the intersection point when the body is not wallsided and Kang's (1988) method is used. If the control point of the BIM is located on the nodal point, it is very difficult to remove the weak singularities at the intersection point and still satisfy the kinematic continuity conditions.

- *Expansion to arbitrary three dimensional bodies*

  The impact force calculation with a three-dimensional body and three-dimensional free surface geometry can be considered with or without the forward speed of a ship. To solve this problem more accurately, the three-dimensional spray-sheet also should be intensively investigated in the spray-jet region. For the

stability analysis of the general three-dimensional impact problem with three-dimensional free surface geometry, the matrix stability analysis presented here is valid within the no spray-jet criteria.

APPENDICES

APPENDIX A

Nomenclature

β : phase($k\Delta x$)

Δx : panel length

Δt : time interval between time step

ϕ_i^n : velocity potential of the ith location at the nth time step

$\vec{\xi}$: source point (ξ, η, ζ)

η_i^n : free surface elevation of the ith location at the nth time step

ω : exciting frequency

$[A], [B]$: induced influence coefficient

$\mathbf{c}$: Green function constant ($G_{2D}^* = G_{2D} + \ln \mathbf{c}$)

$\mathrm{ci}(z)$: cosine function

f : exciting force

FSS : Free Surface Stability Number $(= \frac{\pi g(\Delta t)^2}{\Delta x})$

$FG^n(i)$: forcing term of the ith location at the nth time step

$G(\vec{x};\vec{\xi})$: Green function

G : magnification factor $(= \frac{\varepsilon^{n+1}}{\varepsilon^n})$

k : wave number

l_{bottom}, S_{bottom} : 2-D, 3-D bottom boundary

l_B, S_B : 2-D, 3-D body surface boundary

l_f, S_f : 2-D, 3-D free surface boundary

l_∞, S_∞ : 2-D, 3-D near-field/far-field boundary extended to infinity

$\vec{n}$: outward unit normal vector to the domain boundary $\partial\Omega$

$\mathrm{si}(z)$: sine function

$\vec{u}$: velocity of the fluid particle

$\vec{V}$: velocity of the body

$\vec{x}$: field point (x, y, z)

APPENDIX B

Modified Equation for the Euler Scheme of the Free Surface Problem

The potential value at $(n+1)$ and $(N-1)$ time step can be expanded as a Taylor series,

$$\begin{aligned}
\phi^{n+1} &= \phi^n + \Delta t\phi_t^n + \frac{(\Delta t)^2}{2!}\phi_{tt}^n + \frac{(\Delta t)^3}{3!}\phi_{ttt}^n + \frac{(\Delta t)^4}{4!}\phi_{tttt}^n + \cdots \\
\phi^n &= \phi^n \\
\phi^{n-1} &= \phi^n - \Delta t\phi_t^n + \frac{(\Delta t)^2}{2!}\phi_{tt}^n - \frac{(\Delta t)^3}{3!}\phi_{ttt}^n + \frac{(\Delta t)^4}{4!}\phi_{tttt}^n + \cdots
\end{aligned}$$

$$\phi^{n+1} - 2\phi^n + \phi^{n-1} = (\Delta t)^2\phi_{tt}^n + \frac{(\Delta t)^4}{12}\phi_{tttt}^n + \cdots \tag{B.1}$$

(1) Explicit Scheme

The linearized combined free surface boundary condition is

$$\phi_{tt} = -g\phi_z^{n-1} \tag{B.2}$$

$$\begin{aligned}
\Rightarrow \quad & \frac{\phi^{n+1} - 2\phi^n + \phi^{n-1}}{(\Delta t)^2} = -g\phi_z^{n-1} \\
\Rightarrow \quad & \phi_{tt}^n + \frac{(\Delta t)^2}{12}\phi_{tttt}^n + \cdots = -g\phi_z^{n-1} \\
\Rightarrow \quad & \phi_{tt}^n = -g\phi_z^{n-1} - \frac{(\Delta t)^2}{12}\phi_{tttt}^n + \cdots
\end{aligned} \tag{B.3}$$

(2) Implicit-like Scheme

$$\phi_{tt} = -g\phi_x^n \tag{B.4}$$

$$\Rightarrow \quad \phi_{tt}^n = -g\phi_x^n - \frac{(\Delta t)^2}{12}\phi_{tttt}^n + \cdots \tag{B.5}$$

Original Equation (B.2) is changed to Equation (B.5) because the second time derivative of ϕ^n is substituted to a finite scheme. Equation (B.5) has to be changed again due to the choice of the solution method of ϕ_x^n and the additional term surely includes the Δx and spatial derivative related terms.

For the exact modified equation, ϕ_x should be expressed as a distribution of ϕ which is a result from the BIM. The solution of the elliptic equation has the characteristics that the domain of influence is the while. Thus, ϕ_x will be expressed with all ϕ's on the boundary.

APPENDIX C

Analytic Calculation for Fourth-order Runge-Kutta Method

Suppose that the differential equation $\frac{dy}{dx} = f(x,y)$ is to be solved and that the values of the function $y(x)$ are known. Then, $y(x+h)$ can be expanded using the Talyor expansion and Δy is expressed as the order of h.

$$y(x+h) = y(x) + hy'(x) + \frac{h^2}{2!}y''(x) + \cdots \tag{C.1}$$

$$\Delta y = y(x+h) - y(x) = hy'(x) + \frac{h^2}{2!}y''(x) + \frac{h^3}{3!}y'''(x) + \cdots \tag{C.2}$$

$$= hf + \frac{h^2}{2}(f_x + f_y f)$$

$$+\frac{h^3}{6}\{f_{xx} + 2f_{xy}f + f_{yy}f^2 + f_y(f_x + f - yf)\} + \cdots \tag{C.3}$$

Δy also can be expressed as a combination of k_1, k_2, k_3, and k_4.

$$\Delta y = ak_1 + bk_2 + ck_3 + dk_4$$

where

$$k_1 = hf(x,y) \tag{C.4}$$

$$k_2 = hf(x+mh, y+mk_1) = hf(x+mh, y+mhf)$$

$$= h(f + mhf_x + mhff_y + \cdots) \tag{C.5}$$

$$k_3 = hf(x+nh, y+nk_2) = h(f + nhf_x + nk_2f_y + \cdots) \tag{C.6}$$

$$k_4 = hf(x+ph, y+pk_3) = h(f + phf_x + pk_3f_y + \cdots) \tag{C.7}$$

From the h identity in the equations between Equation (C.3) and Equations (C.4) $\sim$ (C.7), variables $a,\ b,\ c,;d$ and $m,\ n,\ ,p$ is decided from the system of equations below ;

$$
\begin{aligned}
&1)\,h \quad identity \quad : a+b+c+d=1\\
&2)\,h^2 \quad identity \quad : bm+cn+dp=1/2\\
&3)\,h^3 \quad identity \quad \begin{cases} bm^2+cn^2+dp^2=1/3\\ cmn+dnp=1/6 \end{cases}\\
&4)h^4 \quad identity \quad \begin{cases} bm^3+cn^3+dp^3=1/4\\ cmn^2+dnp^2=1/8\\ cm^2n+dn^2p=1/12\\ dmnp=1/24 \end{cases}
\end{aligned}
$$

$$
\begin{cases} a=1/6 \quad b=1/3 \quad c=1/3 \quad d=1/6\\ m=1/2 \quad n=1/2 \quad p=1 \end{cases}
$$

so that

$$
\begin{aligned}
\Delta y &= \frac{1}{6}(k_1+2k_2+2k_3+k_4)\\
k_1 &= hf(x,y)\\
k_2 &= hf(x+\frac{h}{2},y+\frac{k_1}{2})\\
k_3 &= hf(x+\frac{h}{2},y+\frac{k_2}{2})\\
k_4 &= hf(x+h,y+k_3)
\end{aligned}
$$

Variable k is used for the intermediate value of dynamic free surface boundary condition, and another variable l is used for the value of kinematic free surface boundary condition. Thus, fourth-order Runge-Kutta scheme can be written as;

$$
\phi^{n+1} = \phi^n+\frac{1}{6}(k_1+2k_2+2k_3+k_4)
$$

$$\eta^{n+1} = \eta^n + \frac{1}{6}(l_1 + 2l_2 + 2l_3 + l_4)$$

C.1 Method 1 : Explicit Scheme

The intermediate increments of ϕ is defined as k_1, k_2, k_3, and k_4, and the intermediate increments of η is as l_1, l_2, l_3, and l_4. As shown in the equation below, k_1 and l_1 are calculated using the information at the (n) time step, k_2 and l_2 using the information at k_1 and l_1 intermediate step, k_3 and l_3 using the information at k_2 and l_2 intermediate step, and k_4 and l_4 using at k_3 and l_3 step. Applying the Explicit fourth-order Runge-Kutta scheme to the linear free surface boundary conditions are;

$$\begin{aligned}
&\frac{\partial \phi}{\partial t} = -g\eta && && \frac{\partial \eta}{\partial t} = \phi_z \\
&k_1 = -g\Delta t \eta^n && \times && l_1 = \Delta t \phi_z^n \\
&k_2 = -g\Delta t(\eta^n + \phi_z^n \tfrac{\Delta t}{2}) && \times && l_2 = \Delta t(\phi_z^{n+\frac{1}{2}})_1 \\
&k_3 = -g\Delta t\{\eta^n + (\phi_z^{n+\frac{1}{2}})_1 \tfrac{\Delta t}{2}\} && \times && l_3 = \Delta t(\phi_z^{n+\frac{1}{2}})_2 \\
&k_4 = -g\Delta t\{\eta^n + (\phi_z^{n+\frac{1}{2}})_2 \Delta t\} && && l_4 = \Delta t(\phi_z^{n+1})_3
\end{aligned}$$

$$\begin{aligned}
\phi^{n+1} &= \phi^n + \frac{1}{6}(k_1 + 2k_2 + 2k_3 + k_4) && \text{(C.8)} \\
&= \phi^n - \frac{g\Delta t}{6}\{6\eta^n + \Delta t[\phi_z^n + (\phi_z^{n+\frac{1}{2}})_1 + (\phi_z^{n+\frac{1}{2}})_2]\} \\
&= \phi^n - \frac{g\Delta t}{6}\{6\eta^n + l_1 + l_2 + l_3\} && \text{(C.9)} \\
\eta^{n+1} &= \eta^n + \frac{1}{6}(l_1 + 2l_2 + 2l_3 + l_4) && \text{(C.10)}
\end{aligned}$$

ϕ_z^n, $(\phi_z^{n+\frac{1}{2}})_1$, and $(\phi_z^{n+\frac{1}{2}})_2$ is calculated from the boundary value problem (BVP) and substituted into Equations (C.8) and (C.10).

$$\begin{aligned}
\phi_i^{n+1} = \phi_i^n &- \frac{1}{6}g(\Delta t)^2 \sum_{j=1}^{N}\{3^* C_{ij} - \frac{1}{4}g(\Delta t)^2 \sum_{k=1}^{N} C_{ik} C_{kj}^*\}\phi_j^n \\
&- g\Delta t\,[\eta_i^n - \frac{1}{6}g(\Delta t)^2 \sum_{j=1}^{N}(C_{ij}^* \eta_j^n)]
\end{aligned}$$

$$- \frac{1}{6}g(\Delta t)^2[\,FP_i^n + 2FP_i^{n+\frac{1}{2}} - \frac{1}{4}g(\Delta t)^2 \sum_{j=1}^{N} C_{ij}^* FP_j^n\,] \qquad \text{(C.11)}$$

where

$$FP_i^n = \sum_{j=nonf.s.} C_{ij}^3 \cdot \left((\frac{\partial \phi}{\partial n})_j \text{ or } \phi_j \right)$$

as shown in Equation 3.10,

$$\begin{aligned} \eta_i^{n+1} = \eta_i^n \;&+\; \Delta t\{ \sum_{j=1}^{N} C_{ij}^* \phi_j^n - \frac{g(\Delta t)^2}{6} \sum_{j=1}^{N} (\sum_{k=1}^{N} C_{ik}^* C_{kj}^*) \phi_j^n \} \\ &- \frac{1}{2}g(\Delta t)^2 \sum_{j=1}^{N} C_{ij}^* \eta_j^n + \frac{(g(\Delta t)^2)^2}{24} \sum_{j=1}^{N} (\sum_{k=1}^{N} C_{ik}^* C_{kj}^*) \eta_j^n \\ &+ \frac{\Delta t}{6}\{\, FP_i^n + 4FP_i^{n+\frac{1}{2}} + FP_i^{n+1} - \frac{g(\Delta t)^2}{2} \sum_{j=1}^{N} C_{ij}^* FP_j^n \\ &\quad - \frac{g(\Delta t)^2}{2} \sum_{j=1}^{N} C_{ij}^* FP_j^{n+\frac{1}{2}} \} \end{aligned} \qquad \text{(C.12)}$$

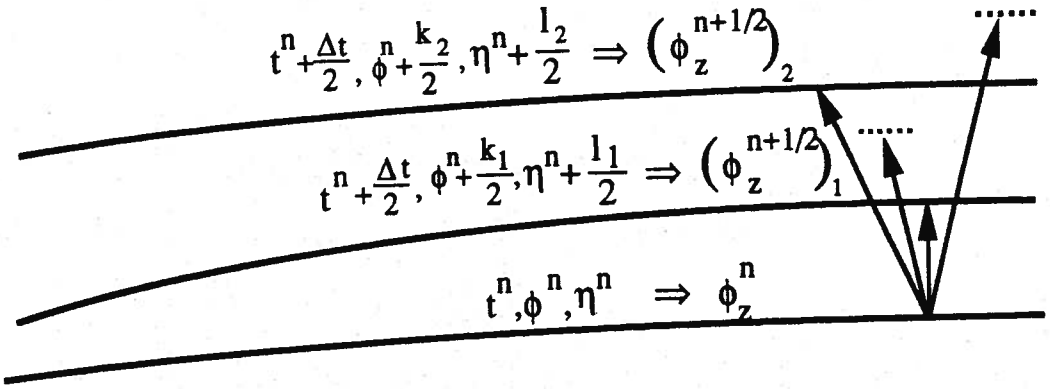

Figure C.1: Fourth-order Runge-Kutta method on the free surface

Previous calculations are used for the time step procedure. It is explained below step by step.

$$\frac{\partial \phi}{\partial t} = -g\eta \qquad\qquad \frac{\partial \eta}{\partial t} = \phi_z$$

Step 1 ;

$$d\phi_1 = k_1 = -g\Delta t\,\eta^n \qquad d\eta_1 = l_1 = \Delta t\,\phi_z^n$$

$$\phi^n + \frac{d\phi_1}{2} \text{ at } \eta^n + \frac{d\eta_1}{2}$$

Solve boundary value problem (BVP) to get new $(\phi_z)_1^{n+\frac{1}{2}}$

Step 2 ;

$$d\phi_2 = k_2 = -g\Delta t\,(\eta^n + \frac{d\eta_1}{2}) \qquad d\eta_2 = l_2 = \Delta t\,(\phi_z)_1^{n+\frac{1}{2}}$$

$$\phi^n + \frac{d\phi_2}{2} \text{ at } \eta^n + \frac{d\eta_2}{2}$$

Solve BVP to get new $(\phi_z)_2^{n+\frac{1}{2}}$

Step 3 ;

$$d\phi_3 = k_3 = -g\Delta t\,(\eta^n + \frac{d\eta_2}{2}) \qquad d\eta_3 = l_3 = \Delta t\,(\phi_z)_2^{n+\frac{1}{2}}$$

$$\phi^n + d\phi_3 \text{ at } \eta^n + d\eta_3$$

Solve BVP to get new $(\phi_z)_3^{n+1}$

Step 4 ;

$$d\phi_4 = k_4 = -g\Delta t\,(\eta^n + d\eta_3) \qquad d\eta_4 = l_4 = \Delta t\,(\phi_z)_3^{n+1}$$

$$\begin{cases} \phi^{n+1} &= \phi^n + \frac{1}{6}(k_1 + 2k_2 + 2k_3 + k_4) \\ \\ \eta^{n+1} &= \eta^n + \frac{1}{6}(l_1 + 2l_2 + 2l_3 + l_4) \end{cases}$$

As a last step, solve BVP to get new ϕ_z^{n+1}

C.2 Method 2 : Implicit-like Scheme

In this Implicit-like scheme, one of the two intermediate increments are used for the calculation of the other in the step. As shown below, l_1 is calculated using the information of the (n) time step and l_1 is used for the calculation of k_1, l_2 used for k_2, and so does l_3 and l_4.

$$\begin{array}{lll} \frac{\partial \phi}{\partial t} = -g\eta & & \frac{\partial \eta}{\partial t} = \phi_z \\ k_1 = -g\Delta t\, \eta^n & \searrow & l_1 = \Delta t\, \phi_z^n \\ k_2 = -g\Delta t \{\eta^n + (\phi_z^{n+\frac{1}{2}})_1 \frac{\Delta t}{2}\} & \searrow\leftarrow & l_2 = \Delta t\, (\phi_z^{n+\frac{1}{2}})_1 \\ k_3 = -g\Delta t \{\eta^n + (\phi_z^{n+\frac{1}{2}})_2 \frac{\Delta t}{2}\} & \searrow\leftarrow & l_3 = \Delta t\, (\phi_z^{n+\frac{1}{2}})_2 \\ k_4 = -g\Delta t \{\eta^n + (\phi_z^{n+\frac{1}{2}})_3 \Delta t\} & \leftarrow & l_4 = \Delta t\, (\phi_z^{n+1})_3 \end{array}$$

$$\begin{aligned} \phi^{n+1} &= \phi^n + \frac{1}{6}(k_1 + 2k_2 + 2k_3 + k_4) \\ &= \phi^n - \frac{g\Delta t}{6}\{6\eta^n + \Delta t\,[(\phi_z^{n+\frac{1}{2}})_1 + (\phi_z^{n+\frac{1}{2}})_2 + (\phi_z^{n+\frac{1}{2}})_3]\} \\ &= \phi^n - \frac{g\Delta t}{6}\{6\eta^n + l_2 + l_3 + l_4\} \qquad \text{(C.13)} \\ \eta^{n+1} &= \eta^n + \frac{1}{6}(l_1 + 2l_2 + 2l_3 + l_4) \qquad \text{(C.14)} \end{aligned}$$

$$\phi_i^{n+1} = \phi_i^n \;-\; \frac{1}{2}g(\Delta t)^2 \sum_{j=1}^{N} C_{ij}^* \phi_j^n - \frac{1}{8}(g(\Delta t)^2)^2 (\sum_{j=1}^{N}\sum_{k=1}^{N} C_{ik}^* C_{kj}^*)\phi_j^n$$

$$
\begin{aligned}
&- \frac{1}{48}(g(\Delta t)^2)^3(\sum_{j=1}^{N}\sum_{k=1}^{N} C_{ik}^{*}\sum_{p=1}^{N} C_{kp}^{*}C_{pj}^{*})\phi_j^n \\
&- g\Delta t\{\eta_i^n - \frac{1}{3}g(\Delta t)^2\sum_{j=1}^{N}(C_{ij}^{*}\eta_j^n) + \frac{1}{16}(g(\Delta t)^2)^2(\sum_{j=1}^{N}\sum_{k=1}^{N} C_{ik}^{*}C_{kj}^{*})\eta_j^n \\
&\qquad -\frac{1}{96}(g(\Delta t)^2)^3\sum_{j=1}^{N}(\sum_{k=1}^{N} C_{ik}^{*}\sum_{p=1}^{N} C_{kp}^{*}C_{pj}^{*})\eta_j^n\} \\
&- \frac{1}{3}g(\Delta t)^2[FP_i^{n+\frac{1}{2}} - \frac{1}{6}g(\Delta t)^2 FP_i^{n+1} + \frac{1}{8}(g(\Delta t)^2)^2\sum_{j=1}^{N} C_{ij}^{*}FP_j^{n+\frac{1}{2}} \\
&- \frac{1}{48}(g(\Delta t)^2)^3\sum_{j=1}^{N} C_{ij}^{*}\sum_{k=1}^{N} C_{jk}^{*}FP_j^{n+\frac{1}{2}} \qquad \text{(C.15)}
\end{aligned}
$$

where

$$
FP_i^n = \sum_{j=nonf.s.} C_{ij}^3 \cdot \left((\frac{\partial\phi}{\partial n})_j \text{ or } \phi_j\right)
$$

as shown in Equation 3.10,

$$
\begin{aligned}
\eta_i^{n+1} = \eta_i^n \;+\; &\Delta t\{\sum_{j=1}^{N} C_{ij}^{*}\phi_j^n - \frac{g(\Delta t)^2}{6}\sum_{j=1}^{N}(\sum_{k=1}^{N} C_{ik}^{*}C_{kj}^{*})\phi_j^n \\
&\qquad +\frac{1}{48}(g(\Delta t)^2)^2(\sum_{j=1}^{N}\sum_{k=1}^{N} C_{ik}^{*}\sum_{p=1}^{N} C_{kp}^{*}C_{pj}^{*})\phi_j^n\} \\
&- \frac{1}{2}g(\Delta t)^2\sum_{j=1}^{N} C_{ij}^{*}\eta_j^n + \frac{(g(\Delta t)^2)^2}{12}\sum_{j=1}^{N}(\sum_{k=1}^{N} C_{ik}^{*}C_{kj}^{*})\eta_j^n \\
&- \frac{1}{96}(g(\Delta t)^2)^3\sum_{j=1}^{N}(\sum_{k=1}^{N} C_{ik}^{*}\sum_{p=1}^{N} C_{kp}^{*}C_{pj}^{*})\,\eta_j^n \\
&+ \frac{\Delta t}{6}\{FP_i^n + 4FP_i^{n+\frac{1}{2}} + FP_i^{n+1} - g(\Delta t)^2\sum_{j=1}^{N} C_{ij}^{*}FP_j^{n+\frac{1}{2}} \\
&\qquad +\frac{(g(\Delta t)^2)^2}{8}\sum_{j=1}^{N} C_{ij}^{*}(\sum_{k=1}^{N} C_{jk}^{*}FP_k^{n+\frac{1}{2}})\} \qquad \text{(C.16)}
\end{aligned}
$$

As an example, in the square panel case which has one panel on the free surface (Section 3.5.1), ϕ^{n+1} and η^{n+1} are obtained from Equations (C.15) and (C.16),

$$
\begin{Bmatrix} \phi \\ \eta \end{Bmatrix}^{n+1} = \begin{bmatrix} D_{11} & D_{12} \\ D_{21} & D_{22} \end{bmatrix}\begin{Bmatrix} \phi \\ \eta \end{Bmatrix}^{n} + \begin{Bmatrix} f_1 \\ f_2 \end{Bmatrix}^{n} \qquad \text{(C.17)}
$$

where

$$D_{11} = 1 - \frac{1}{2}g(\Delta t)^2 C_{11} - \frac{1}{8}g^2(\Delta t)^4 C_{11}^2 - \frac{1}{48}g^3(\Delta t)^6 C_{11}^3$$

$$D_{12} = -g\Delta t\{1 - \frac{1}{3}g(\Delta t)^2 C_{11} + \frac{1}{16}g^2(\Delta t)^4 C_{11}^2 - \frac{1}{96}g^3(\Delta t)^6 C_{11}^3\}$$

$$D_{21} = \Delta t\{C_{11} - \frac{g(\Delta t)^2}{6}C_{11}^2 + \frac{1}{48}g^2(\Delta t)^4\}$$

$$D_{22} = 1 - \frac{1}{2}g(\Delta t)^2 C_{11} + \frac{1}{12}g^2(\Delta t)^4 C_{11}^2 - \frac{1}{96}g^3(\Delta t)^6 C_{11}^3$$

C.3 Method 3 : Kang's Method

Kang's method is closely following the Explicit scheme. The difference is that, in his method, k_2, k_3, and k_4 are calculated with the accumulated wave height η which, seemingly causes the numerical instability in the time simulation.

$$k_1 = -g\Delta t\eta^n$$

$$k_2 = -g\Delta t\{\eta^n + \phi_x^n\frac{\Delta t}{2}\}$$

$$k_3 = -g\Delta t\{\eta^n + \phi_x^n\frac{\Delta t}{2} + (\phi_x^{n+\frac{1}{2}})_1\frac{\Delta t}{2}\}$$

$$k_4 = -g\Delta t\{\eta^n + \phi_x^n\frac{\Delta t}{2} + (\phi_x^{n+\frac{1}{2}})_1\frac{\Delta t}{2} + (\phi_x^{n+\frac{1}{2}})_2\frac{\Delta t}{2}\}$$

$$l_1 = \Delta t\phi_x^n$$

$$l_2 = \Delta t(\phi_x^{n+\frac{1}{2}})_1$$

$$l_3 = \Delta t(\phi_x^{n+\frac{1}{2}})_2$$

$$l_4 = \Delta t(\phi_x^{n+1})_3$$

where

$$(\phi_x^{n+\frac{1}{2}})_1 = \sum_{j=1}^{N} C_{ij}^*(\phi_j^n + \frac{k_{1j}}{2}) + FP_i^{n+\frac{1}{2}}$$

$$(\phi_x^{n+\frac{1}{2}})_2 = \sum_{j=1}^{N} C_{ij}^*(\phi_j^n + \frac{k_{1j}}{2} + \frac{k_{2j}}{2}) + FP_i^{n+\frac{1}{2}}$$

$$(\phi_z^{n+\frac{1}{2}})_2 = \sum_{j=1}^{N} C_{ij}^*(\phi_j^n + \frac{k_{1j}}{2} + \frac{k_{2j}}{2} + k_{3j}) + FP_i^{n+1}$$

$$\phi_z^n = \sum_{j=1}^{N} C_{ij}^* \phi_j + FP_i^n$$

Using equations (C.8)–(C.10), we can have the form for ϕ^{n+1} and η^{n+1}.

$$\begin{aligned}\phi_i^{n+1} = \phi_i^n &- \frac{1}{6}g(\Delta t)^2 \sum_{j=1}^{N}\{5C_{ij}^* - \frac{1}{4}g(\Delta t)^2 \sum_{k=1}^{N} C_{ik}^* C_{kj}^*\}\phi_j^n \\ &- g\Delta t\,[\eta_i^n - \frac{7}{24}g(\Delta t)^2 \sum_{j=1}^{N}(C_{ij}^* \eta_j^n)] \\ &- \frac{1}{12}g(\Delta t)^2[5FP_i^n + 5FP_i^{n+\frac{1}{2}} - \frac{1}{2}g(\Delta t)^2 \sum_{j=1}^{N} C_{ij}^* FP_j^n] \end{aligned} \quad \text{(C.18)}$$

where

$$FP_i^n = \sum_{j=nonf.s.} C_{ij}^3 \cdot \left((\frac{\partial \phi}{\partial n})_j \text{ or } \phi_j\right)$$

as shown in Equation 3.10,

$$\begin{aligned}\eta_i^{n+1} = \eta_i^n &+ \Delta t\{\sum_{j=1}^{N} C_{ij}^* \phi_j^n - \frac{5}{6}g(\Delta t)^2 \sum_{j=1}^{N}(\sum_{k=1}^{N} C_{ik}^* C_{kj}^*)\phi_j^n\} \\ &- \frac{3}{4}g(\Delta t)^2 \sum_{j=1}^{N} C_{ij}^* \eta_j^n + \frac{1}{48}(g(\Delta t)^2)^2 \sum_{j=1}^{N}(\sum_{k=1}^{N} C_{ik}^* C_{kj}^*)\eta_j^n \\ &+ \frac{\Delta t}{6}\{FP_i^n + 4FP_i^{n+\frac{1}{2}} + FP_i^{n+1} - \frac{3}{4}g(\Delta t)^2 \sum_{j=1}^{N} C_{ij}^* FP_j^n \\ &\quad - \frac{g(\Delta t)^2}{4} \sum_{j=1}^{N} C_{ij}^* FP_j^{n+\frac{1}{2}}\} \end{aligned} \quad \text{(C.19)}$$

APPENDIX D

Calculation of the Stable Region by von Neumann Method

In the numerical stability analysis for the Euler scheme, the equation of the magnification factor is second order algebraic equation. This equation has two roots and the magnitude of the roots determines the stability. The roots for the second order algebraic equation can be calculated easily using the well-known formula for the root. The stability region is defined as the area where the magnitude of the both roots be less than or equal to 1. In this appendix, the ways for finding the stable region are discussed. The first one is simple algebraic calculation, but can not be used for the higher order algebraic equation. The second method is applicable to the higher order.

D.1 Simple case

$$G^2 - (2+p)G + 1 = 0$$

$$G = \frac{2+p \pm \sqrt{p^2+4p}}{2}$$

1. $p > 0$: No region for the two roots to have $G < 1$.

2. $p < 0$:

- If $p^2 + 4p > 0$, then p should be less than -4. $(p < -4)$

$$G = \frac{2 + p \pm \sqrt{p^2 + 4p}}{2} = -(1 + \oplus) \pm \frac{\sqrt{p^2 + 4p}}{2}$$

where $\oplus$ means some positive value.

Therefore, one of them will be surely less than -1 which results in $|G| > 1$.

- If $p^2 + 4p < 0$, then p should be less than 0 and greater than -4.

$(-4 < p < 0)$

$$G = 1 + \frac{p}{2} \pm \frac{\sqrt{-p^2 - 4p}}{2} i$$

So, the stability region for $|G| < 1$ is

$$-4 < p < 0$$

D.2 Miller's Method

Follow the method of Miller for the stability region calculation ([60]).

$$G^2 - (2 + p)G + 1 = 0 \tag{D.1}$$

$$f(\lambda) = \lambda^2 - (2 + p)\lambda + 1 \tag{D.2}$$

$$\tilde{f}(\lambda) = \lambda^2 - (2 + \tilde{p})\lambda + 1 \tag{D.3}$$

$$f_1(\lambda) = \frac{1}{\lambda}\{\tilde{f}(0) f(\lambda) - f(0) \tilde{f}(\lambda)\} \tag{D.4}$$

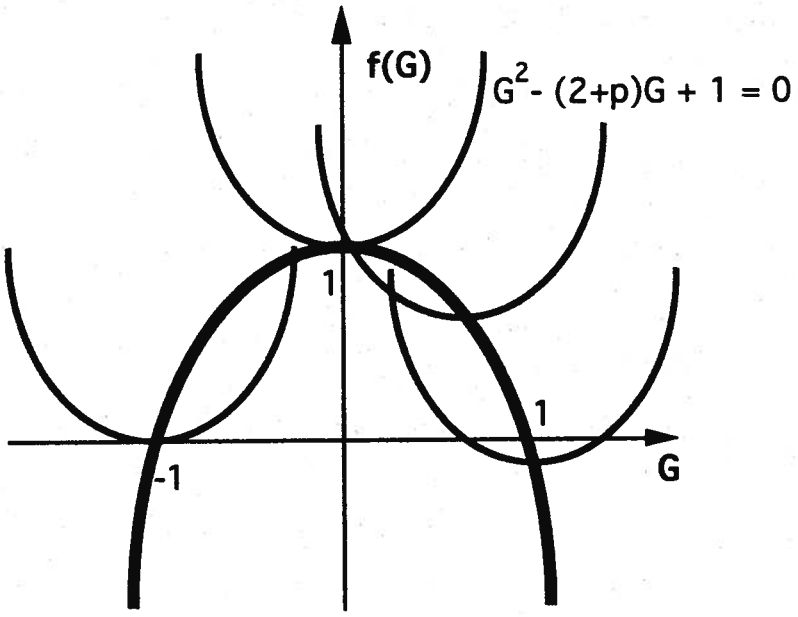

Figure D.1: Algebraic equation of $f(G) = 0$

where $\tilde{f}(\lambda)$ is the equation with the complex conjugate coefficient of f(λ) and $\tilde{p}$ is the complex conjugate of p.

There are two possible ways for f(λ) to have the stable criterion where the modulus of λ is less than 1.

(1) $|\tilde{f}(0)| > |f(0)|$ and zeros λ of $f_1(\lambda)$ are such that $|\lambda| \leq 1$

$$\left.\begin{array}{l} |\tilde{f}(0)| = 1 \\ |f(0)| = 1 \end{array}\right\} \xrightarrow{\text{So}} |\tilde{f}(0)| \not> |f(0)|$$

No region for the stability

(2) $f_1 \equiv 0$ and zeros of $\frac{df}{d\lambda}$ should satisfy $|\lambda| \leq 1$.

- $f_1 = \frac{1}{\lambda}\{\lambda^2 - (2+p)\lambda + 1 - \lambda^2 + (2+\tilde{p})\lambda - 1\} = \tilde{p} - p \equiv 0$

  So, the imaginary part of p should be identically zero.

- $\frac{df}{d\lambda} = 2\lambda - (2+p) = 0$

  $\Rightarrow \lambda = 1 + \frac{p}{2}$

For the magnitude of λ to be less than or equal to 1,

$$-4 < p \leq 1.$$

For example, if $p = g(\Delta t)^2/A_{11}$ which is from the Implicit-like Euler method for one panel near-field open boundary problem, then

$$-4 \leq \frac{g(\Delta t)^2}{A_{11}} = \frac{\pi g(\Delta t)^2}{2a(\ln ca - 1)} \leq 0.$$

Thus, the stability region should satisfy,

$$\left\{ \begin{array}{l} ca < e \quad \text{and} \\ \\ \frac{\pi g(\Delta t)^2}{2a} < -4(\ln ca - 1) \end{array} \right\}$$

BIBLIOGRAPHY

BIBLIOGRAPHY

[1] Abramowitz and Stegun (1972), **Handbook of Mathematical Functions**, Dover

[2] Ames (1977), **Numerical Methods for Partial Differential Equations**, Academic Press

[3] Anderson, Tannaehill, and Pletcher (1984), **Computational Fluid Mechanics and Heat Transfer**, McGraw-Hill

[4] T.S. Angell, G.C. Hsiao, and R.E. Kleinman (1986), *An integral equation for the floating-body problem*, JFM vol.166, pp161-171

[5] G.R. Baker, D.I. Meiron, and S.A. Orzag (1982), *Generalized vortex method for free surface flow problems*, JFM vol.123, pp477-501

[6] P.K. Beier (1990), **NA574 Lecture Note**

[7] J.L. Black, C.C. Mei, and M.C.G. Bray (1971), *Radiation and scattering of water waves by rigid bodies*, JFM vol.46, pp151-164

[8] T. Brockett (1986), **NA520 Lecture Note**

[9] V. Casulli and R.T. Cheng (1990), *Stability analysis of Eulerian-Lagrangian methods for the one-dimensional shallow-water equations*, Appl. Math. Modelling, vol.14, pp122-131

[10] Chan and Hirt (1974), *Two-dimensional Calculations of the Motion of Floating Bodies*, In 10th. Symp. Naval Hydro.,Cambridge,MA:667–682

[11] Chapman (1976), *Free Surface Effects for Yawed Surface-piercing Plates*, JSR vol.20, pp125-36

[12] S. Christiansen (1989), *A stability analysis of a Eulerian method for some surface gravity wave problems*, Notes on Numerical Fluid Mechanics, vol.24

[13] S. Christiansen (1990), *A stability analysis of a Eulerian solution method for moving boundary problems in electrochemical machining*, J. Comp. Appl. Math. vol.33, pp269-296

[14] S.L. Chuang (1973), *Slamming tests of 3-dimensional models in calm water and waves*, NSRDC No.4095

[15] S.L. Chuang and D.T. Milne (1971), *Drop test of cones to investigate the 3-d effects of slamming*, DTNSRDC-3543

[16] R. Cointe (1986), *Hydrodynamic Impact Analysis of a Cylinder*, UC-Santa Barbara Diss. of MS

[17] Z.N. Dobrovol'skaya (1969), *On some problems of similarity flow of fluid with a free surface*, JFM vol.36, pp805-829

[18] J.W. Dold and D.H. Peregrine (1984), *Steep unsteady water waves: An efficient computational scheme*, School of Math. in U. of Bristol

[19] J.W. Dold and D.H. Peregrine (1986), *An efficient Boundary-Integral method for Steep unsteady water waves*, in Num. Meth. for Fluid Dynamics 2

[20] Dommermuth and Yue (1986), *Study of Nonlinear Axisymmetric Body-Wave Interactions*, In Proc. 16th. Symp. on Naval Hydrodynamics, Berkeley

[21] D.G. Dommermuth and D.K. Yue (1987), *Numerical simulations of nonlinear axi- symmetric flows with a free surface*, JFM vol.178, pp195-219

[22] D.G. Dommermuth (1987), *Numerical methods for solving nonlinear water wave problems in the time domain*, Dr. thesis in MIT

[23] D.G. Dommermuth and D.K. Yue (1987), *A high-order spectral method for the study of nonlinear gravity waves*, JFM vol.184, pp267-288

[24] D.G. Dommermuth, D.K. Yue, W.M. Lin, and R.J. Rapp (1988), *Deep Water plunging breakers:a comparison between potential theory and experiments*, JFM vol.189, pp423-442

[25] O.M. Faltinsen (1977), *Numerical solutions of transient nonlinear free- surface motion outside or inside moving bodies*, 2nd. Num. Hydr.

[26] O.M. Faltinsen (1978), *A numerical nonlinear method of sloshing in tanks with two-dimensional flow*, JSR vol.22, pp193-202

[27] O. Faltinsen, O. Kjaerland, A. Nottveit, and T. Vinje (1977), *Water impact loads & dynamic response of horizontal circular cylinders in offshore structures*, 9th annual OTC-2741

[28] W. Frank (1967), *Oscillation of cylinders in or below the free surface of deep fluids*, NSRDC 2375

[29] Gradsteyn and Ryzhik (1980), **Table of Integrals,Series and Products**, Academic Press

[30] Hess and Smith (1974), *Calculation of Non-lifting Potential Flow about Arbitrary Three-dimensional Bodies*, JSR vol.8, pp22-44

[31] M. Greenhow (1983), *Free surface flows related to breaking waves*, JFM vol.134, pp259-275

[32] M. Greenhow (1986), *Wedge entry into initially calm water*, Nor. Marine Tech. Research Insti. A/S

[33] M. Greenhow and W.M. Lin (1983), *Nonlinear free surface effects: Experiments and theory*, MIT83-19

[34] M. Greenhow and W.M. Lin (1985), *Numerical simulation of nonlinear free surface flows generated by wedge entry and wavemaker motions*, 4th Int. Conf. on Num. Ship Hydro.

[35] S.T. Grilli, J. Skourup, and I.A. Svendsen (1989), *An efficient boundary element method for nonlinear water waves*, Comp. Eng. Anal. with Boundary Elements

[36] T.H. Havelock (1948), *The wave resistance of a cylinder started from rest*, Quart. J. Mech. Appl. Math. vol.2, pp325-334

[37] T.H. Havelock (1949), *The resistance of a submerged cylinder in accelerated motion*, Quart. J. Mech. Appl. Math. vol.2, pp419-427

[38] L.M. Hocking (1987), *Waves produced by a vertically oscillating plate*, JFM vol.179, pp267-281

[39] O.F. Hughes (1972), *Solution of the wedge entry problem by numerical conformal mapping*, JFM vol.56, pp173-192

[40] Jin Huh (1991),*A numerical study of capillary-gravity waves*, Ph.D Thesis , U. of Michigan

[41] A. Hulme(1982), *The wave forces acting on a floating hemisphere undergoing forced periodic oscillations*, JFM vol.121, pp443-463

[42] F. John (1949), *On the motion of floating bodies,1*, Comm. on Pure & Appl. Math. vol.2, pp13-57

[43] F. John (1950), *On the motion of floating bodies,2*, Comm. on Pure & Appl. Math. vol.?, pp45-101

[44] C.G. Kang (1988), *Bow Flare Slamming and Non-linear Free Surface-Body Interaction in the Time Domain*, Ph.D Thesis , U. of Michigan

[45] P. Kaplan and M.N. Silbert (1976), *Impact forces on flatform horizontal members in the splash zone*, 8th annual OTC-2498

[46] C. Kharif and A. Ramamonjiarisoa (1990), *On the stability of gravity waves on deep water*, JFM vol.218, pp163-170

[47] Ketter and Drawel (1969), **Modern Methods of Engineering Computation**, McGraw-Hill

[48] Kharif and Ramamonjiarisoa (1990), *On the Stability of Gravity Waves on Deep Water*, JFM vol.218, pp163-170

[49] R.E. Kleinman (1982), *On the mathematical theory of the motion of floating bodies-an update*, DTNSRDC-82/074

[50] A.A. Korobin (1987), *Asympttotic analysis of the unsteady problem of waves in a two-layer flow*, Plenum Pub. Co.

[51] A.A. Korobin and V.V. Pukhnachov (1988), *Initial stage of water impact*, Ann. R. Fluid Mech. vol.20, pp159-185

[52] D. Langbein (1990), *The shape and stability of liquid menisci at solid edges*, JFM vol.213, pp251-265

[53] Lapidus and Pinder (1982), **Numerical Solution of Partial Differential Equations In Science and Engineering**, Wiley-Interscience

[54] W.M. Lin, J.N. Newman and D.K. Yue (1984), *Nonlinear forced motions of floating bodies*, 15th Symp. on Naval Hydro.

[55] M.S. Longuet-Higgins and E.D.Cokelet (1976), *The deformation of steep surface waves on water*, Proc. R. Soc. Rond. A350, pp1-26

[56] M.S. Longuet-Higgins(1986), *Eulerian and Lagrangian aspects of surface waves*, JFM vol.173, pp683-707

[57] MacKay and Saffman (1986), *Stability of Water Waves*, In Proc. R. Soc. Lond. A406,115-125

[58] P. McIver and D.H. Peregrine (1981), *Comparison of numerical and analytical results for waves that are starting to break*, Intl. Symp. Hydro. Ocean Eng.

[59] C.C. Mei and H.S. Chen (1976), *A hybrid element method for steady linearized free surface flows*, Int. J. for Num. Meth. in Eng. vol.10, pp1153-1175

[60] J.J. Miller (1971), *On the location of zeroes of certain classes of polynomials with applications to numerical analysis*, J. of Inst. Math. Appl. vol.8, pp397–406

[61] M. Moghisi and P.T. Squire (1981), *An experimental investigation of the initial force of impact on a sphere striking a liquid surface*, JFM vol.108, pp133-146

[62] D.E. Nakos and P.D. Sclavounos (1989), *On steady and unsteady ship wave patterns*, MIT

[63] J.N. Newman (1977), **Marine Hydrodynamics** MIT Press

[64] J.N. Newman (1985), *Transient axisymmetric motion of a floating cylinder*, JFM vol.157, pp17-33

[65] D.H. Norrie and G. de Vries (1978), *A survey of the finite element application in fluid mechanics*, Finite Elements in Fluids vol 3, pp363-396

[66] D.H. Peregrine (1983), *Breaking Waves on Beaches*, Ann. R. Fluid Mech. vol.15, pp149-78

[67] Peyret and Taylor (1983), **Computational Method for Fluid Flow**, Springer-Verlag

[68] R.D. Richtmyer (1957), **Difference Methods for Initial Value Problems**, Interscience Publishers, Inc.

[69] A.J. Roberts (1983), *A Stable and Accurate Numerical Method to Calculate the Motion of a Sharp Interface between Fluids*, J. of Applied Math., 31:13-35

[70] A.J. Roberts (1987), *Transient free-surface flows generated by a moving vertical plate*, Q. J. Mech. Appl. Math. vol. 40, pp129-158

[71] T. Sarpkaya (1978), *Wave impact loads on cylinders*, 10th annual OTC-3065

[72] L.W. Schwartz and J.D. Fenton (1982), *Strongly nonlinear waves*, Ann. R. Fluid Mech. vol.14, pp39-60

[73] S.F. Shen(1977), *Finite-element methods in fluid mechanics*, Ann R. Fluid Mech. vol 9, pp421-445

[74] M. Shiffman and D.C. Spencer (1951), *The force of impact on a cone striking a water surface(vertical entry)*, Comm. on Pure & Appl. Math. vol. 4, pp379-417

[75] A.B. Stavovy and S.L. Chuang (1976), *Analytical determination of slamming pressure for high-speed vehicles in waves*, JSR vol.20, pp190-198

[76] Ib.A. Svendsen and S.T. Grilli (1989), *Nonlinear waves on steep slopes*, U. of Delaware

[77] F. Ursell (1987), *Mathematical aspects of trapping modes in the theory of surface waves*, JFM vol.183, pp421-437

[78] N.K. Venkat and M.L. Spaulding (1990), *Numerical Simulation of nonlinear free- surface flows generated by a heaving body of Arbitrary cross section*, JSR vol.34, pp92-104

[79] T. Vinje (1982), *On the impact forces from breaking waves*, A.S.Veritas Research

[80] T. Vinje and P. Brevig (1980), *Nonlinear two-dimensional ship motions*, Norw. Inst. Tech. & NHL

[81] T. Vinje and P. Brevig (1981), *Breaking waves on finite water depths. A numerical study*, Norw. Inst. Tech. & NHL

[82] T. Vinje, X. Maogang and P. Brevig (1982), *A numerical approach to non-linear ship motion*, 14th. Symp. Naval Hydro.

[83] T. von Karman (1929), *The Impact on seaplane floats during Landing*, In NACA TN321

[84] W.S. Vorus (1992), *An extended slender body model for planing hull hydrodynamics*, SNAME Section Meeting at Cleveland, Ohio

[85] H. Wagner (1931), *Landing of seaplanes*, N. A. C. A. Tech. Notes No. 622

[86] J.V. Wehausen (1971), *The motion of floating bodies*, Ann. Rev. Fluid Mech. vol.3, pp237-68

[87] R.W. Yeung(1982), *Numerical methods in free-surface flows*, Ann. R. Fluid Mech. vol.14, pp395-442

[88] C.S. Yih (1977), **Fluid Mechanics**, McGraw-Hill

[89] B. Yim (1985), *Numerical solution for 2-D wedge slamming with a nonlinear free surface condition*, 4th Int. Conf. on Num. Ship Hydro.

[90] D.K. Yue, H.S. Chen and C.C. Mei (1978), *A hybrid element method for diffraction of water waves by 3-d bodies*, Int. J. for Num. Meth. in Eng. vol.12, pp245-266

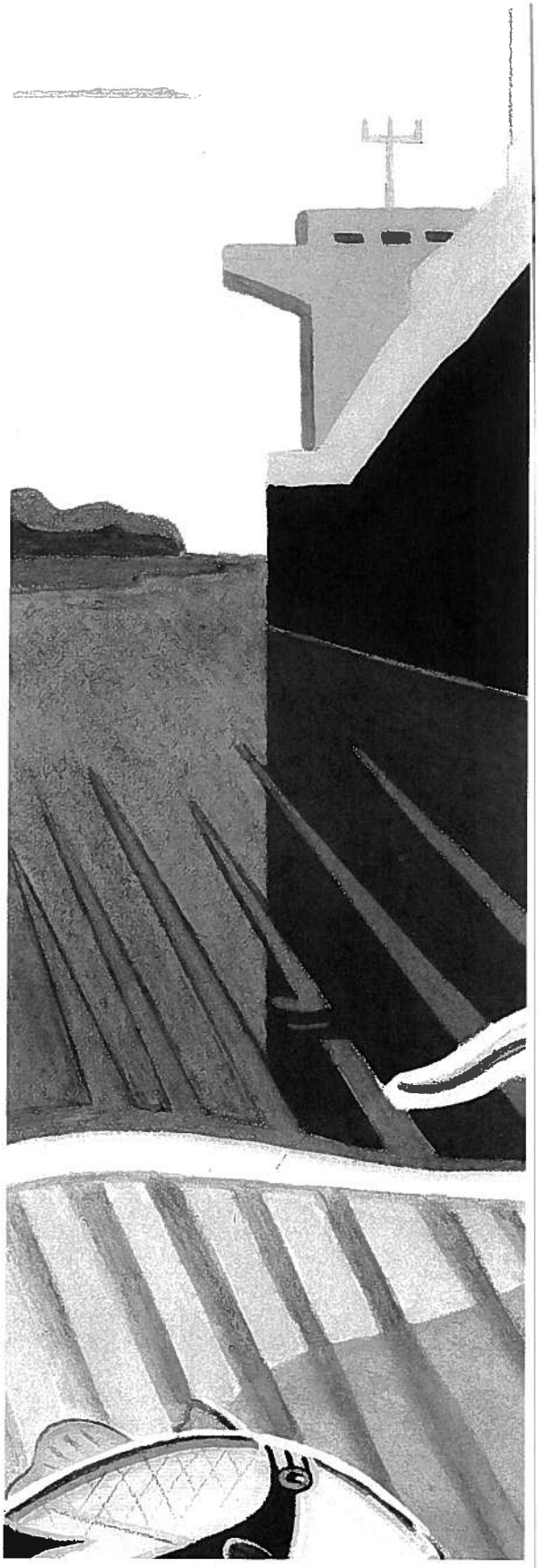

University of Michigan
College of Engineering

Naval Architecture and Marine Engineering
NAME Building
2600 Draper Road
Ann Arbor, Michigan 48109-2145

Phone: (734) 764-6470
Fax: (734) 936-8820

http://www.engin.umich.edu/dept/name